

Physical patterning of silicone hydrogel to alter surface wettability, tear lipid deposition and bacterial adhesion

by
Linan Cui

A thesis
presented to the University of Waterloo
in fulfillment of the
thesis requirement for the degree of
Master of Applied Science
in
Chemical Engineering

Waterloo, Ontario, Canada, 2021

©Linan Cui 2021

AUTHOR'S DECLARATION

I hereby declare that I am the sole author of this thesis. This is a true copy of the thesis, including any required final revisions, as accepted by my examiners.

I understand that my thesis may be made electronically available to the public.

Abstract

A hydrogel is defined as a three-dimensional network of polymer chains that can swell and retain a significant fraction of water inside its structure without dissolving in water. Outstanding properties of a hydrogel such as high biocompatibility, low toxicity and good tissue mechanical matching make it popular in the contact lens area. As a newly developed material, silicone hydrogel (SiHy) has significantly increased oxygen permeability and wearer comfort. However, three major problems still exist are tear film deposition, reduced surface wettability, and microbial contamination.

Generally, chemical modifications can be applied to optimize hydrogel surface properties to improve the performance of hydrogels. In recent years, a new type of surface modification has been discovered to alter hydrogel properties by physically patterning the hydrogel surfaces with topographies. Therefore, we hypothesize that the SiHy surface properties can also be changed by adding surface topographies. In this project, patterns with different dimensions (diameters, heights and spacing distances) were applied to the SiHy surface, and we also evaluated their effects on hydrogel surface wettability, lipid deposition and microbial adhesion.

Therefore, a variety of surface patterns were first fabricated on polypropylene (PP), by embossing with Silicon wafer, as molds with the mirror patterns for the subsequent SiHy fabrication. PP films from three different sources was used for patterning, and the roughness and patterning fidelity were investigated. Based on the characterization, PP pellets provided by our collaborator were chosen for mold fabrication as they created fewer defects. SiHy samples were subsequently fabricated by the collaborator using the PP mold. We used both a 3D laser confocal microscope and an atomic force microscope (AFM) to measure the actual surface structure dimensions of the PP molds and SiHy samples.

Among different ways to examine the material surface wettability, in this study, the captive bubble method was chosen to determine SiHy wettability. The static and dynamic water contact angles were measured. Further studies were undertaken to test the lipid deposition and bacterial adhesion on surface patterned SiHy samples. Commercial hydrogel contact lenses were used in preliminary tests to evaluate the experimental setup.

Based on the data that we obtained, pattern 11 showed outstanding performance in increasing surface wettability and reducing lipid deposition. However, it also generated higher microbial adhesion compared with other patterns. The principal component analysis (PCA) showed that the lipid deposition was more correlated to the contact angle hysteresis and static water contact angle, while the microbial adhesion was more correlated to the ratio of spacing and diameter. Therefore, surface topography did alter the surface properties of SiHy samples, but further studies are still necessary to figure out how performance on wettability, lipid deposition, and microbial adhesion can be improved synchronously.

Acknowledgements

First and foremost, I would like to acknowledge the assistance and support of my supervisor Dr. Evelyn Yim for her patience and motivation that I have learnt much more than knowledge and experimental skills from her.

I also need to express my appreciation to my committee members, Dr. Tizazu Mekonnen and Dr. Eline Boghaert, for reviewing my thesis and giving me feedback.

Also, I would like to thank all the help that I received from our collaborators Dr. Sourav Saha, Dr. Melanie George, Dr. Jing Ni and Dr. Lu Jiang. Their suggestions on experimental setup and optimizing methods were very important throughout the whole study.

The completion of this project could not have been accomplished without the support of people from other labs as well. Many thanks to Dr. Lyndon Jones and Miriam Heynen at School of Optometry & Vision Science for giving me the access to the captive bubble device. I am also grateful to Dr. Tizazu Mekonnen, Dr. Valerie Ward, Dr. Mark Servos and Leslie Bragg for allowing me to use their labs for FTIR analysis, bacteria culture and radioactive analysis.

My sincere thanks also go to our group members Dr. Yuan Yao, Dr. Aung Moe Zaw, Grace Pohan, Wesley Luu, YeJin Jeong, Sarah Wen-Hui Chan and Sabrina Mattiassi, for giving me much help and encouragement.

Table of Contents

List of Figures.....	vii
List of Tables	x
Chapter 1 Introduction.....	1
Chapter 2 Literature review	3
2.1 Contact lens development	3
2.1.1 Contact lens history.....	3
2.1.2 Silicone hydrogel (SiHy) contact lenses	3
2.1.3 Conventional methods to improve SiHy contact lens performance	4
2.2 Surface characterization methods.....	4
2.2.1 Surface energy and surface contact angle characterization technique.....	4
2.2.2 Methods for testing protein and lipid deposition methods	5
2.2.3 Bacteria quantification methods.....	6
2.3 Techniques to fabricate patterned hydrogels	6
2.4 Influence of surface topography on interfacial energy	11
2.4.1 Influence of surface topography on the hydrophobicity of hydrogels.....	11
2.4.2 Surface topography alters protein adsorption on hydrogels	12
2.5 Surface topography affects microbial adhesion to hydrogels	12
2.5.1 Surface roughness effect	13
2.5.2 Surface topography effect	14
Chapter 3 Polypropylene (PP) molds fabrication and topography characterization of PP and SiHy samples	16
3.1 Introduction.....	16
3.2 Materials and methods.....	16
3.2.1 Silicon (Si) wafer fabrication.....	16
3.2.2 PDMS mold preparation	18
3.2.2 Heat embossing method to fabricate patterned PP molds.	18
3.2.3 Fabrication of patterned SiHy samples.	19
3.2.4 PP polymer characterization by FTIR and DSC.....	19
3.2.5 Topography characterization of PP molds and SiHy samples	20
3.2.5.1 Industrial 3D laser confocal measuring microscope	20
3.2.5.2 Atomic force microscopy (AFM)	20
3.3 Results and discussion.....	21
3.3.2 Si wafer fabrication.....	21
3.3.2 PP Molds development	21
3.3.2.1 U.S. Plastic Corp. PP (item # 46017).....	24
3.3.2.2 GoodFellow PP (order code 802-942-05).....	26
3.3.2.3 PP pellets provided by the collaborator	27
3.3.3 Surface topography characterization of PP molds and SiHy samples	29
3.4 Conclusion.....	37
Chapter 4 Surface energy characterization and functional characterization of patterned SiHy samples	38
4.1 Introduction.....	38
4.2 Materials and methods.....	38
4.2.1 Water contact angle (WCA) measurement	38
4.2.2 Lipid deposition test.....	40

4.2.2.1 Commercial hydrogel lenses for benchmarking lipid deposition protocol	40
4.2.2.2 Preparation of the complex salt solution (CSS)	40
4.2.2.3 Preparation of lipid tear solution (LTS)	41
4.2.2.4 Preparation of artificial tear solution (ATS).....	41
4.2.2.5 Glass vial incubation.....	42
4.2.2.6 Experimental setup for lipid deposition and lipid extraction	42
4.2.2.7 Fluorescence imaging	43
4.2.3 Microbial adhesion test	43
4.2.3.1 Commercial hydrogel lenses for benchmarking bacterial adhesion procotol	43
4.2.3.2 Bacterial strains tested	43
4.2.3.3 Culture preparation	44
4.2.3.4 Primary adhesion method	44
4.2.3.5 Bacteria extraction and recovery	44
4.2.4 Statistical analysis	44
4.3 Results and discussion.....	44
4.3.1 Static water contact angle	44
4.3.2 Advancing and receding water contact angle	46
4.3.3 Preliminary test to set up lipid deposition test	48
4.3.4 Fluorescent-labeled lipid vs. radiolabeled lipid	49
4.3.5 Effect of scintillation cocktail volume	49
4.3.6 Effect of ATS volume and air exposure time	50
4.3.7 Adsorption vs absorption of lipids	54
4.3.8 Lipid 1 & lipid 2 deposition on surface patterned SiHy samples.....	55
4.3.9 Bacteria growth curve	57
4.3.10 Preliminary <i>bacteria 2</i> adhesion test on commercial lenses	58
4.3.11 Bacterial adhesion onto surface patterned SiHy samples	58
4.4 Correlation between surface pattern parameters and surface properties.....	61
4.5 Conclusion.....	63
Chapter 5 Summary and Future Work	65
5.1 Si wafer fabrication and PP molds development	65
5.2 Oxygen permeability of patterned SiHy samples	65
5.3 SiHy surface properties characterization	65
5.4 Summary	66
References	67

List of Figures

Figure 1. Schematic diagram of sessile drop method.	4
Figure 2. Schematic diagram of captive bubble method.	5
Figure 3. Advancing and receding contact angle measurement through captive bubble method [38].	5
Figure 4. Examples of predesigned patterns with different shapes and sizes on hydrogel surfaces. Reprinted from Biomaterials 84, Cutiongco, Marie FA, et al., Planar and tubular patterning of micro and nano-topographies on poly (vinyl alcohol) hydrogel for improved endothelial cell responses, 184-195, Copyright (2016), with permission from Elsevier [53].	6
Figure 5. Cassie-Baxter model versus Wenzel model.	11
Figure 6. Two opposite surfaces with similar Ra values.	13
Figure 7. Comparison between a flat surface, a surface with random roughness and a surface with specific patterns.	13
Figure 8. <i>S. epidermidis</i> adhesion on PEG hydrogel with different patterns (a) blank control (b) 2 μm apart (c) 1 μm apart (d) 0.2 μm apart. Reprinted from Acta Biomaterialia 5(2), Krsko, P., Kaplan, J. B., & Libera, M., Spatially controlled bacterial adhesion using surface-patterned poly (ethylene glycol) hydrogels, 589-596, Copyright (2009), with permission from Elsevier [137].	15
Figure 9. Schematic diagram of PDMS mold fabrication from Si wafers.	18
Figure 10. Schematic diagram of PP films formation by flattening melted PP pellets.	19
Figure 11. Schematic diagram of PP heat embossing.	19
Figure 12. Scan parameters could be adjusted prior to starting a scan or during the scan.	21
Figure 13. FTIR analysis of PP from U.S. Plastic (green) and GoodFellow (black).	22
Figure 14. DSC analysis of U.S. Plastic PP.	23
Figure 15. DSC analysis of GoodFellow PP.	23
Figure 16. Glass slides (left) and Si wafer (right) worked as the heating substrate.	24
Figure 17. Two surfaces of USP PP had different roughness. One surface was rougher (a), and the other surface was smoother (b).	25
Figure 18. Defects up to 2 μm observed on embossed USP PP film under the 3D laser confocal microscope. ...	25
Figure 19. Areal roughness measurement of blank USP PP sample. Root mean square height (Sq), Skewness (Ssk), Kurtosis (Sku), maximum peak height (Sp), maximum pit height (Sv), maximum height (Sz), arithmetical mean height (Sa), root mean square gradient (Sdq) and developed interfacial area ratio (Sdr) were measured.	26
Figure 20. GoodFellow PP was smooth originally (a) but became rough after heat embossing (b).	26
Figure 21. Areal roughness measurement of blank GoodFellow PP sample. Root mean square height (Sq), Skewness (Ssk), Kurtosis (Sku), maximum peak height (Sp), maximum pit height (Sv), maximum height (Sz), arithmetical mean height (Sa), root mean square gradient (Sdq) and developed interfacial area ratio (Sdr) were measured.	27
Figure 22. The uniformity of the pattern was affected by the defects.	27
Figure 23. Surface of the flat PP film made from PP pellets under the 3D laser confocal microscope.	28
Figure 24. Areal roughness measurement of blank the collaborator PP sample. Root mean square height (Sq), Skewness (Ssk), Kurtosis (Sku), maximum peak height (Sp), maximum pit height (Sv), maximum height (Sz), arithmetical mean height (Sa), root mean square gradient (Sdq) and developed interfacial area ratio (Sdr) were measured.	28
Figure 25. The collaborator PP (b) showed better pattern quality than GoodFellow PP (a).	29
Figure 26. The same Si sample was characterized with both AFM (a) and confocal microscope (b). It was more difficult for confocal microscope to get the actual dimension of submicron structures than AFM.	29

Figure 27. The force curve showed the force that the cantilever is undergoing during each oscillation cycle. The cantilever did not work properly in (a) and (b) and work well in (c).....	30
Figure 28. The scalebar should in green during the scanning to guarantee the image quality and protect the AFM.	30
Figure 29. 3D confocal laser images of patterned PP surfaces.	32
Figure 30. AFM images of patterned PP surfaces.	33
Figure 31. 3D confocal laser images of patterned SiHy surfaces.	34
Figure 32. AFM images of patterned SiHy surfaces.	35
Figure 33. OCA 25 captive bubble apparatus for wettability measurement (A) and 3D printed sample holder (B).	39
Figure 34. Adjustable settings for captive bubble measurement.....	40
Figure 35. Experimental setup for lipid deposition and extraction.	42
Figure 36. Static contact angle measurement of all surface patterned SiHy samples was shown in figure (a), and patterns were also analyzed in different groups according to their diameters (b) diameter = D1; (c) diameter = D2; (d) diameter = D3; (e) diameter = D4. D1<D2<D3<D4. D1 and D2 are in submicron size, D3 and D4 are in micro size. Center-to-center distance increases from left to right in each figure. One-way ANOVA analysis was applied. P value style: < 0.05(*), < 0.005(**), < 0.0002(***), < 0.0001(****).	46
Figure 37. Dynamic water contact angle of surface patterned SiHy samples. One-way ANOVA analysis was applied. P value style: < 0.05(*), < 0.005(**), < 0.0002(***), < 0.0001(****).	48
Figure 38. Effect of scintillation cocktail volume to counting results. The cocktail volume did not affect the final counting result and there was no significant effect when considering different cocktail volumes in the same size vial.	50
Figure 39. Lipid 2 deposition onto 4 commercial lenses. One-way ANOVA analysis was applied. P value style: < 0.05(*), < 0.005(**), < 0.0002(***), < 0.0001(****).	51
Figure 40. ATS volume cannot be too low.....	51
Figure 41. Lower ATS volume resulted in less lipid 2 deposited but the same trend. One-way ANOVA analysis was applied. P value style: < 0.05(*), < 0.005(**), < 0.0002(***), < 0.0001(****).	51
Figure 42. Lipid 1 deposition onto 4 commercial lenses. One-way ANOVA analysis was applied. P value style: < 0.05(*), < 0.005(**), < 0.0002(***), < 0.0001(****).	52
Figure 43. ATS volume did not affect the amount of lipid 1 deposited.	52
Figure 44. Effect of “shaking” mode and pausing time. One-way ANOVA analysis was applied. P value style: < 0.05(*), < 0.005(**), < 0.0002(***), < 0.0001(****).	53
Figure 45. Lipid 1 deposition on 4 commercial lenses. Deposition on omafilcon A was significantly lower than all other three lenses. One-way ANOVA analysis was applied. P value style: < 0.05(*), < 0.005(**), < 0.0002(***), < 0.0001(****).	54
Figure 46. Lipid 2 soaked (absorbed) more into the lens while lipid 1 adsorbed onto the lens surface.	55
Figure 47. lipid 2 deposition on pattern SiHy samples. One-way ANOVA analysis was applied. P value style: < 0.05(*), < 0.005(**), < 0.0002(***), < 0.0001(****).	56
Figure 48. Lipid 1 deposition onto patterned SiHy samples. T test was performed to compare patterned SiHy samples with the blank control, and a p < 0.05 was considered significantly different. P value style: < 0.05(*), < 0.005(**), < 0.0002(***), < 0.0001(****).	57
Figure 49. <i>Bacteria 2</i> growth curve at 37 °C.	57
Figure 50. <i>Bacteria 1</i> growth curve at 26 °C.	58
Figure 51. <i>Bacteria 2</i> adhered more onto lotrafilcon A lenses than etafilcon A lenses. T test was performed, and a	

p < 0.05 was considered significantly different. P value style: < 0.05(*), < 0.005(**), < 0.0002(***), < 0.0001(****). 58

Figure 52. *Bacteria 2* adhesion onto patterned SiHy samples. One-way ANOVA analysis was applied. P value style: < 0.05(*), < 0.005(**), < 0.0002(***), < 0.0001(****). 60

Figure 53. *Bacteria 1* adhesion onto patterned SiHy samples. One-way ANOVA analysis was applied. P value style: < 0.05(*), < 0.005(**), < 0.0002(***), < 0.0001(****). 60

Figure 54. PCA analysis with respect to different variances. (a) proportion of component variances, (b) PC1 vs. PC2, (c) PC1 vs. PC3, (d) PC2 vs. PC3..... 62

Figure 55. Linear regression of lipid 1 deposition vs. contact angle hysteresis for submicron and micro patterns. 62

Figure 56. Linear regression of *bacteria 1* adhesion vs. spacing/diameter ratio for submicron and micro patterns. 63

List of Tables

Table 1. Relationship between water contact angle and surface wettability.	4
Table 2. Description and comparison between common hydrogel surface patterning methods.	8
Table 3. List of patterns that were investigated in this study.	17
Table 4. PP temperature decreased versus time.	24
Table 5. Pattern transfer fidelity	36
Table 6. Four commercial hydrogel lenses used for preliminary lipid deposition test.	40
Table 7. Concentration of components used to prepare complex salt solution [153].	41
Table 8. Molecular and experimental details of lipids used in all lipid deposition tests [153].	41
Table 9. Molecular weight and concentration of proteins in ATS.	42
Table 10. Two commercial hydrogel lenses used for preliminary bacteria adhesion test.	43
Table 11. Different types of vials/tubes evaluated for lipid deposition test.	49

Chapter 1 Introduction

Contact lenses refer to transparent lenses that are worn directly on human cornea. Because of the direct contact with the cornea, they need to meet higher requirements to function properly and avoid damaging the eyes. Basically, a contact lens should be able to correct the vision by altering its optical parameters such as thickness, diameter, base curve, sphere power and cylinder power. Also, only nontoxic materials should be used to fabricate contact lenses.

Another concern that wearers always have when they make a choice is whether contact lenses can support high comfort. It is well known that poor oxygen permeability can adversely affect successful contact lens wear. Oxygen permeability describes the amount of oxygen that can pass through the contact lens to reach the eye [1]. Oxygen is extremely important for cornea cell health, but contact lenses could prevent the absorption of oxygen, leading to the mild hypoxia of cornea. In addition to the oxygen permeability, the comfort of contact lenses can also be highly influenced by tear film deposition [2]. Tear film consists of three layers: mucin layer, aqueous layer, and lipid layer [3]. The lipid layer is the outermost layer, and it can help reduce evaporation of natural tears; the aqueous layer is the middle layer, and it works to prevent infection; the inner layer is the mucin layer, it is mainly responsible for maintaining the eye lubrication. Tear film mainly works to keep the eye moist and increase the flexibility of eye ball movement [4]. It can also help reduce astigmatism and change the optical properties of the cornea. However, deposits including proteins, mucins, and lipids onto contact lens surfaces can disrupt the tear function and cause discomfort to the wearer.

Ideally, contact lens should also exhibit low microbial contamination. Dozens of microbial keratitis have been discovered to associate with contact lens wear in the past few years [5, 6]. Microbial adhesion to contact lenses is harmful to the health of human eyes, as many eye infections and illnesses could arise from them. Based on the data from Willcox, unfortunately, the number of bacteria adhere to SiHy lenses are even higher than that of poly-HEMA lenses due to the hydrophobicity of silicone hydrogel surface [7]. Bacteria adhesion onto a surface can be divided into three phases: reversible phase, irreversible phase and biofilm formation phase [8]. The biofilms can increase the resistance of bacteria to antimicrobial substances such as host defense systems and antibiotics. They can also be formed on lens surfaces to protect the bacteria from being wiped out [9]. The development of daily disposable contact lenses has helped decreasing the infection rate significantly because wearers do not need to reuse and clean the CL anymore, but the infection risk still exists. Tears also contain a variety of specific bactericidal substances. For example, lysozyme can destroy the cell wall of bacteria, causing the dissolving and death of bacteria [10]. Lactoferrin and immunoglobulin in tears also exhibit antibacterial effects [11]. Therefore, disruption of tear film stability caused by lipid deposits can also affect microbial contamination of eyes.

As a newly developed material, SiHy contact lenses allow up to five times more oxygen to reach the cornea than conventional hydrogel lenses due to their silicone components [12]. Such outstanding performance makes them the most popular material in contact lens industry. However, microbial contamination and tear film deposition problem still exist. In addition to traditional chemical modifications such as altering hydrophilicity by grafting hydrophilic molecules [13] or introducing antimicrobial agents into contact lens care solutions [14], a new method has been introduced in recent years to change hydrogel properties by physically patterning the hydrogel surface.

Therefore, we hypothesize that we can also alter SiHy surface properties by adding different submicron/micro-topographies onto their surfaces. We first aimed to obtain the surface patterned SiHy samples. In this research, we prepared the silicon wafer through e-beam and UV-lithography, and polypropylene (PP) molds through heat embossing method with different surface patterns, and our collaborator fabricated surface patterned SiHy from these PP molds. A 3D laser confocal microscope and an atomic force microscope (AFM) were used to confirm the dimensions of these structures. Then, we aimed to figure out the effects of these surface structures on

SiHy surface properties. The captive bubble method was used to measure the SiHy water contact angle and investigate the effect of surface topography on sample surface wettability. Also, the amount of lipid deposited, and the quantity of bacteria adhered onto the samples were evaluated and correlated to different variables.

Chapter 2 Literature review

This chapter will give a review on the contact lens development history, and different characterization methods for surface wettability, lipid deposition and microbial adhesion will also be introduced and compared. As surface patterning method has already been applied to many kinds of hydrogels to alter their properties for various applications, this chapter will also introduce different techniques for hydrogel surface patterning, as well as the influence of patterns on hydrogel surface properties.

2.1 Contact lens development

2.1.1 Contact lens history

Contact lenses (CL), also called corneal contact lenses, are transparent lenses worn on the cornea of the eye to correct vision or for cosmetic use. It is estimated that more than 140 million people around the world wear contact lenses, with over 90% of these are soft contact lenses [15, 16].

In 1508, the world's famous artist Leonardo da Vinci found that the refraction of the cornea can be neutralized when the eye was soaked in water, making him the first person to introduce the concept of contact lens [17]. In the following centuries, different materials have been selected to fabricate contact lenses. In 1888, German scientist Adolf E. Fick and French scientist Edouard Kalt attempted to create glass-based contact lenses for vision correction [18]. However, this kind of contact lenses also introduced very high wearer discomfort, and therefore failed in clinical use. In 1937, a material named Polymethylmethacrylate (PMMA) was applied to mimic the scleral lens, but its low oxygen permeability forced people to continue developing new materials for contact lenses [19, 20]. Afterward, more and more different materials were used for contact lens fabrication, such as cellulose acetate butyrate [21] and silicone elastomer [22] and poly(hydroxyethyl methacrylate) (poly-HEMA) [23].

Contact lenses can be divided into different groups based on their function, lens material and replacement cycle. According to their functions, visual correction lenses can help correct abnormal refraction; cosmetic lenses work to change the color of eyes (iris color), and therapeutic lenses are mainly used for treating patients with various eye diseases. According to the lens materials, they can be divided into hard contact lenses, soft contact lenses and permeable hard contact lenses. As soft contact lenses are more comfortable to wear, they have become the most popular lenses. Also, according to the use cycle, there are daily disposal contact lenses and long wear contact lenses. People can select suitable products based on their habits or requirements. Although potential risks such as infection of chronic conjunctivitis and xerophthalmia could exist, contact lenses generally introduce higher convenience and beauty compared to conventional glasses, making them more and more popular in real life.

2.1.2 Silicone hydrogel (SiHy) contact lenses

Silicone hydrogel (SiHy) is a newly developed material showing outstanding performance in contact lens area. A hydrogel is a crosslinked hydrophilic polymer that does not dissolve in water. Its hydrophilic properties mainly come from the hydrophilic functional groups, while the interactions between the network polymer chains protect it from dissolving in water [24, 25]. Silicones, also called polysiloxanes, are synthetic polymers containing an inorganic alternating silicon and oxygen atoms backbone (-Si-O-Si-O-) with organic functional groups such as vinyl (CH₂), methyl (CH₃) and phenyl (C₆H₅) groups attached to silicon atoms [26]. Silicone hydrogels are usually prepared by adding monomers containing silicones into hydrogel formulations. Either the silicone-containing monomer or the hydrophilic component inside hydrogels can work as the crosslinking agent [27]. For a conventional hydrogel contact lens, the transport of oxygen through the lens only relies on the water molecules. However, as water evaporation occurs throughout the whole day, a higher water content will make it even more difficult for oxygen to be delivered to the cornea, especially later in a day. In this case, hypoxia often occurs, bringing many suffering problems including red eyes, corneal swelling, blurred vision, or even eye infection [28].

Fortunately, the silicone hydrogel lens can help solve this problem. The Si-O bonds are not readily attacked by oxygen, the siloxane molecule is highly flexible due to the free rotation of the Si-O bonds, leading to the high gas permeability of silicones [26, 29, 30]. Therefore, oxygen permeability of SiHy contact lenses doesn't rely on the hydrogel water content anymore, which significantly increased the wearer comfort.

2.1.3 Conventional methods to improve SiHy contact lens performance

Although SiHy lenses have much higher oxygen permeability than traditional hydrogel soft lenses, new challenges are still presented due to its inherent hydrophobicity. They tend to attract lipid deposits from the tear film constituents, which can be a concern as it increases that evaporation of tear film aqueous phase [31]. It has also been reported that SiHy can contribute to a higher microbial contamination due to its hydrophobicity [9, 32].

To overcome this problem, several methods were used to improve the SiHy performance. For example, the lotrafilcon A lenses were plasma coated to create a thin hydrophilic layer on the surface [33, 34], and internal wetting agents based on polyvinyl pyrrolidone were also introduced to enhance the senofilcon A material hydrophilicity [34, 35].

2.2 Surface characterization methods

2.2.1 Surface energy and surface contact angle characterization technique

Wettability is essential to contact lenses because an ideal contact lens should support a stable tear film layer to increase comfort. The most common way to evaluate the surface wettability is by measuring the water contact angle. The relationship between water contact angle and surface wettability can be summarized in Table 1. A conventional method for contact angle measurement is the sessile drop method. As is shown in Figure 1, the sample is placed on the stage in air and the water droplet will be pumped out from the syringe above. Images can be captured using LabView software and then analyzed using ImageJ software. Another method is named as captive bubble method (Figure 2). Opposite to the sessile drop method, the sample is stabilized underwater with the area of interest facing down. Air bubbles will be pumped out from underneath through an inverted needle and a syringe full of air.

Table 1. Relationship between water contact angle and surface wettability.

Contact Angle θ	Wettability
$\theta=0^\circ$	Perfect wetting
$0 < \theta < 90^\circ$	High wettability
$90^\circ < \theta < 180^\circ$	Low wettability
$\theta=180^\circ$	Non-wetting

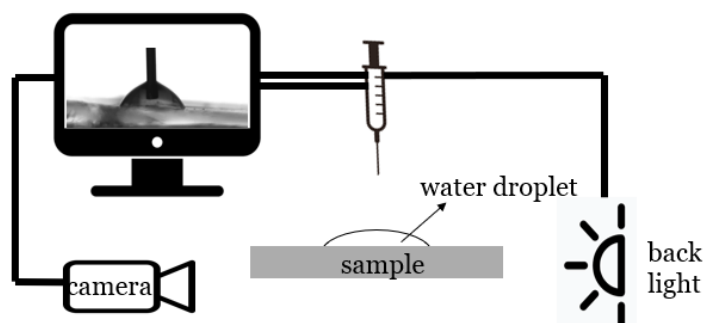


Figure 1. Schematic diagram of sessile drop method.

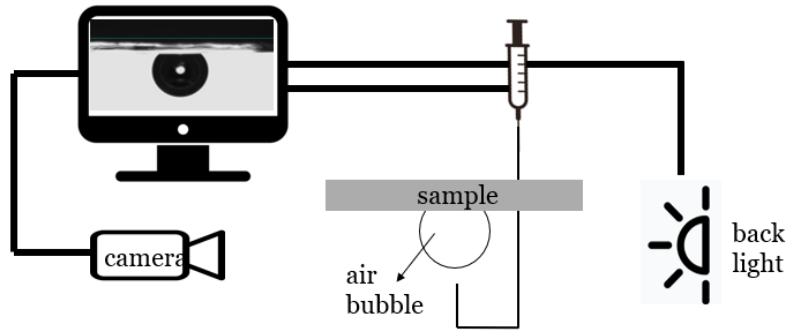


Figure 2. Schematic diagram of captive bubble method.

Static water contact angle refers to the angle between the solid and liquid phases when there is no change, while dynamic water contact angles are produced during the wetting (advancing CA) and de-wetting (receding CA) process on the surface. As is shown in Figure 3, an air bubble is dispensed from a curved needle until it is in contact with the sample surface. Then the volume of the air bubble is enlarged and reduced to obtain the receding and advancing contact angle, respectively. The difference between the magnitude of advancing and receding contact angle can be described as hysteresis [36]. The hysteresis can be determined by multiple factors including surface heterogeneity, surface roughness and liquid molecular size. Generally, higher hysteresis reflects that the surface hydrophilicity is also higher [37].

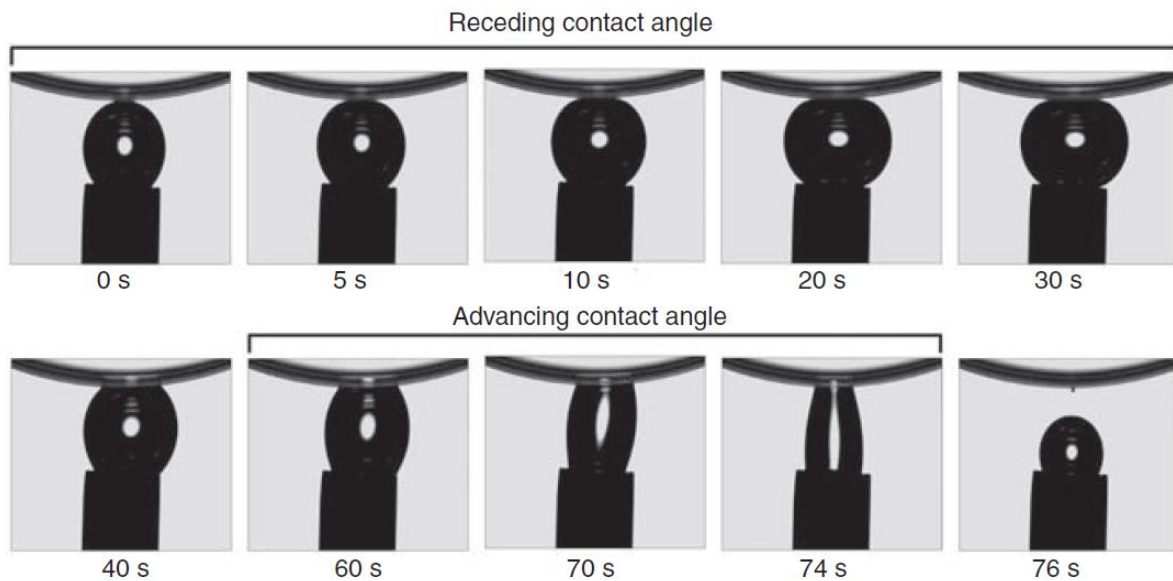


Figure 3. Advancing and receding contact angle measurement through captive bubble method [38].

2.2.2 Methods for testing protein and lipid deposition methods

Both fluorescently labeled lipid [39] and radiolabeled lipid [40] can be used to characterize the lipid deposition onto lenses. The fluorescence intensity can be quantified by setting the excitation and emission wavelength, and the lipid distribution can also be imaged. For radiolabelled lipids, the radioactivity is quantified by the scintillation counter, and the amount of lipid on the sample can be calculated from the radioactivity and lipid specific activity.

2.2.3 Bacteria quantification methods

There are many quantitative methods frequently used to follow the growth of specific microorganisms and determine the number of cells. Four commonly used bacteria quantification methods are optical density (OD) reading, direct microscope counting, cell dry weight and plate counting [41]. The selection of a particular enumeration method highly depends on its accuracy, applicability, and convenience.

OD reading method is a fairly accurate enumeration technique if the sample is well-mixed. It gives results very fast within a few seconds, and one can estimate important parameters such as the average growth rate [42]. The microscope counting method is also rapid and straightforward as it counts the number of cells directly under the microscope. However, clumping of cells within the grid could introduce large errors [43]. The dry weight method is a very coarse technique, and one needs to assume the mass per cell and the cell water content, which can lead to significant errors in the result [44]. The plate counting method usually takes a long time because cells need to grow and become visible on the agar plates. Errors could be introduced from the dilution series, so triplicate plates are necessary for each sample to guarantee the accuracy of the result. This method is also only suitable for counting viable cells [45].

2.3 Techniques to fabricate patterned hydrogels

Surface construction methods can be divided into two types depending on the final surface topographical conditions. The first category is the surface roughening method. Surface roughening methods aim to change the surface roughness and are usually applied to metallic or plastic materials. Surface roughness refers to the height or depth of asperities and irregularities on the surface in both macro and micro scales. The most commonly used parameters describing the roughness are average surface roughness (R_a) and root-mean-square surface roughness (R_{rms}), which can be calculated from the average and root-mean-square deviation of height values from the surface mean line, respectively. Examples of roughening methods include surface silanization [46], Taguchi design [47] and severe shot peening [48].

Different from roughening that mainly creates random and polydisperse surface features, surface patterning methods produce specific micro/nanoscale topographies on material surfaces that are periodic or precisely pre-designed (Figure 4). Based on specific requirements and designs of the material, various patterning methods have also been developed to be applied to different materials such as soft lithography [49], template-based surface nano-patterning [50], nanoimprinting [51], and direct laser interference patterning [52]. The selection of methods depends on both the inherent properties of modified materials and the advantages and disadvantages of each method.

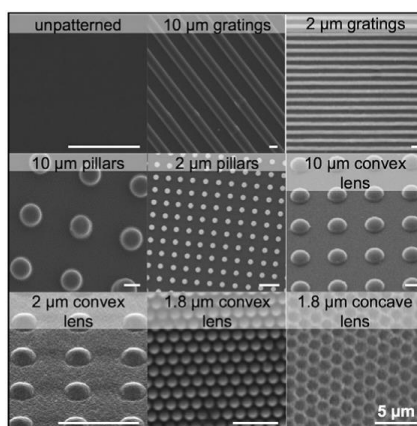


Figure 4. Examples of pre-designed patterns with different shapes and sizes on hydrogel surfaces. Reprinted from Biomaterials 84, Cutiungco, Marie FA, et al., Planar and tubular patterning of micro and nano-topographies on

poly (vinyl alcohol) hydrogel for improved endothelial cell responses, 184-195, Copyright (2016), with permission from Elsevier [53].

Due to the high water content, any change in volume of hydrogel resulting from swelling or deswelling can subsequently cause surface deformation, such as feature widening, making it difficult to precisely obtain the initially designed patterns. Also, extensive swelling can occur in hydrogels with higher precursor concentration, resulting in the undesirable detachment of the hydrogel layer from the substrate during the patterning process [54, 55]. Compared to densely crosslinked stiff hydrogels, loosely crosslinked soft hydrogels are more prone to damage during the demolding step as they could easily break into debris under mechanical stress [56]. In addition to the fragility of hydrogel, the adsorption of protein-based hydrogel precursor onto templates such as polydimethylsiloxane (PDMS) without surface treatment, due to the nonspecific protein adsorption onto surfaces, could also affect the demolding process [54, 57, 58]. Therefore, it is challenging to apply conventional surface patterning techniques mentioned above to hydrogel materials directly.

The casting method is one of the most commonly used methods for hydrogel patterning. Crosslinking hydrogel solution is usually poured onto the surface of a prepared negative mold with specific patterns, so the precisely pre-definable patterned hydrogel can be obtained after demolding the crosslinked hydrogel from the mold [53, 55, 59, 60]. Another popular way to fabricate surface topographically patterned hydrogel is photolithographic patterning technique, where the mixed solution of photo-initiator and monomer are layered onto the photoactive hydrogel substrate and exposed to UV light through the photolithographic mask with desired patterns [61, 62]. Other commonly used methods such as nanoimprinting [53, 63-65], 3D printing [66-68], electrospinning [69-71], multiphoton patterning [72-75], e-beam lithographic patterning [76, 77], Self-assembly wrinkle technique [78, 79], ion-induced nanopatterning [80] and swelling-induced patterning [81, 82] also have their own specific fabrication mechanism and process. In addition, many research groups have also developed effective methods to add patterns to hydrogel substrates. For example, dithiol macromolecular linker that can both bond to gold covalently and entangle the PEG hydrogel network was used to transfer a cell-adhesion-available gold microarray from the initial glass substrate to a cell-adhesion-resistant PEG hydrogel surface [83]; and Peng's group has successfully obtained surface patterned hydrogels via ion inkjet printing [84]. Features of these techniques and the resolution they can reach have been listed in Table 2.

In general, due to the special physical and chemical properties of hydrogel materials, several techniques have been developed from conventional surface construction methods to pattern hydrogels. Based on the hydrogel type and the desired application, these techniques could also vary from each other in details.

Table 2. Description and comparison between common hydrogel surface patterning methods.

Common surface patterning methods	Description	Feature size range / resolution	Advantages	Disadvantages	Ref
Casting method	Crosslinking hydrogel solution is poured on top of negative molds.	Submicron/micro-size features	<ul style="list-style-type: none"> • Simplicity • Low cost • Versatility 	<ul style="list-style-type: none"> • Mold materials should have good wetting properties. • Potential pattern collapse during demolding due to excessive stress of mold materials 	[53, 55, 60, 85]
Thermal-based nanoimprint lithography (for thermo-plastic polymer)	The substrate will be heated up and soften into a molten stage, and it will fill in the negative mold cavities under specific pressure and time.	Nanoscale features (down to 6 nm)	<ul style="list-style-type: none"> • High-resolution used for planar patterning • High-throughput process 	<ul style="list-style-type: none"> • Precise temperature control needed • Temperatures much higher than glass transition temperature T_g can cause serious damage to the substrate. 	[63, 64]
Nanoimprint lithography	Crosslinking of hydrogel on the patterned mold happens during nanoimprinting.	Submicron-size features	<ul style="list-style-type: none"> • High resolution • Simplicity 	<ul style="list-style-type: none"> • Limited to materials that can be crosslinked during the nanoimprinting process 	[53, 65]
Photolithographic patterning	Specific hydrogel regions are exposed to UV light through the transparency mask.	Micro-size features (A few microns to a few hundred microns)	<ul style="list-style-type: none"> • Simple • Inexpensive 	<ul style="list-style-type: none"> • Only large size patterns can be obtained. • Photomasks necessary 	[61, 62]
3D printing	Stimuli-responsive hydrogel is fabricated layer by layer from a 3D model that is generated by computer-aided-design (CAD) software.	Micro-size features	<ul style="list-style-type: none"> • Fast • Inexpensive • 3D structure easily designed by CAD software 	<ul style="list-style-type: none"> • Lack of various printable hydrogel systems • Limited resolution and feature size 	[66-68]
Ion inkjet printing	The crosslinking density of the	resolution up to several hundred	<ul style="list-style-type: none"> • Programmable variation in cross- 	<ul style="list-style-type: none"> • Patterning strongly relies on 	[84]

	printed regions will be increased by the complexation between the polyelectrolyte and ferric ions, and the hydrogel can have shape deformation upon swelling / deswelling.	micrometers	linking densities <ul style="list-style-type: none"> • Controllable swelling & deswelling behavior of the hydrogel 	the shapes of metal anodes; <ul style="list-style-type: none"> • Not suitable for continuous, or mass production of complicated patterns. 	
Electrospinning method	The hydrogel is formed by stabilizing the nanofibers (applied either during or after the spinning process) and rapid dissolution is prevented via re-exposure to water.	Difficult to achieve pattern with size (diameter or pore) >50 μm	<ul style="list-style-type: none"> • Low cost • High throughput • Tunability • Both the morphology of individual fibers and the topography of the entire nanofibrous scaffold are controllable. 	<ul style="list-style-type: none"> • Limited to random and aligned fibrous structure. 	[69-71]
Multiphoton patterning method	Direct laser writing enables patterning of 3D microstructures without photomasks or complex optical systems; photo-sensitive crosslinker is used in the fabrication.	Submicron /micro-size features	<ul style="list-style-type: none"> • High resolution • Free-form 3D fabrication • Noncontact fabrication 	<ul style="list-style-type: none"> • Precise control of laser wavelength needed • Limited to photo-crosslinkable materials 	[72-75]
E-beam lithographic patterning method	Hydrogel is crosslinked upon exposure of accelerated electrons to create patterns on the substrate.	Submicron /micro-size features	<ul style="list-style-type: none"> • High resolution • Complex patterns can be printed directly. 	<ul style="list-style-type: none"> • Longer processing time • Expensive • Dose tests are always necessary and significant to precisely obtain the expected feature size and shape. 	[76, 77]
Swelling-induced surface patterning method	The photocurable hydrogel is exposed to the light in air and then swelling, the anisotropic	Tens of micrometers	<ul style="list-style-type: none"> • Stable patterns in both dry and swollen states • Simplicity, additional coating 	<ul style="list-style-type: none"> • The control of final pattern morphology could be challenging. 	[81, 82]

	osmotic pressure in depth makes the outer surface buckled and create the pattern.		or organic solvents are unnecessary for swelling		
Self-assembly wrinkle technique	The pre-polymerized hydrogel is spin-coated and deswelling in vacuum, then exposed to UV to form wrinkled patterns.	Micro-size features	<ul style="list-style-type: none"> • Simplicity • Fast 	<ul style="list-style-type: none"> • Not suitable for specifically designed patterns 	[78, 79]
Ion-induced nanopatterning method	Ions are used in the directed plasma nano synthesis to create the nanostructures on hydrogel surface.	Nanosized features	<ul style="list-style-type: none"> • Reproducible fabrication • Stable to sterilization • Mechanically stable • Nanostructures with high aspect ratio can be fabricated without collapse. 	<ul style="list-style-type: none"> • Not suitable for specifically designed patterns 	[80]

2.4 Influence of surface topography on interfacial energy

2.4.1 Influence of surface topography on the hydrophobicity of hydrogels

In the past few decades, many studies have shown that the wetting state can be changed by adding different surface topographies, in addition to being determined by the intrinsic hydrophobic or hydrophilic properties of the material [86-90]. Two models, the Cassie-Baxter model and the Wenzel model, have been proposed to describe the process when a droplet is placed on a solid surface. In the Cassie-Baxter model, the droplet will only touch the top of the topography, when air would be trapped between the micron-sized asperities. While in the Wenzel model, the microstructures will penetrate the droplet (Figure 5) [91-93]. Dai *et al.* have identified that the magnitude of the interaction between droplets and substrates can be varied by the height and width of pillar structures. When the water contact angle on a smooth surface is larger than 93.13° , increasing the height of pillars (2.82 nm width) to 3.76 nm can change the wetting state of the surface from Wenzel state to Cassie-Baxter state. However, when the water contact angle on the smooth surface is smaller than 85.1° , such influence of pillar dimensions on the wetting state was abolished [94].

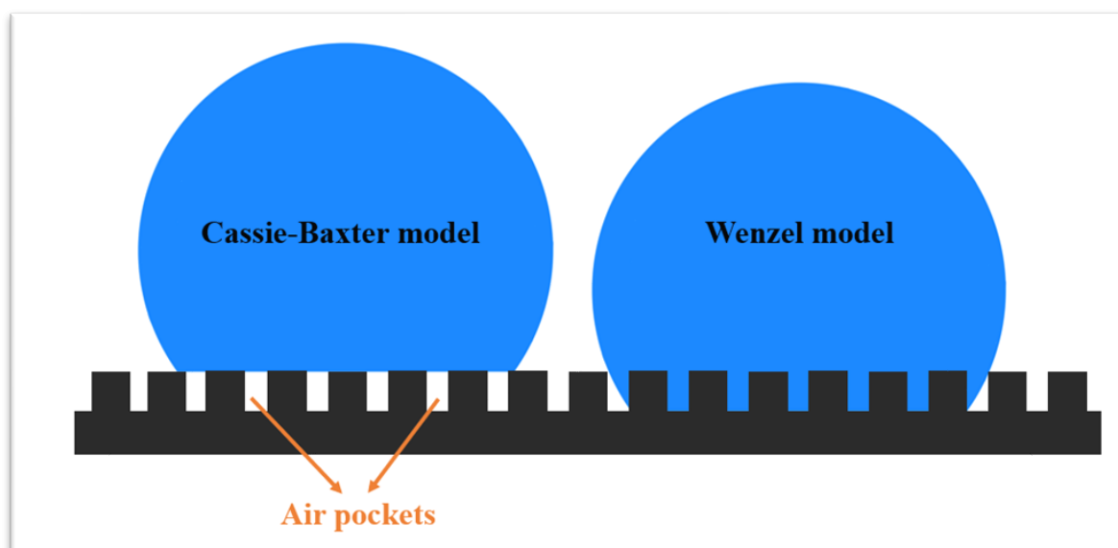


Figure 5. Cassie-Baxter model versus Wenzel model.

Hydrophobicity is one of the most significant properties in material surface science. The hydrophobicity of hydrogels can affect their performance in different applications critically. For example, the delivery of hydrophobic drugs by hydrogels has been limited, as hydrophobic drugs are generally less compatible with hydrogels due to the hydrophilic matrix of hydrogel polymers [95, 96]. By altering the hydrophobicity, hydrogels could be adapted to be able to expand their application in hydrophobic drug delivery as well. Also, it has been demonstrated that hydrogel hydrophobicity can modulate cell behaviors such as cell adhesion and migration [97, 98]. Inspired by the topographical effect on hydrophobicity and wettability of various materials such as silicon [93] and aluminum [99], Cutiongco *et al.* measured water contact angle of casted PVA hydrogel with different topographies. Among several patterns including pillars, concave lenses and gratings, $2\ \mu\text{m}$ gratings showed significantly higher contact angle compared to flat hydrogel samples [53]. Similarly, casted pHEMA hydrogel with lotus leaf topography has been measured to have much higher water contact angles compared with flat hydrogel samples [91]. Another test was also performed on the pHEMA hydrogel. In the test, the water droplet was replaced by a Ga/In/Sn liquid alloy, because the water was immediately incorporated by the prepared hydrogel network. However, it still showed some interesting phenomenon related to the effect of surface microstructure on

the liquid state. The pHEMA hydrogel was structured to have $165\ \mu\text{m} \times 170\ \mu\text{m}$ rectangular pillars with $1500\ \mu\text{m}$ height and $700\ \mu\text{m}$ center-to-center distance. Compared to the smooth pHEMA surface, the liquid contact angle on the patterned pHEMA surface was significantly higher [100]. The above studies show that the surface topography has an effect on hydrogel material hydrophobicity, which supports further research on commercial hydrogel products.

2.4.2 Surface topography alters protein adsorption on hydrogels

Few studies discussed lipid deposition onto surface patterned hydrogels. However, protein adsorption altered by surface topography has attracted more attention. As a critical component in human body fluids, proteins can adsorb onto the surface of the material within seconds, once being exposed to a biomaterial [101]. Such adsorption is essential in inducing cell responses [102, 103]; on the other hand, the adsorption can lead to unexpected pathological phenomenon. For example, the adsorption of blood proteins on blood-contacting biomaterials can trigger the activation of coagulation and complement pathways, followed by blood cell activation, which will lead to thrombus formation on the surfaces [104]. Also, in the area of contact lens research, adsorption of tear film substances onto the lens material, including proteins and lipids, can lead to wearer discomfort or even severe eye symptoms [105]. Developing biomaterials with ability to prevent unspecific protein adsorption will be significant for anti-fouling surfaces, and other applications with defined chemistry or with specific and desirable bioactivities.

Recent studies have shown that adding topography onto hydrogel surface can alter protein adsorption. PEG is reported to be protein- and cell-repellent. Schulte *et al.* formed hydrogel with 6-arm star-shaped poly(ethylene glycol) (star-PEG) macromonomers by UV lithography. Both flat star-PEG hydrogel and patterned star-PEG hydrogel samples were washed in sterile water and PBS to remove toxic residuals before fibroblast cell culture. Two patterns were selected, pillars with $3\ \mu\text{m}$ diameter, $3\ \mu\text{m}$ height and $6\ \mu\text{m}$ center-to-center distance and lines with $5\ \mu\text{m}$ depth and different spacing distances from $5\text{-}50\ \mu\text{m}$. No cell spreading was observed on the flat hydrogel surfaces as expected, while on the patterned surfaces, cells spread on pillar tops and wrapped around the structures. One possible reason why cell adhesion was successful in patterned PEG was that the amount and type of proteins adsorbed on the structured areas were different from that on flat surfaces. To further support this hypothesis, they continued experiments on the adsorption of proteins onto patterned hydrogel surfaces, including bovine serum albumin (BSA), bovine fibronectin (FN), and bovine vitronectin (VN). Both bovine FN and bovine VN showed a preference to adhere on the groove walls on surfaces with line patterns [106, 107]. Similarly, Cutiongco *et al.* reported that the human umbilical vein endothelial cells (HUVEC) had significantly higher adhesion on casted cyclic RGD peptide (cRGD) modified PVA hydrogel films with $2\ \mu\text{m}$ gratings than the unpatterned control. The result again showed the possible effect of surface topography on protein adsorption [108].

2.5 Surface topography affects microbial adhesion to hydrogels

Microbial adhesion or biofilm formation on medical devices could lead to serious health problems. Patients can suffer from infections or even death with pathogenic bacteria adhesion on medical devices such as implants and catheters. In recent years, several methods have been developed to reduce or prevent microbial adhesion of biomaterials, including adding antimicrobial reagents or toxic biocides into coatings and substrates [109, 110]. However, such toxic reagents added into the biomaterials could possibly harm human cells or tissues, especially in close proximity or with close contact. The effectiveness of the biocides could also be unstable for biocides with a short half-life [111, 112]. In order to provide a safer microenvironment for medical use, numerous efforts have been made to develop a more efficient and user-friendly technique that can reduce microbial adhesion. Surface roughness and surface topography are factors that are newly discovered to be able to significantly affect the interactions between bacteria and material surfaces. Both of them have been applied on biomaterials to control

microbial adhesion in biomedical applications. The effects and mechanism of each type of surface modification are different and they are further discussed below.

2.5.1 Surface roughness effect

Surface roughness mainly shows heights and depths of surface irregularities, which can be measured via two parameters R_a and R_{rms} , respectively. Yong *et al.* tested the adhesion of *Staphylococcus aureus* and *Pseudomonas aeruginosa* onto the Etafilcon A hydrogels with different surface roughness values. A significant positive correlation existed between the hydrogel roughness and colony forming units (CFUs) of the two bacteria [113]. Similarly, *Staphylococcus epidermidis* adhesion onto five kinds of hydrogels (Omafilcon A, Ocufilecon B, Nelfilcon A, Senofilcon A and Comfilcon A) with varied R_a and R_{rms} values measured by AFM was studied [114]. In the result, hydrogels with lower R_a values were observed to have lower CFUs, and the authors suggested that it is probably because the colonization of microorganism could be affected by the surface roughness [114].

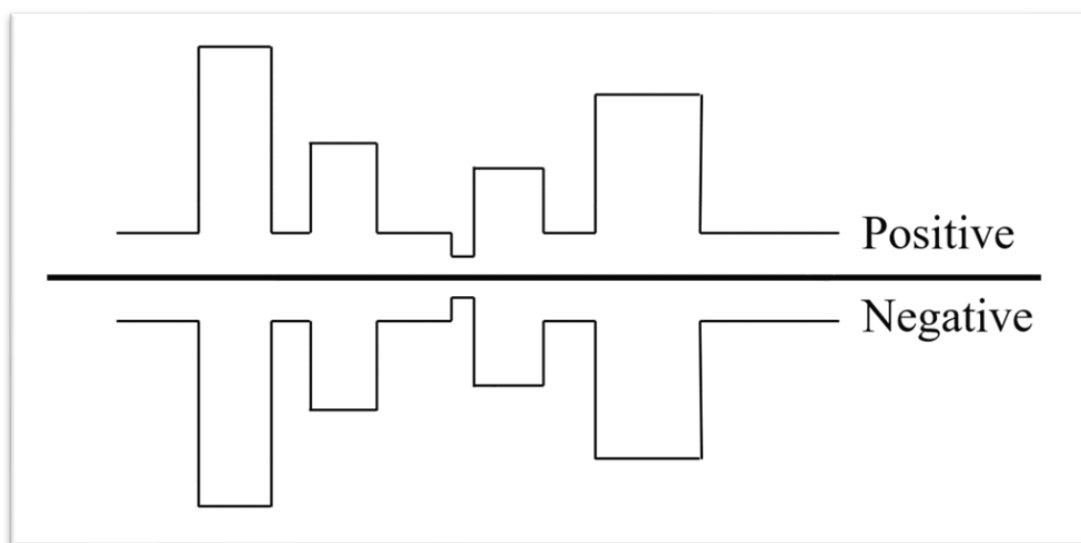


Figure 6. Two opposite surfaces with similar R_a values.

However, the two parameters R_a and R_{rms} are not sufficient to describe and characterize the surface properties. Only the information about the variation of asperities heights can be given by the surface roughness values. For example, although the shapes, slopes or sizes of irregularities can be different on two surfaces, the calculated values of R_a can still be very similar to each other when values of peaks and valleys are canceled out (Figure 6) [114, 115]. Therefore, these two surfaces with similar roughness value could perform differently in different specific applications. The effect of material surface roughness on bacterial adhesion has been controversial. Some researchers argued that rougher surfaces lead to higher adhesion forces of bacteria, while others argued that the surface roughness had nothing to do with the bacteria adhesion or even prevented the adhesion [113, 114, 116-118]. Such debate also reflects the controversy of the actual effects of surface random roughness. Due to this problem, precisely designed topographies, in which researchers can engineer the dimension, shape and geometry of the topography systematically, can be more useful and promising in studying how surface patterning affects the interactions between bacteria and biomaterial surfaces (Figure 7).

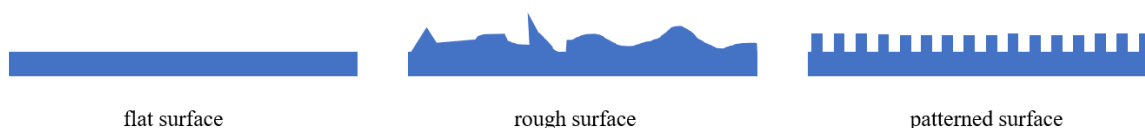


Figure 7. Comparison between a flat surface, a surface with random roughness and a surface with specific patterns.

2.5.2 Surface topography effect

Bacterial motility on the surface can be led by the interaction between the topography and bacteria appendages such as flagella and pili. According to the shape and size of the topography, different bacteria also show distinct motion preferences and responses to the surface, such as near-surface swimming and surface-anchored spinning [119]. Surface topographies can achieve antibacterial functions by providing anti-adhesion surfaces or bactericidal surfaces. Anti-adhesion surfaces aim to prevent bacterial cells from attaching to a surface via unfavorable surface topography. It has been discovered that topographies with smaller sizes work more efficiently to decrease bacterial adhesion than large structures. Bactericidal surfaces refer to surfaces with specific structures, such as closely spaced nanoscale pillars that can directly pierce through the bacteria cell membrane and kill the bacteria within several minutes [111, 120].

In nature, many animals or plants have evolved surfaces with specific topographies that can either support self-cleaning or protect themselves from bacteria. Such inherent functional surfaces provided inspiration in applying these bio-inspired micro/nanostructures into other synthetic materials to give them antibacterial properties [121-124]. Nanopillars on wings of cicada (*Psaltoda claripennis*) with a height of 200 nm and center-to-center distance of 170 nm have been demonstrated to be able to puncture the membranes of *Pseudomonas aeruginosa* and kill them within 3 min [125]. The inner and outer membranes of *E. Coli* were damaged and separated from each other on dragonfly (*Orthetrum villosovittatum*) wings due to the existence of nanopillars with heights in the range of 189 nm to 311 nm and diameters in the range of 37 nm to 57 nm [126, 127]. Black silicon surfaces with similar biomimicking high aspect ratio nanostructures could kill *Staphylococcus aureus* and *Pseudomonas aeruginosa* bacteria effectively at an estimated killing rate of 450,000 cells min⁻¹cm⁻² [111, 128]. The adhesion of *E.coli* and *Staphylococcus aureus* on micro-patterned PDMS were also observed to be reduced when the bacteria size is larger than that of the pattern groove [120, 129]. Microbial adhesion on more rigid materials with surface topography, such as implant topography, has also been extensively studied. However, as the current paper focuses on topography on hydrogel, readers can refer to excellent review papers for further extended reading [130-132].

As a popular biomaterial, hydrogels with organized surface textures have also been fabricated to study their antimicrobial performance. However, most studies are designed to target bacterial adhesion on hydrogels, while adhesion of other microbes such as fungi or virus are much less taken into account. *Pseudomonas aeruginosa* was cultured on both casted flat and surface patterned chitosan hydrogel films for 18 hours, and CFUs were then counted on agar plates to see if the surface topography could inhibit the bacteria growth [133]. Compared to the flat hydrogel films, *P. aeruginosa* cultured on nanopillars with 120 nm diameter and 230 nm height showed 31% lower CFUs. Nanopillars with 190 nm diameter and 400 nm height exhibited even better antibacterial property with 52% lower CFUs compared to flat chitosan films. The adhesion of *E. coli* onto the patterned PEG hydrogel was examined in another study [134]. In the research by Koh *et al.*, PEG hydrogel with 30 μm x 30 μm square microwells fabricated by UV lithography was attached covalently to the silicon substrate surface via a 3-(trichlorosilyl) propyl methacrylate (TPM) monolayer. After incubating the samples with micro-structured PEG hydrogel in suspended *E. coli* solution for six hours, the *E.coli* bacteria were observed to be confined within the three-dimensional trenches of the hydrogel, showing the active resistance of micro-structured PEG hydrogel to the *E.coli* adhesion. Similarly, another group also incorporated patterned PEG hydrogel coating onto a silanized glass substrate by e-beam lithography method to study the bacteria adhesion compared with common biomaterials, including silicone rubber, poly(methyl methacrylate) (PMMA), and tissue culture polystyrene (TCPS) [135]. The diameter of the hydrogel pattern was designed to be 2.5 μm, 5 μm and 10 μm, with 5 μm or 10 μm interpatch spacing distance. *Staphylococcus aureus* was first allowed to adhere onto the samples for 30 min, and the lowest

bacteria adhesion was observed on patterned PEG hydrogel coatings. Then, murine macrophages were added to see how different surfaces would affect the phagocytosis of the bacteria. Interestingly, the unpatterned PEG hydrogel coated surface exhibited the lowest phagocytosis rate, but this rate was significantly increased on hydrogel patterned surfaces, depending on the patch diameter and the interpatch spacing. The underlying detailed mechanism was still not clear due to lack of research. However, these studies provide the directions for further research on the relationship between bacteria, macrophages, and patterned surfaces. To prevent bacterial contamination more effectively, Papi *et al.* have combined graphene oxide (GO) hydrogels with *Cancer Pagurus* (crab) carapace surface patterns by laser printing, as GO can cause membrane disruption to kill microorganisms and *Cancer Pagurus* carapace is a natural antibacterial surface [136]. The result again illustrated that the patterns on GO hydrogel surfaces reduced the colony area by around 70% for *S. aureus*, 65% for *E.coli*, and 45% for *C. albicans*. Also, a surface-patterned PEG hydrogel crosslinked on the silanized glass substrate by e-beam lithography has been demonstrated to effectively control the adhesion of *S. epidermidis* and to prevent the development of large bacteria colonies (Figure 8) [137].

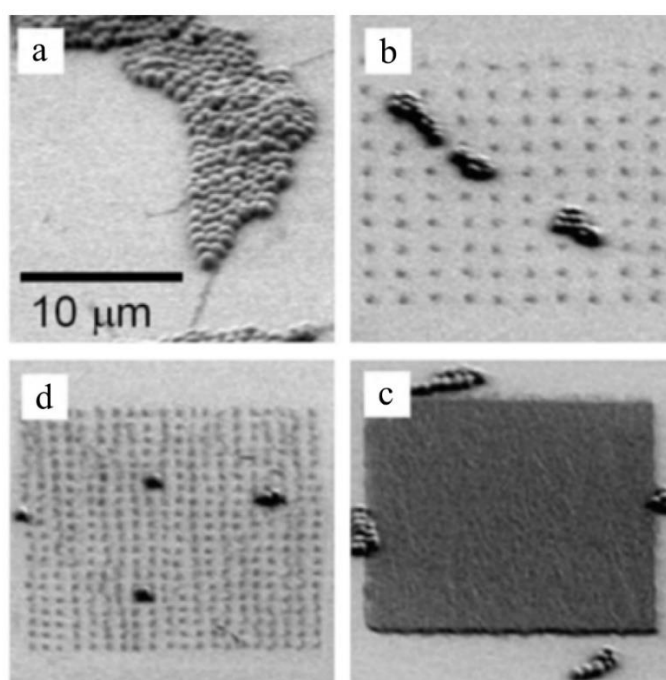


Figure 8. *S. epidermidis* adhesion on PEG hydrogel with different patterns (a) blank control (b) 2 μm apart (c) 1 μm apart (d) 0.2 μm apart. Reprinted from Acta Biomaterialia 5(2), Krsko, P., Kaplan, J. B., & Libera, M., Spatially controlled bacterial adhesion using surface-patterned poly (ethylene glycol) hydrogels, 589-596, Copyright (2009), with permission from Elsevier [137].

Chapter 3 Polypropylene (PP) molds fabrication and topography characterization of PP and SiHy samples

3.1 Introduction

SiHy samples would be fabricated by demolding from PP negative molds, while these PP molds would be prepared through heat embossing method first.

Polypropylene (PP) is a thermoplastic material comprised of propylene monomers. Commercially available PP are commonly available as homopolymers and copolymers. Copolymers can be further classified into block copolymers and random copolymers. Homopolymer PP is popular for general industrial use. Block copolymer PP is often made with ethylene monomers added to improve the impact resistance, while random copolymer PP can be used to make more ductile and transparent products [138, 139]. Different additives can also be added to modify and customize PP to meet unique application requirements.

The melting temperature of PP is around 160 °C [140]. Like other thermoplastics, PP can be repeatedly heated and cooled without significant degradation [141]. Also, PP has a relatively smooth surface and low-toxicity [142], making it a suitable material to be patterned with the heat embossing method. Desired patterns were first fabricated on silicon wafer using e-beam or UV-lithography for heat embossing. The patterned PP could then be used as molds for patterning hydrogel. Our collaborator subsequently fabricated the SiHy samples with surface patterns using these PP molds. The different topographies with various sizes and aspect ratios were evaluated to identify their effects on the SiHy surface properties.

In this chapter, we have developed the fabrication method and surface characterization of surface patterned PP molds. PP from different sources will be evaluated, and surface topography characterization will be performed for both PP molds and SiHy samples using Industrial 3D laser confocal microscope and AFM.

The reflected confocal microscope is a 3D laser non-contact microscope that can deliver accurate measurement data. A 405 nm laser diode light source is optimized to capture the shape of the sample in the field of view. The long working distance objectives could support the noncontact measuring mode better and keep samples from indentation or crash.

The AFM uses a cantilever with a very sharp tip to scan over the sample surface [143]. It has a z-scanner to move the tip up and down and an x-y scanner to move the sample back and forth underneath the cantilever. The position sensor works by tracking the laser beam that is reflected off the flat top of the cantilever. The AFM can then image the topography of a surface by scanning the cantilever over the region of interest. It usually generates an accurate topographic map of the surface by using a feedback loop to control the height of the tip above the surface. As the tip approaches the surface, the close-range attractive forces between the sample surface and the tip will cause the cantilever to bend towards the surface. When the cantilever is brought even closer to the surface, increasingly repulsive forces will cause the cantilever to bend away from the surface instead [144]. Meanwhile, the position-sensitive photodetector records the bending of the cantilever. Any bending in the cantilever will cause changes in the direction of the reflected beam, and the detector can track and record these beam changes.

AFM can exhibit high-resolution images for rigid, dry substrates or films such as Si wafers. However, the AFM cantilever could stick to the sample surface during the scanning process from time to time for relatively soft polymer materials. Not only will the characterization fail easily, but the cantilever could also be damaged permanently under this circumstance. Therefore, AFM probes with lower spring constant and smaller size would be recommended when characterizing soft polymer materials.

3.2 Materials and methods

3.2.1 Silicon (Si) wafer fabrication

Si wafers with pre-designed micron and submicron structures were either ordered from EULITHA or

fabricated in the cleanroom of Quantum-Nano Fabrication and Characterization Facility at University of Waterloo (Table 3).

Table 3. List of patterns that were investigated in this study.

Pattern number	Submicron or micro	Actual dimension	Aspect ratio	Ordered or fabricated
Blank	/	/	/	/
10	Submicron	/	1.1	Ordered from Eulitha (by e-beam)
11	Submicron	/	1	Ordered from Eulitha (by e-beam)
12	Submicron	/	1	Ordered from Eulitha (by e-beam)
13o	Submicron	/	0.2	Ordered from Eulitha (by e-beam)
13n	Submicron	/	0.5	Ordered from Eulitha (by e-beam)
14	Submicron	/	0.5	Ordered from Eulitha (by e-beam)
18	Micro	/	1	Fabricated through UV lithography
19	Micro	/	1	Fabricated through UV lithography
20	Micro	/	0.5	Fabricated through UV lithography
21	Micro	/	0.5	Fabricated through UV lithography
22	Micro	/	0.5	Fabricated through UV lithography
26	Submicron	/	1	Fabricated through e-beam lithography
27	Submicron	/	1	Fabricated through e-beam lithography
28	Submicron	/	1	Fabricated through e-beam lithography
29	Submicron	/	0.5	Fabricated through e-beam lithography
30	Submicron	/	0.5	Fabricated through e-beam lithography
31	Submicron	/	0.5	Fabricated through e-beam lithography
32	Submicron	/	0.5	Fabricated through e-beam lithography
L1	Micro	/	0.5	Fabricated through UV lithography
L2	Micro	/	0.5	Fabricated through UV lithography
L4	Micro	/	0.25	Fabricated through UV lithography
L5	Micro	/	0.25	Fabricated through UV lithography

Single side polished blank Si wafers (prime grade, 100 orientation) were purchased from University Wafer Inc. Patterns with pre-designed dimensions were drawn using KLayout software to create .DGS files that can be read by the lithography systems.

Micron structures with dimension larger than 1 μm were fabricated through photolithography. Blank Si wafers were first spin-coated with MICROPOSIT™ Shipley 1805 photoresist at 5000 rpm for 60 s. The coated Si wafer was then baked on a 115 °C hotplate for 60 s to drive off solvents and increase the stability of the resist film. Because of the sensitivity of photoresists to the light, all coated Si wafers were stored in dark place. After loading the .GDS files, Heidelberg MLA150 Direct Write UV Lithography system was used to expose patterns through a diode laser operating at 405 nm. The Si wafer was carefully unloaded from the operational stage after the exposure and developed in MF319 developer for 45 seconds, followed by DI water for 60 seconds. The wafer was completely dried using nitrogen (N_2) gun and loaded into Oxford ICP380 DRIE Si etcher for etching. The etching time depends on the expected etching depth and therefore can be different for different patterns. Finally, the etched Si wafer was washed in Remover PG at 80 °C for 20 min to remove residual resist and rinsed successively in a 2-Propanol (IPA) bath and a DI water bath.

E-beam lithography technique was used to fabricate submicron patterns because the minimum structure size that the MLA150 system can reach is $1\mu\text{m}$. The fabrication process was similar to that of UV lithography. The clean Si wafer was first spin-coated with ZEP520A e-beam resist for 45 s and baked at $180\text{ }^\circ\text{C}$ for 3 min. Then, the JBX-6300FS Electron Beam Lithography System was calibrated and an exposure was run. The ZED-N50 developer was specific to the ZEP520A resist, and the developing time was modified to be 90 s.

The dimensions of patterns on Si wafers were checked using AFM. Bruker FastScan head and FastScan-A probe were loaded for scanning and the scanning rate was set to be 2 Hz.

3.2.2 PDMS mold preparation

To make the PDMS replica, the Si wafer was first surface treated with trichloro (1H,1H,2H,2H-perfluorooctyl) silane (97%, Sigma-Aldrich) in a desiccation chamber overnight. The PDMS crosslinking solution (base: crosslinker = 5:1) (Dow Corning, Sylgard 184) was mixed for 5-10 min and degassed for 30 min to obtain a homogeneous solution and remove any air bubbles. The solution was then poured onto the salinized Si wafer and degassed for another 30 min until the cavities were filled with the PDMS solution. Afterward, the PDMS was cured at $60\text{ }^\circ\text{C}$ overnight and demolded from the Si wafer.

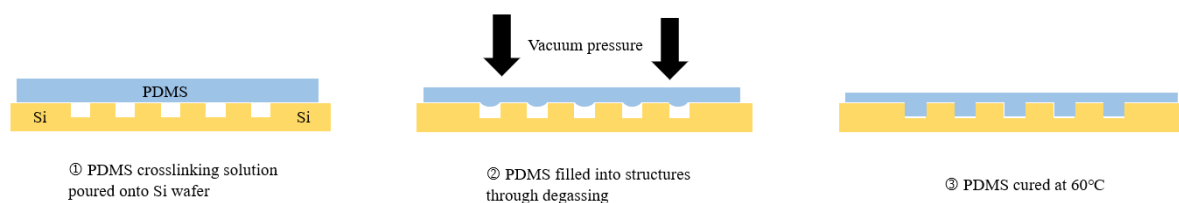


Figure 9. Schematic diagram of PDMS mold fabrication from Si wafers.

When the surface topographical structures were too small (especially for structures with dimension less than $0.5\text{ }\mu\text{m}$) or PDMS was too viscous, PDMS solution failed to fully fill the structure, resulting in an incomplete filling and replication. In this case, an additional step was necessary. After pouring the PDMS solution onto the Si mold surface, the Si mold was centrifuged at 1500 rpm for 30 min and degassed again in the vacuum chamber for 30 min with a coverslip on top. This step provided additional force to push the solution into cavities and therefore can help solve the problem.

3.2.2 Heat embossing method to fabricate patterned PP molds.

The quality of PP from three different sources was evaluated before fabricating patterned PP molds. PP ordered from GoodFellow and U.S. Plastic Corp were both in the form of flat film and could be heat embossed directly. PP provided by the collaborator was in the form of pellets, and these pellets were first flattened to form films before heat embossing. Generally, the heat embossing method works by heating the polymer sample until it was softened into a molten stage, and pressure was given to drive the filling of polymer in the negative mold cavities. After cooling down, the sample could be peeled off from the negative mold. During this process, significant factors affecting the quality of embossed samples included heating temperature, heating time, pressure, and cooling time. These parameters were adjusted for three different PP to reach the best quality, which will be discussed in section 3.3.2. Based on the comparison between three PP samples, PP pellets were finally selected to fabricate molds for all patterns. The detailed procedure is shown below.

PP pellets were first heated up on the blank Si substrate at $200\text{ }^\circ\text{C}$ for 10 min until they were melted. A second blank Si piece was put on the top, and 100 kPa pressure was applied to flatten the PP pellets. The thickness of the PP film can be controlled by placing spacers on two sides of the PP film. In this study, five 0.13 mm-thick glass

coverslips (Fisherbrand™ 12542B) were stacked up together to work as a spacer, forming the PP film with thickness of 0.65 ± 0.05 mm (Figure 10).

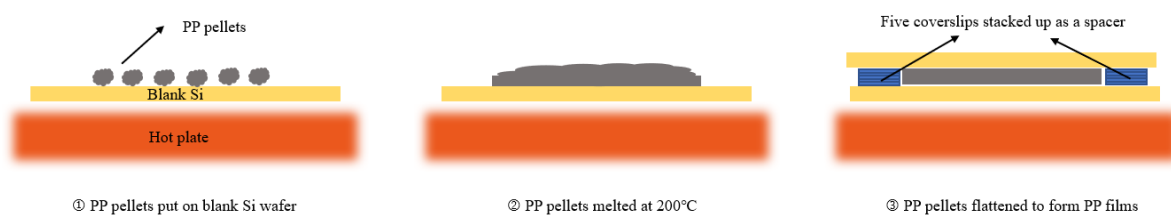


Figure 10. Schematic diagram of PP films formation by flattening melted PP pellets.

The flattened PP film was cut into 2cm width squares, then heated up and softened again at 200 °C for 3 min on a blank Si wafer substrate. The patterned PDMS mold obtained from section 3.2.2 was placed on the PP film with another blank Si piece on the top. A 320 kPa pressure was applied to transfer the pattern from PDMS to PP. Afterward, the whole system was allowed to cool down for 30 min, and the patterned PP sample can be demolded from the PDMS mold (Figure 11).

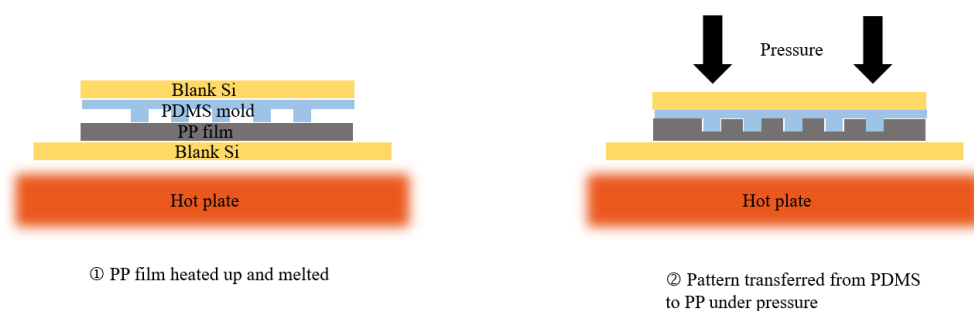


Figure 11. Schematic diagram of PP heat embossing.

3.2.3 Fabrication of patterned SiHy samples.

The embossed PP films were shipped to the collaborator and were used as the mold to fabricate surface patterned SiHy samples. The fabrication method and process details were kept confidential.

3.2.4 PP polymer characterization by FTIR and DSC

Differential scanning calorimetry (DSC; TA Instruments DSC Q2000) was performed following the published protocol to determine the PP melting process and evaluate the crystallinity [145]. $10 \text{ g} \pm 0.1 \text{ g}$ of samples were measured and added into the Tzero Aluminum Hermetic pan. The heating cycle was set from 30 °C to 230 °C at the ramp rate of 10 °C/min. Data were analyzed using the TA Universal Analysis software.

The PP components were analyzed and confirmed by Fourier Transform Infrared (FTIR) spectroscopy following a published protocol [145]. Polypropylene samples were cut into 2 cm x 2 cm squares. The samples were loaded directly into the FTIR for measurement. FTIR spectroscopy was performed using Thermo Fisher Scientific FTIR (Nicolett 6700) fitted with germanium and a high sensitivity pyroelectric detector. Percent transmittance of the samples were collected between 400 cm^{-1} and 4000 cm^{-1} . Sixty-four scans were acquired at a spectral resolution of 4 cm^{-1} .

3.2.5 Topography characterization of PP molds and SiHy samples

3.2.5.1 Industrial 3D laser confocal measuring microscope

To obtain structure dimensions and a large area uniformity of pattern transfer, all surface patterned PP films and SiHy samples were characterized under the 3D laser measuring microscope (LEXT OLS5000). Magnification up to 800X was used.

3.2.5.2 Atomic force microscopy (AFM)

ScanAsyst-in-Air mode of Bruker Dimension FastScan AFM imaging was used to investigate the pattern dimensions at the center area of PP samples and SiHy samples. Image processing was performed with NanoScope Analysis version 1.8.

The FastScan AFM head and ScanAsyst-Air AFM probe were loaded to characterize the surface topography of PP samples. PP molds were cut into 3 mm diameter square pieces and mounted on the AFM specimen discs using the carbon tape. The laser beam was first aligned on the AFM probe tip, and the reflected laser beam was then aligned at the center of the AFM split photodiode using the side controls. The cantilever was brought into focus after the region of interest was found. The scan rate was set to be 1.5 Hz and sample/line was set to be 256. The Feedback and Peak Force Tapping parameters was automatically adjusted to optimize the images.

The Icon AFM head and ScanAsyst-Air AFM probe were loaded to obtain the SiHy surface topography. The operation of SiHy samples characterization was similar to that of PP samples. The alignment of the laser, cantilever and photodiode system was still adjusted in the setup tab, and the scan rate was set to be 1 Hz (Figure 12). However, SiHy samples were first air-dried for 6 hours and mounted on sample discs prior to AFM characterization because the ScanAsyst-in-Air mode was designed only to handle dry substrates or films and the ScanAsyst-in-Fluid mode was not available. The piezo Z-position was monitored during the scanning to make sure that the piezo was operating within its normal range.

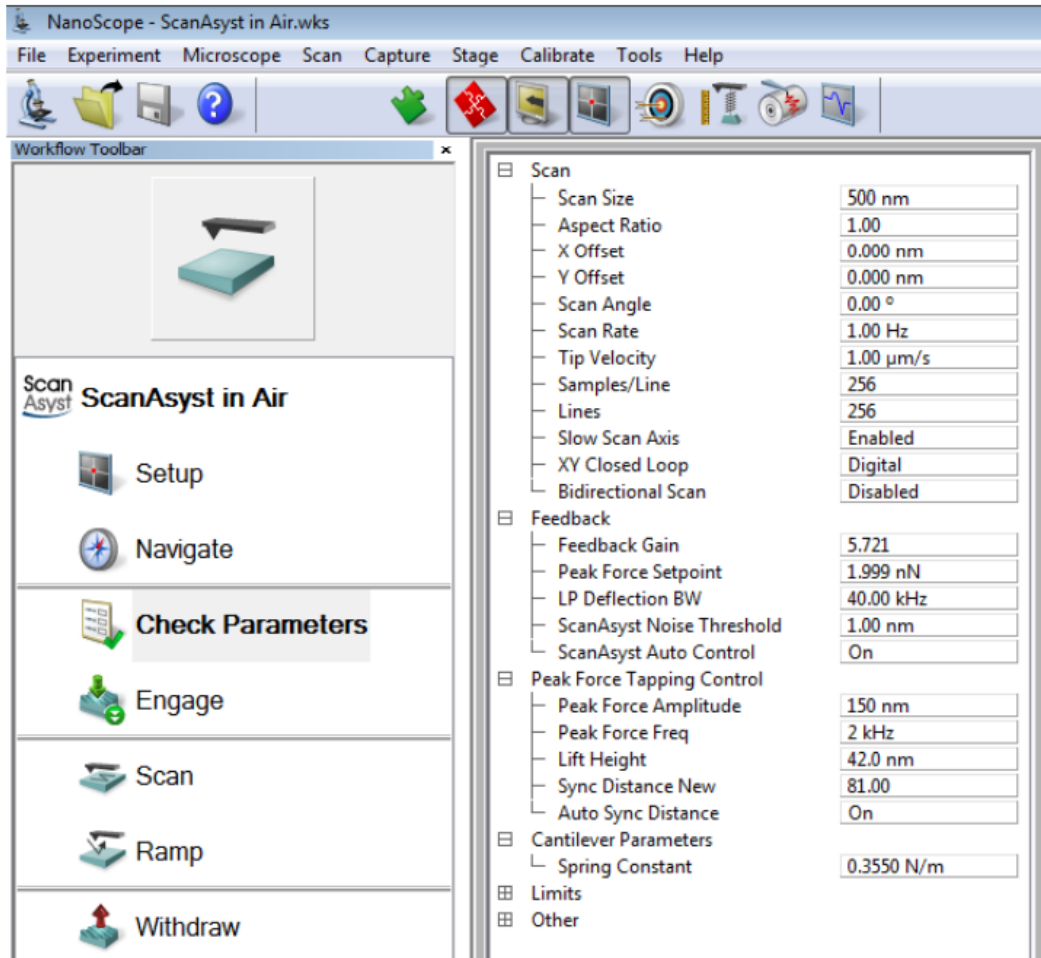


Figure 12. Scan parameters could be adjusted prior to starting a scan or during the scan.

3.3 Results and discussion

3.3.2 Si wafer fabrication

Micro and submicron patterns were successfully fabricated from UV lithography and e-beam lithography, respectively. The pattern dimensions were characterized through the AFM. The fidelity of structure diameter and spacing distancing was within 15% from the expected value, while the fidelity of structure height was within 40% from the expected value due to excessive etching.

3.3.2 PP Molds development

The quality of PP molds was significant for patterned SiHy fabrication. Any defects existing on PP molds could be transferred to SiHy samples along with patterns. Three different PP samples came from U.S. Plastic, GoodFellow and the collaborator were characterized through Fourier-transform infrared spectroscopy (FTIR) and Differential scanning calorimetry (DSC) to analyze the difference between them.

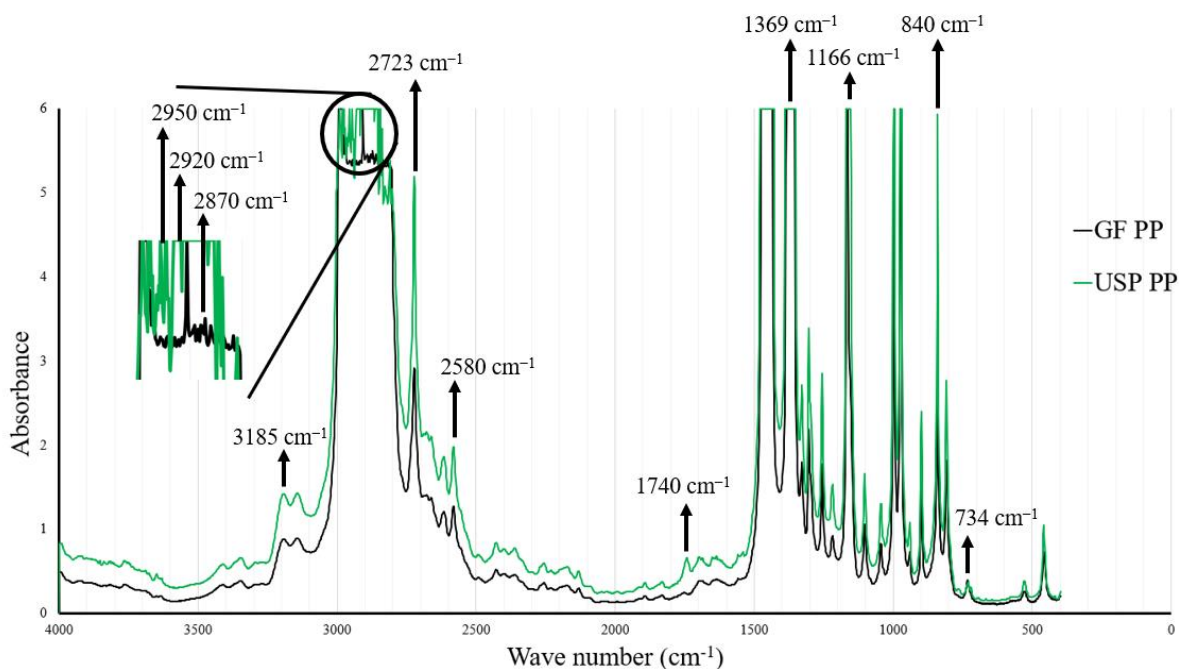


Figure 13. FTIR analysis of PP from U.S. Plastic (green) and GoodFellow (black).

The FTIR spectra of USP PP and GoodFellow PP are shown in Figure 13. The FTIR data of PP pellets were removed as required by our collaborator. All three spectra show large peaks at 2920 cm^{-1} , which represents the CH_2 -group asymmetrical stretching vibration in the main PP polymer chain [146]. Also, three spectra show numerous high peaks in the wavelength range $3000\text{--}2800\text{ cm}^{-1}$. The peak at 2950 cm^{-1} should be due to asymmetrical stretching of the CH_3 -group, and the peak at 2870 cm^{-1} can be attributed to CH_3 -group stretching [146]. The spectra of GF PP and USP PP show small peaks in the range $780\text{--}700\text{ cm}^{-1}$, which can be due to the weak cis- CH -group out-of-plane-bending. The peak at 1166 cm^{-1} is caused by CO -group stretching vibration; the peak at 1369 cm^{-1} is attributed to CH_3 -group out-of-plane bending vibrations or CH_2 -group wagging and twisting vibrations [147]. Comparing the GF PP and USP PP spectra, we noticed that USP PP exhibited higher peaks than GF PP at almost all wavelengths, which means the number of functional groups associated with the molecule should be higher. According to the product information provided by the manufacturer, the USP PP was a homopolymer, while the GF PP was a PP/PE copolymer.

Figure 14 and Figure 15 below show the DSC curves of USP PP and GF PP. Again, the DSC data of PP pellets provided by our collaborator was removed. The identification of polymer depends on both the melting temperature and the enthalpy of fusion, which is the area under the peak. All three PP showed an endothermic peak at around $160\text{ }^\circ\text{C}$, referring to their melting points. During the cooling process, we observed slightly larger difference between their recrystallization temperature, with GoodFellow PP exhibiting the highest at $127.62\text{ }^\circ\text{C}$ and USP PP showing the lowest at $114.76\text{ }^\circ\text{C}$.

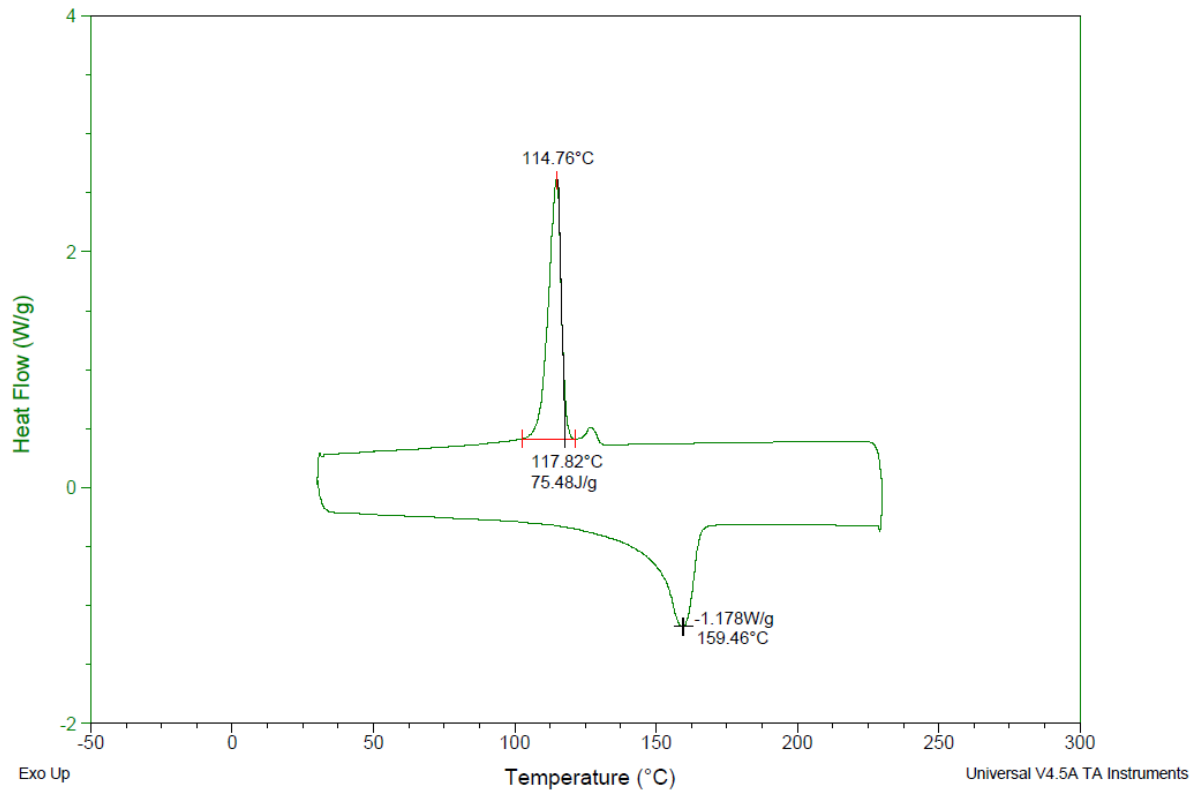


Figure 14. DSC analysis of U.S. Plastic PP.

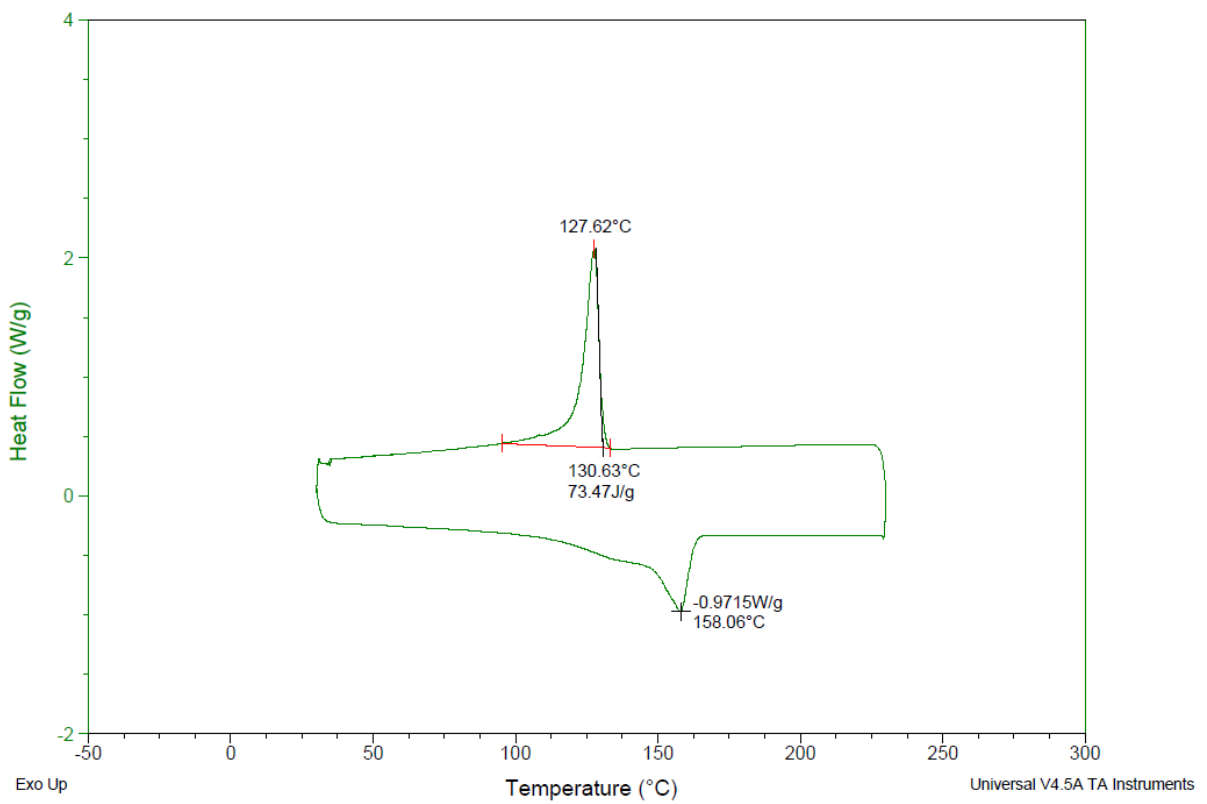


Figure 15. DSC analysis of GoodFellow PP.

PP from three different sources were also heat embossed and investigated to compare their qualities.

3.3.2.1 U.S. Plastic Corp. PP (item # 46017)

The first type of PP was purchased from U.S. Plastic Corp. This homopolymer PP sheet was translucent in color, and it could be heat-formed or shaped. Initially, the PP film was placed on two glass slides on the hotplate and heated at 200 °C for 4 min. Then a 320 kPa pressure was applied, and the hotplate was turned off after 90 s to start cooling the whole system. After cooling for 15 min, the patterned PP sample was demolded from the PDMS mold.

However, surface undulations were observed on the patterned PP samples. One potential reason for the undulation was uneven heat conduction. As is shown in Figure 16, the gap between two slides and any unevenness could cause the uneven heat conduction and undulation. To solve this problem, the glass slides were first replaced by a blank Si wafer as the Si wafer has higher thermal conductivity [148] and can provide a larger and more flat area for the PP film. Although it was easier to handle the PP sample on the Si wafer, the undulation was still observed.



Figure 16. Glass slides (left) and Si wafer (right) worked as the heating substrate.

Insufficient cooling could be another reason for the undulation because wrinkle formation of thermoplastics could result from high temperature [149, 150]. Therefore, we increased cooling time to see if the undulation could be removed. As is shown in table 4, when the whole system was cooled down for 10 min, the temperature of the PP sample was 126 °C. When the temperature was decreased to 45 °C, the undulation was not observed anymore.

Table 4. PP temperature decreased versus time.

	Condition 1	Condition 2	Condition 3	Condition 4	Condition 5
Cooling time (min)	0	10	20	30	40
Temperature (°C)	200	126	88	45	21

When the embossed PP sample was characterized under the 3D laser microscope, another problem was brought into attention. The initial roughness of this PP was different on two surfaces that one was much rougher than the other (Figure 17). After heat embossing, defects with a size up to 2 μm were still observed, whichever surface the PP was embossed on, and even higher pressure or temperature could not help removing such defects (Figure 18). As is shown in Figure 19, the areal roughness of the patterned sample was measured using the confocal microscope. Among all the area roughness parameters, arithmetical mean height Sa is more commonly used to evaluate the roughness of a surface. It shows the difference in height of each point compared to the arithmetical mean of the surface. The Sa value of the USP blank PP sample is 0.889 μm, since most of the patterns evaluated in this project were in submicron size, such defects cannot be neglected because they could either damage the pattern or have their own effect on the surface properties.

Moreover, the thickness of the USP PP was 0.79±0.05 mm, and our collaborator found that the fabrication

of SiHy samples from thicker PP molds was more challenging than from thinner PP films made from PP pellets.

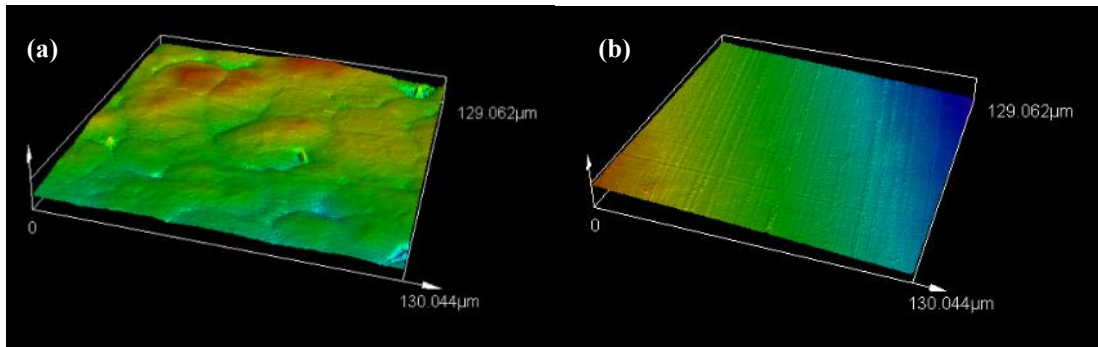


Figure 17. Two surfaces of USP PP had different roughness. One surface was rougher (a), and the other surface was smoother (b).

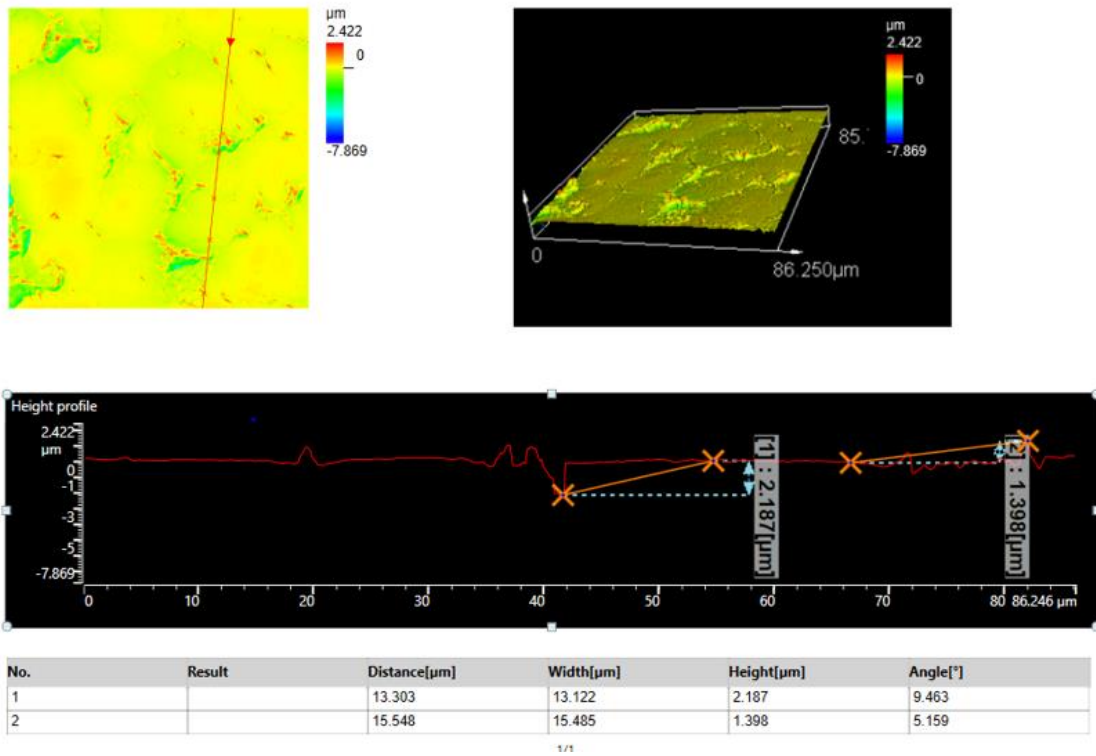


Figure 18. Defects up to 2 μm observed on embossed USP PP film under the 3D laser confocal microscope.

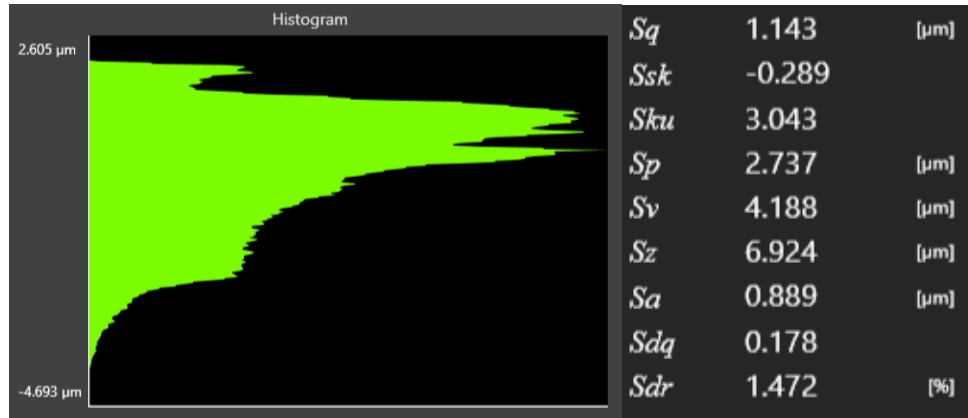


Figure 19. Areal roughness measurement of blank USP PP sample. Root mean square height (Sq), Skewness (Ssk), Kurtosis (Sku), maximum peak height (Sp), maximum pit height (Sv), maximum height (Sz), arithmetical mean height (Sa), root mean square gradient (Sdq) and developed interfacial area ratio (Sdr) were measured.

3.3.2.2 GoodFellow PP (order code 802-942-05)

The second PP film ordered from GoodFellow was a semi-opaque thermoplastic with a thickness of 0.5 ± 0.05 mm. It comprised a PP core layer and a PP/PE copolymer outer layer. Based on the experience from U.S. Plastic PP, the GoodFellow PP film was heated on the Si wafer and cooled down for 30 min to ensure that there was no undulation problem. The pressure applied during the embossing was still 320 kPa.

Although the surface of the PP film was flat and smooth originally, micro-roughness in the shape of dimples and pits were observed on the PP surface after heat embossing (Figure 20). We again measured the surface roughness of this sample. As shown in Figure 21, blank GoodFellow PP sample exhibited a Sa value of $0.033 \mu\text{m}$, which was much lower than that of USP PP sample.

However, when these PP samples were embossed with patterned molds, we observed that the defects could still affect the pattern uniformity, especially when these surface structures are in the submicron size. As is shown in Figure 22, the size of the defects was much larger than pattern dimensions. We tried to increase the pressure and heating time but failed to remove these defects. Such roughness could be created by the interaction between different monomer units of the copolymer [151].

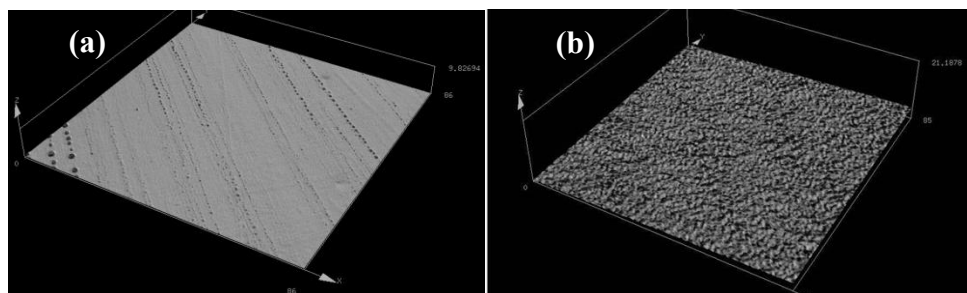


Figure 20. GoodFellow PP was smooth originally (a) but became rough after heat embossing (b).

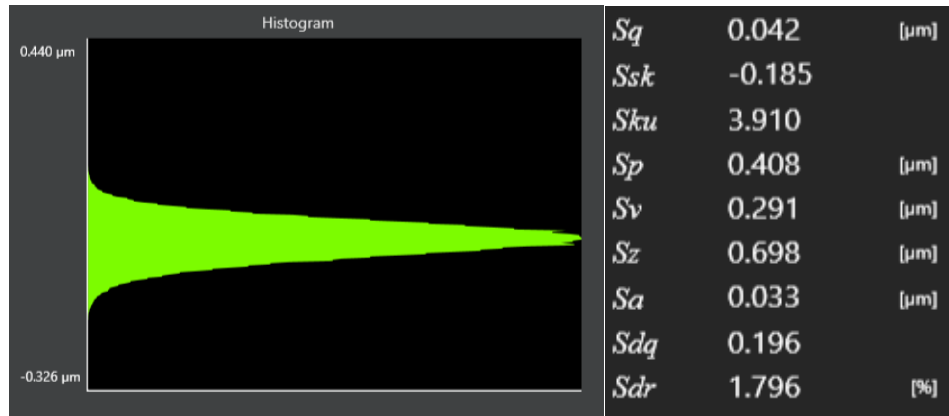


Figure 21. Areal roughness measurement of blank GoodFellow PP sample. Root mean square height (Sq), Skewness (Ssk), Kurtosis (Sku), maximum peak height (Sp), maximum pit height (Sv), maximum height (Sz), arithmetical mean height (Sa), root mean square gradient (Sdq) and developed interfacial area ratio (Sdr) were measured.

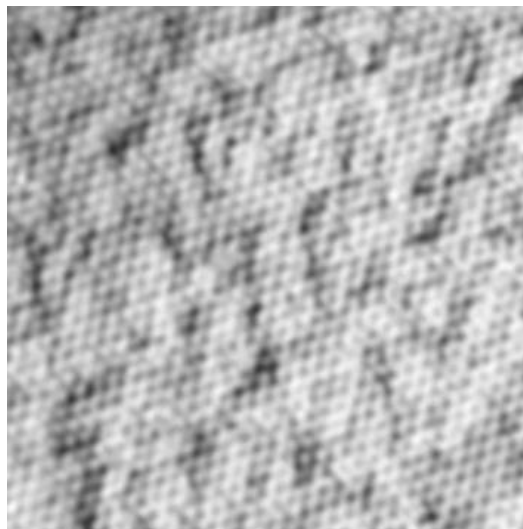


Figure 22. The uniformity of the pattern was affected by the defects.

3.3.2.3 PP pellets provided by the collaborator

The collaborator provided the third type of PP. As described in section 3.2.2, PP pellets were sandwiched between two pieces of Si to fabricate flat PP films. Then the PP films were embossed under 320 kPa at 200 °C with PDMS molds. Undulations were also observed on embossed PP films, as is shown in Figure 23, the height difference throughout the surface was around 0.2 μm , which can be ignored compared to dimensions of most patterns. Based on the areal roughness measurement, the Sa value of this blank PP sample was 0.036 μm , which was very close to the GoodFellow PP film. Also, the whole sample was smoother, and we did not observe large defects that could damage the submicron patterns (Figure 25). Therefore, PP from the collaborator was selected for the fabrication of all PP molds in this project.

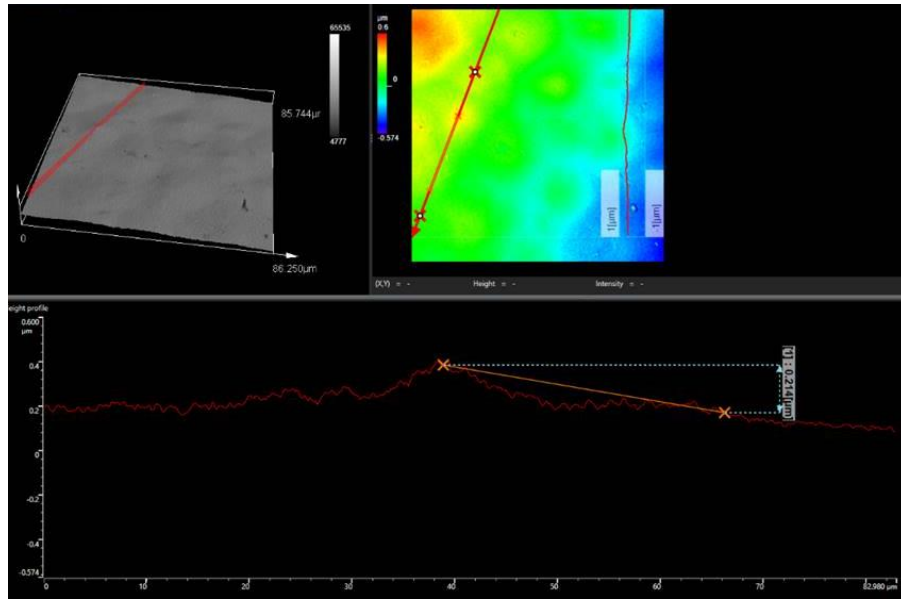


Figure 23. Surface of the flat PP film made from PP pellets under the 3D laser confocal microscope.

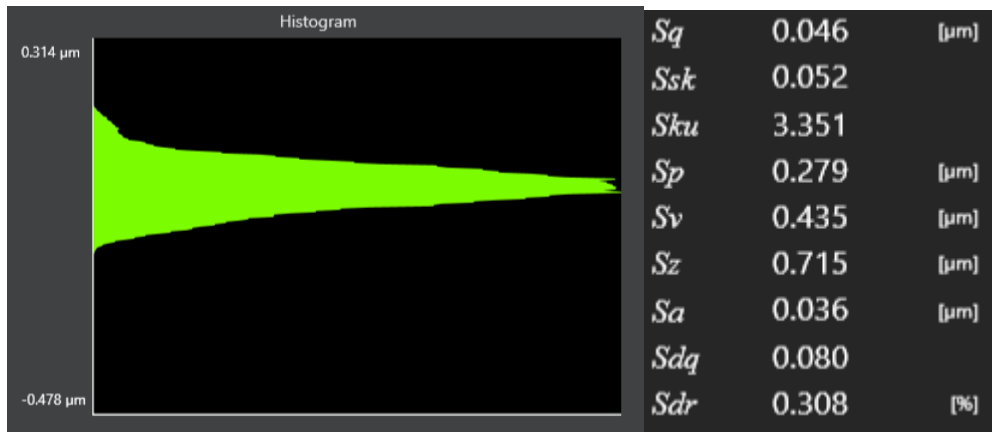


Figure 24. Areal roughness measurement of blank the collaborator PP sample. Root mean square height (Sq), Skewness (Ssk), Kurtosis (Sku), maximum peak height (Sp), maximum pit height (Sv), maximum height (Sz), arithmetical mean height (Sa), root mean square gradient (Sdq) and developed interfacial area ratio (Sdr) were measured.

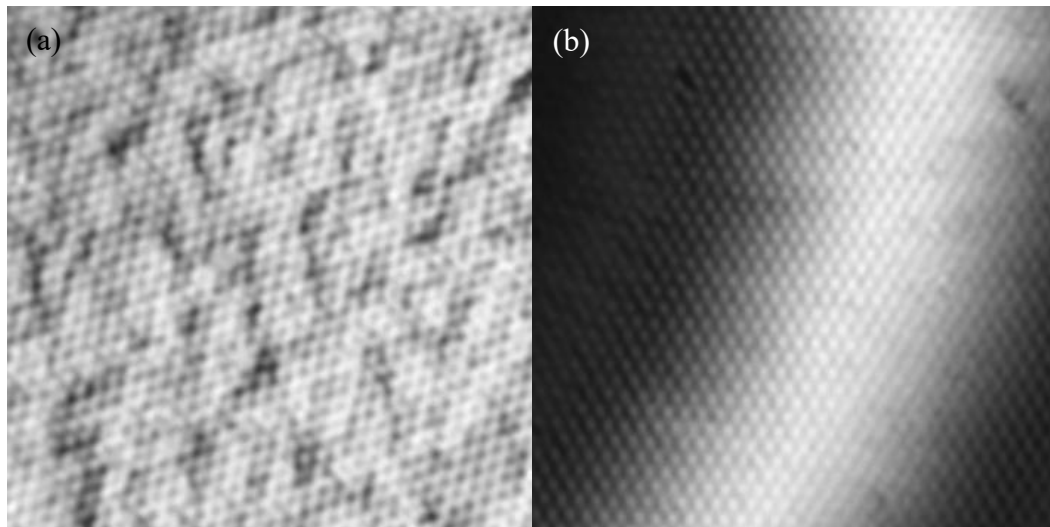


Figure 25. The collaborator PP (b) showed better pattern quality than GoodFellow PP (a).

3.3.3 Surface topography characterization of PP molds and SiHy samples

During the hydrogel sample fabrication process, the pattern fidelity could be affected by the fabrication method. To obtain the actual structure dimensions, 3D laser confocal microscope and AFM were used to measure the pattern parameters.

For Si samples, images could be easily obtained with high resolution and less noise when the structure was larger than $1\ \mu\text{m}$. For structures smaller than $1\ \mu\text{m}$, the confocal could still exhibit good lateral resolution, but axial resolution was reduced. For example, Figure 26 shows the 3D height image of pattern 32 on Si wafer. The expected depth of this structure was D . The actual depth of the well was confirmed using AFM to be $1.03D$, while the depth measured with confocal microscope was only $0.624D$.

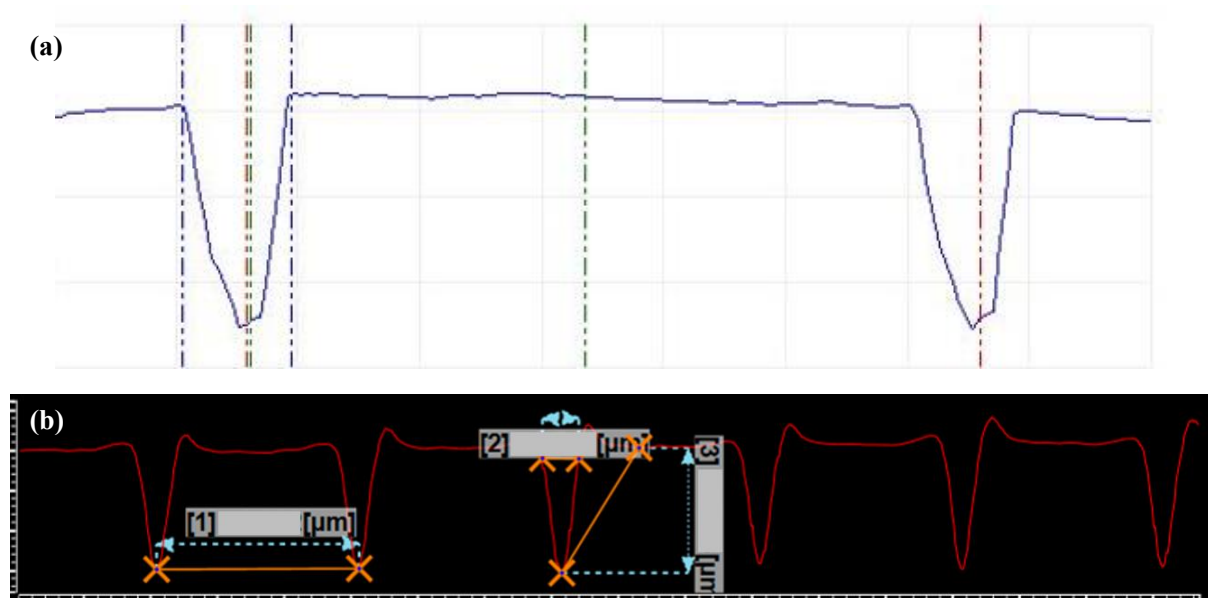


Figure 26. The same Si sample was characterized with both AFM (a) and confocal microscope (b). It was more difficult for confocal microscope to get the actual dimension of submicron structures than AFM.

For submicron patterned PDMS or PP samples, it was more challenging to achieve an excellent resolution, as their refractive index is much lower than that of Si material. Poor resolution problems also happened to hydrogel samples because they were usually hydrated and transparent with an even lower refractive index like air or water. Therefore, it was not easy to have their topography accurately characterized with only the confocal microscope. It was necessary to confirm the measurement of the confocal microscope with AFM.

Here, the ScanAsyst-Air AFM probe was selected to characterize the PP and SiHy samples. The spring constant of this probe is 0.4 N/m, and the tip radius is around 2 nm. During the scanning, it was important to monitor the force curve because it could tell whether the probe was working properly. Figure 27(a) shows that the cantilever stuck to the sample surface during the scanning, while Figure 27(b) indicates that probe bent too hard. The expected force curve is shown in Figure 27(c). During the characterization, we stopped the scanning when we observed force curve shown in Figure 27(a) and (b) and restarted the scan.

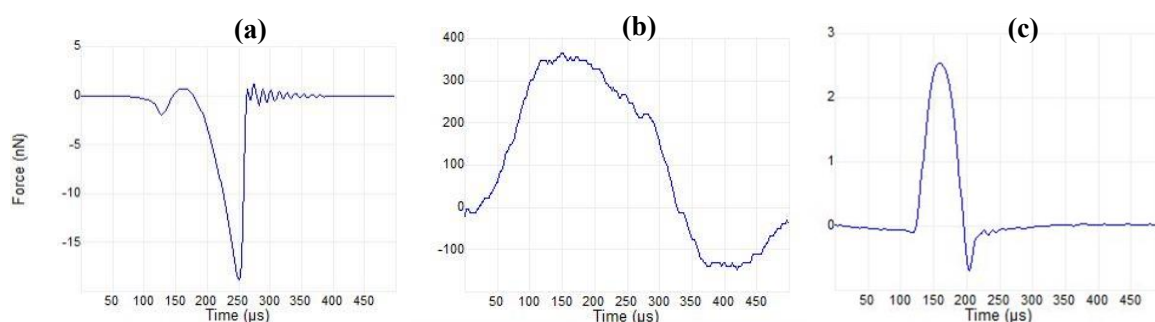


Figure 27. The force curve showed the force that the cantilever is undergoing during each oscillation cycle. The cantilever did not work properly in (a) and (b) and work well in (c).

In addition to the force curve, we also need to care about the position of the piezo stack. If the scalebar was green, then the piezo was operating within its normal range. The scalebar would turn yellow or red if it got too close to its limits of extension, and the image quality would be poor if the piezo operates at its limit and piezo damage could occur from extended operation in this range. When the AFM was characterizing the SiHy samples, the scalebar tended to approach its limit especially when the scan area was large. Therefore, we could not scan a very large area for SiHy samples.

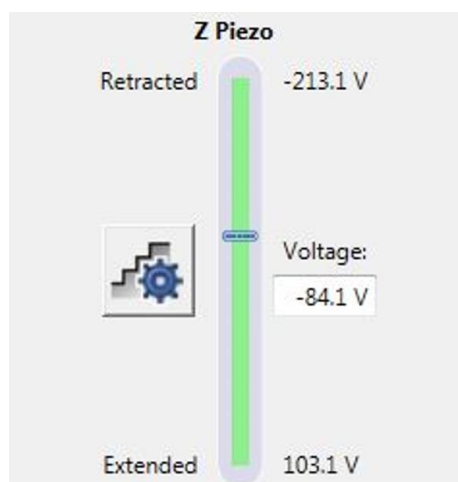


Figure 28. The scalebar should be in green during the scanning to guarantee the image quality and protect the AFM.

Moreover, as our AFM was not equipped with the fluid mode and wet samples were not possible, all SiHy samples were first dehydrated in the air for 6 hours and then mounted on the sample discs using the carbon tape before the characterization. Therefore, the measured pattern dimensions of the hydrogel samples can be different from that of the hydrated hydrogel samples due to their deswelling behavior upon dehydration.

Figures 29-32 show the surface topography of surface patterned PP molds and SiHy samples. When the pattern was transferred from the mold to the substrate, we found it more difficult to maintain the height than the diameter and the spacing distance. The loss of height could happen when the sample did not completely fill into the mold. Therefore, when making the PDMS replica from the Si wafer, we always needed to treat the sample with a vacuum because the vacuum could help to force the PDMS solution into the small structures. Also, the pressure used in PP heat embossing should be high enough so that the melted PP could fill into the mold as much as possible. However, decrease in height was still observed during the pattern transfer. As is shown in Table 5, the pattern transfer fidelity in height was calculated for Si molds, PP samples and SiHy samples. For Si wafers fabricated at UW QNC, the heights were slightly higher than the expected value due to excessive etching. As mentioned above, height loss could happen during the pattern transfer, so it would be better to have a larger height than a smaller one. Table 5 showed that the fidelity of structure height was within 10% from the expected value for all patterns except pattern 11, 13n, 18, 21, 22 and 27, among which pattern 11, 13n and 27 had smaller height than expected, and pattern 18, 21 and 22 had larger height than expected.

Before characterizing the SiHy sample surface properties, their surface topographies were characterized to compare with the theoretical dimensions. The fidelity of structure height was within 30% from the expected value for most of the patterns. Such a decrease in height mainly came from the deswelling of hydrogels in the air. Because the AFM was only equipped with the air mode, we had to dry the SiHy samples before the characterization.

PP Topography Characterization (Confocal Microscope)

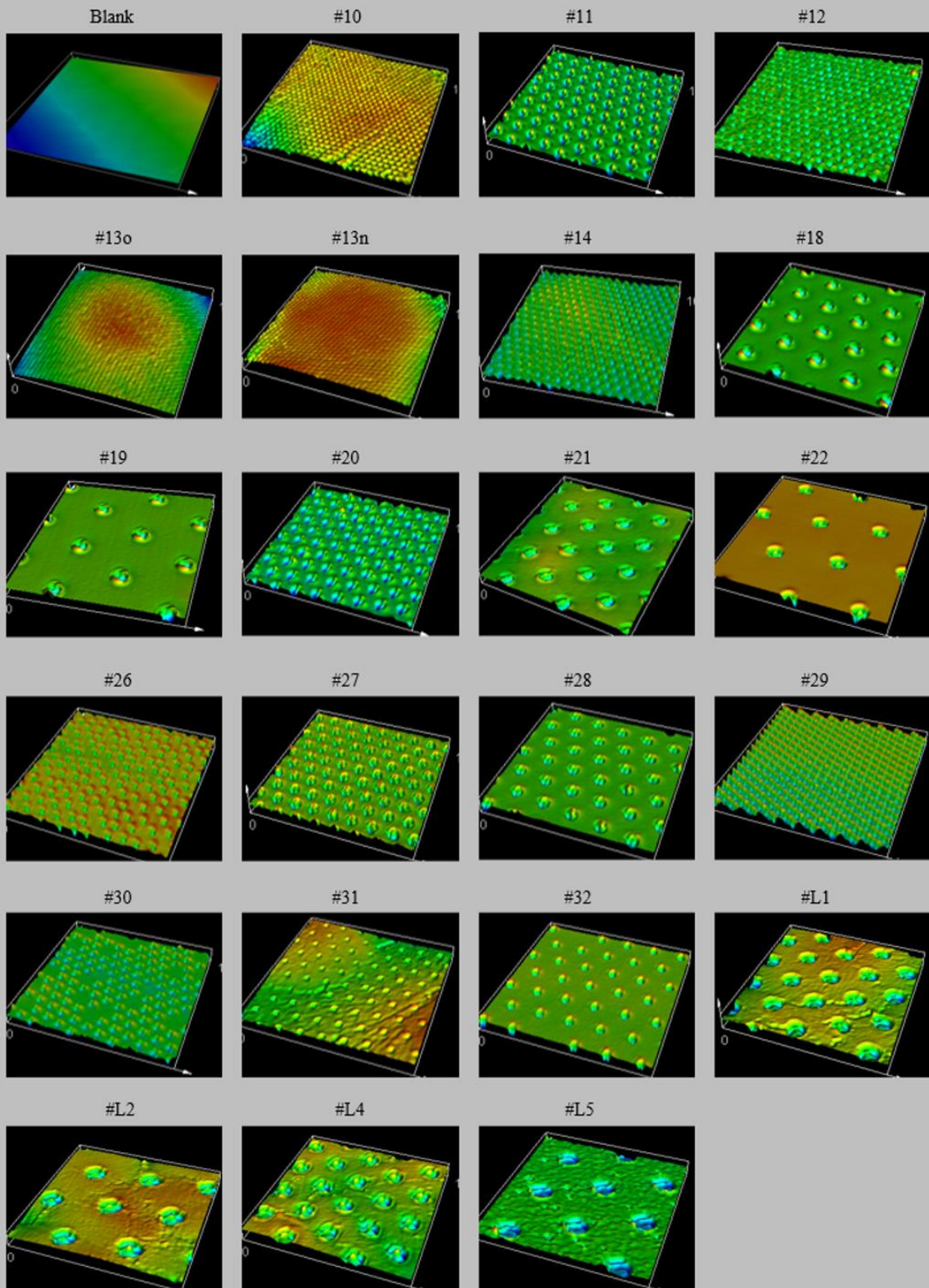


Figure 29. 3D confocal laser images of patterned PP surfaces.

PP Topography Characterization (AFM)

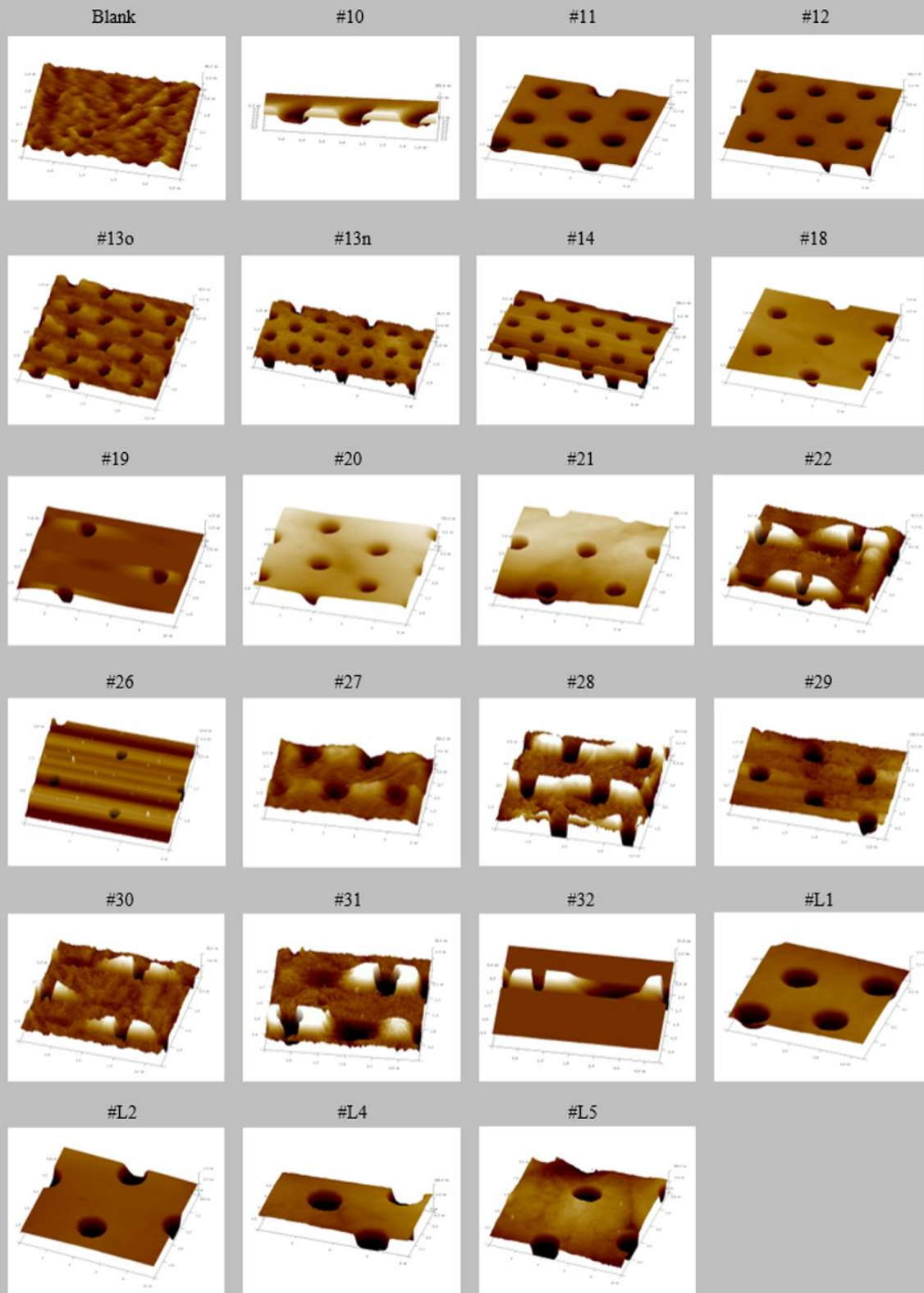


Figure 30. AFM images of patterned PP surfaces.

SiHy Topography Characterization (Confocal Microscope)

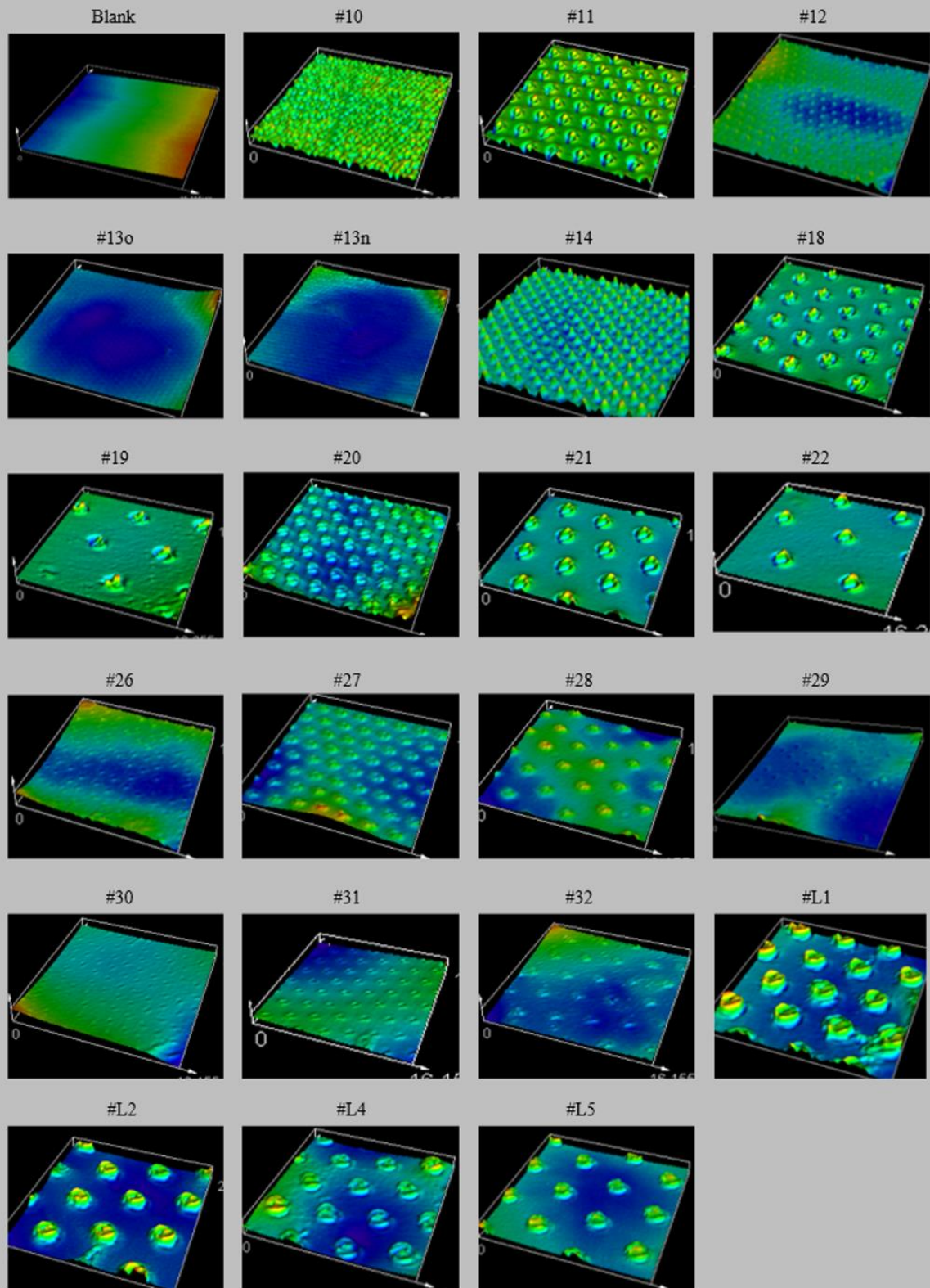


Figure 31. 3D confocal laser images of patterned SiHy surfaces.

SiHy Topography Characterization (AFM)

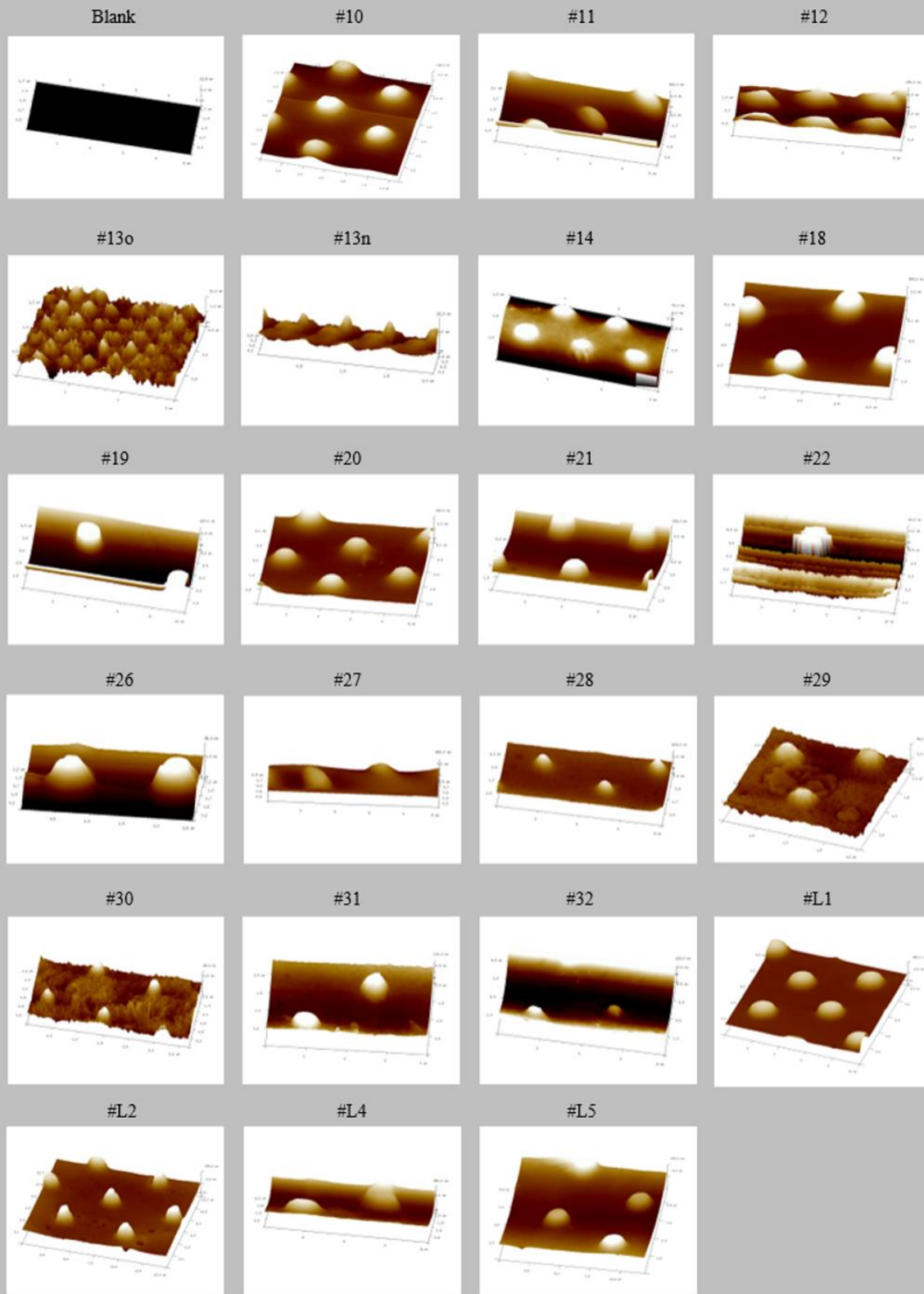


Figure 32. AFM images of patterned SiHy surfaces.

Table 5. Pattern transfer fidelity

Pattern number	Submicron or micro	Actual dimension	Aspect ratio	Si fabrication derivation from theoretical dimension (height) $\frac{Si - expected}{expected} \times 100\%$	PP replication fidelity derivation from theoretical dimension (height) $\frac{PP - expected}{expected} \times 100\%$	SiHy replication fidelity derivation from theoretical dimension (height) $\frac{SiHy - expected}{expected} \times 100\%$
Blank	/	/	/	/	/	/
10	Submicron	/	1.1	107.98%	110.60%	63.44%
11	Submicron	/	1	88.93%	75.94%	68.05%
12	Submicron	/	1	119.95%	105.96%	35.70%
13o	Submicron	/	0.2	103.67%	85%	64.94%
13n	Submicron	/	0.5	69.23%	62.95%	20.56%
14	Submicron	/	0.5	95.82%	90.73%	39.83%
18	Micro	/	1	142.84%	119.97%	80.60%
19	Micro	/	1	136.70%	102.76%	91.27%
20	Micro	/	0.5	/	106.93%	72.99%
21	Micro	/	0.5	131.93%	116.10%	76.24%
22	Micro	/	0.5	127.12%	117.98%	77.75%
26	Submicron	/	1	104.28%	96.22%	51.68%
27	Submicron	/	1	/	70.13%	68.35%
28	Submicron	/	1	/	106.70%	46.01%
29	Submicron	/	0.5	119.2%	103.71%	75.2%
30	Submicron	/	0.5	117.84%	96.01%	55.76%
31	Submicron	/	0.5	111.13%	99.41%	69.56%
32	Submicron	/	0.5	103.13%	102.58%	70.68%
L1	Micro	/	0.5	102.3%	93.65%	72.66%
L2	Micro	/	0.5	107%	109.96%	56.82%
L4	Micro	/	0.25	111.4%	93.89%	74.50%
L5	Micro	/	0.25	120%	100.15%	87.10%

3.4 Conclusion

In this chapter, three different PP materials were evaluated to reduce the defects on the patterned PP molds. The hot-embossed USP PP film generated the highest surface roughness compared to others. The measured areal roughness of the hot-embossed GoodFellow PP film and the collaborator PP film were close to each other. However, when we looked into their detail surface characterization of patterned films, we noticed that the collaborator PP film had a much smoother surface that both microstructures and submicron structures were maintained in good quality. The heat embossing method was then used to fabricate the patterned PP molds. The optimal embossing parameters for PP were 200 °C heating, 320 kPa pressure, and 30 min cooling. Before shipping the PP molds to the collaborator, the pattern dimensions were characterized with both a confocal microscope and an AFM. The confocal microscope mainly worked to check the large area uniformity of pattern transfer, and the AFM was used to obtain the actual dimensions of the patterns. The characterization data showed that the fidelity of structure height on PP molds was within 10% from the theoretical value for all patterns except pattern 11, 13n, 18, 21, 22 and 27, among which pattern 11, 13n and 27 had smaller heights than expected, and pattern 18, 21 and 22 had larger heights than expected.

After receiving the patterned SiHy samples, we again used the confocal microscope and AFM to characterize the structures on the SiHy surface. Due to the transparency of SiHy samples, it was more challenging to obtain their dimension accurately. We loaded the ScanAsyst-Air probe and Icon head for hydrogel characterization because the ScanAsyst-Air probe has a lower spring constant, and the Icon head could support a larger scanning area. Based on the characterization result, all patterns, except pattern 12, 13n, 14, 26, 28 and 30, had a fidelity within 35% from the theoretical dimension due to the deswelling behavior of the hydrogel, which was consistent with our expectation.

Chapter 4 Surface energy characterization and functional characterization of patterned SiHy samples

4.1 Introduction

After characterizing the surface topography of SiHy samples, we then performed surface wettability test, lipid deposition test and bacterial adhesion test on these samples. Water contact angle is one of the most significant parameters that can describe the material surface wettability. The value of the contact angle tells whether a surface has higher or lower wettability. In this chapter, captive bubble method was used to measure the water contact angle of patterned SiHy samples, and we aimed to find the samples showing higher wettability by comparing their contact angle values. These samples were then incubated in artificial tear solution (ATS) to evaluate the lipid deposition. Lipid 1 and lipid 2 were chosen as two model lipids for this study. Lipid 1 is a hydrophobic lipid while lipid 2 is an amphiphilic lipid, both are components of tear. We hypothesized that when topographies altered the surface energy, the amount of lipid deposited onto the sample could also be affected.

Bacteria 1 (Gram-negative, ATCC®) and *bacteria 2* (Gram-positive, ATCC®) are two different common bacteria that can adhere onto SiHy contact lenses and cause eye diseases. In this chapter, they were allowed to adhere onto the surface patterned SiHy samples to evaluate the antibacterial function of those topographies. Gram negative bacteria are the predominant causative agents in contact lens-related microbial keratitis, with *bacteria 1* species being the most commonly isolated organism [7, 152]. *Bacteria 1* have been shown to adhere to contact lens surfaces more easily than many other pathogens. Therefore, this section could be more focused on the *bacteria 1* on patterned SiHy samples, and only selected patterns were tested with *bacteria 2*.

In addition to finding specific patterns that could work well to improve the SiHy performance in these three aspects, we would also like to figure out the relationship between topography dimensions and hydrogel surface properties. Thus, principal component analysis (PCA) was performed at the end to analyze the correlation between these variables.

4.2 Materials and methods

4.2.1 Water contact angle (WCA) measurement

The water contact angle measurement was performed using the optical contact angle measuring device (Dataphysics, OCA 25) at Center for Ocular Research & Education (CORE), University of Waterloo (Figure 33a). The OCA 25 is an all-purpose measuring device for contact angle measurements and drop shape analysis. The sample holder was designed by our former lab member Grace Pohan, and Chau-Minh Phan in Dr. Lyndon Jones's lab helped with the 3D-printing of the holder (Figure 33b). This apparatus was used to understand the hydrophilicity of surface patterned SiHy samples. The SiHy sample was first mounted on the custom-made sample holder through two rubber bands and stabilized in DI water. An inverted needle connected to a syringe full of air was placed under the sample so that air bubbles could be pumped out and adhered to the sample surface.

As is shown in Figure 34, 5 μl air was pumped out at a dosing rate of 2 $\mu\text{l/s}$ for static contact angle measurement. For measuring receding and advancing contact angle, 6 μl air was pumped out continuously at a rate of 2 $\mu\text{l/s}$ for 3 s to enlarge the air bubble, and then the bubble volume was shrunk at the same rate by selecting the "Rev. Disp." option in the SCA20_F software. This entire process was captured as a digital movie, and the movie can be split into multiple continuous pictures for further analysis.

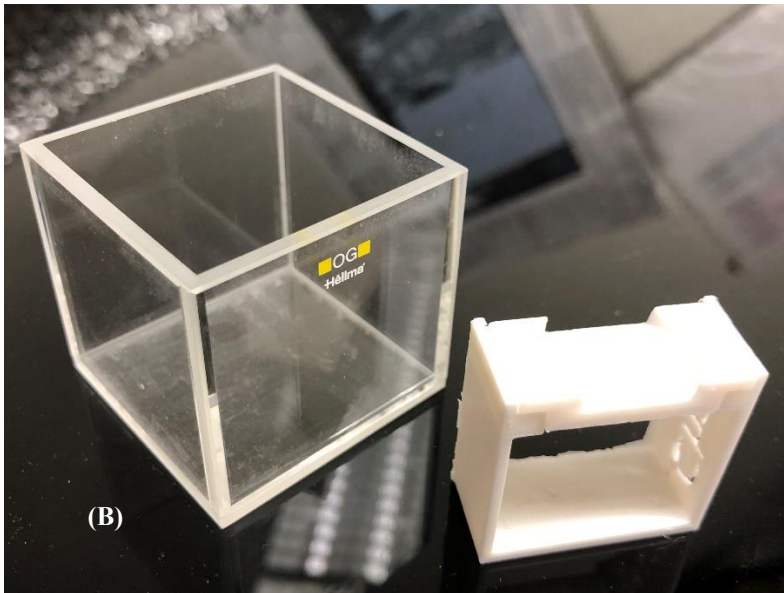
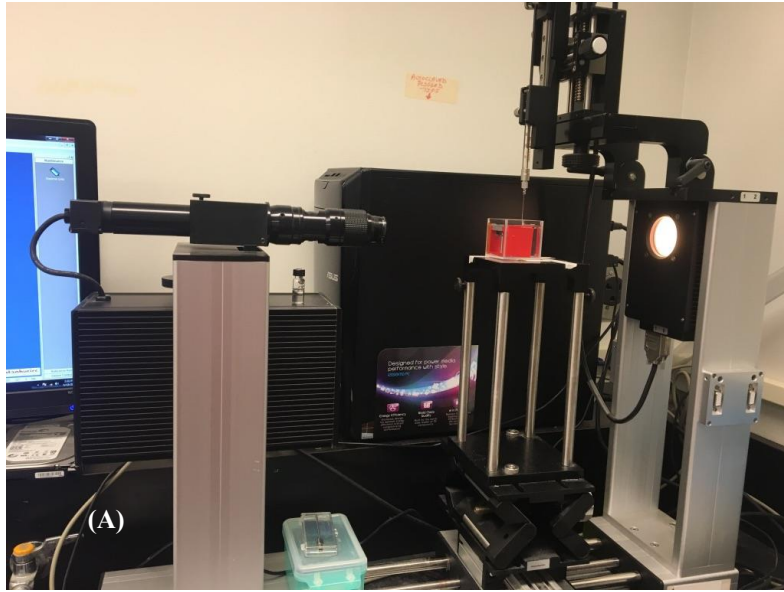


Figure 33. OCA 25 captive bubble apparatus for wettability measurement (A) and 3D printed sample holder (B).

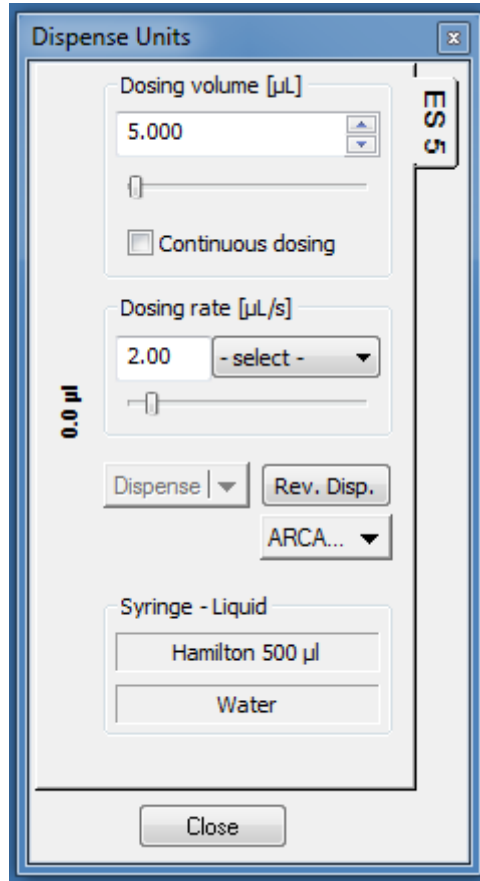


Figure 34. Adjustable settings for captive bubble measurement.

4.2.2 Lipid deposition test

4.2.2.1 Commercial hydrogel lenses for benchmarking lipid deposition protocol

Different commercial lenses were used in the preliminary tests to guarantee that the experimental setup in section 4.2.2.6 was proper and effective. The four hydrogel lenses were comfilcon A, omafilcon A, senofilcon A and lotrafilcon B. All lenses were removed from their blister pack solutions and placed in 12-well plates, with 2 mL of the complex salt solution (CSS). They were soaked for 24 hours, while being gently rotated at 60 rpm, to remove any residual blister pack solution.

Table 6. Four commercial hydrogel lenses used for preliminary lipid deposition test.

USAN	Material type	Proprietary name	Manufacturer	Water content
Comfilcon A	Silicone hydrogel	Biofinity	CooperVision	48%
Omafilcon A	HEMA hydrogel	Proclear	CooperVision	62%
Senofilcon A	Silicone hydrogel	Acuvue OASYS	Johnson & Johnson	38%
Lotrafilcon B	Silicone hydrogel	Air Optix	Alcon	33%

4.2.2.2 Preparation of the complex salt solution (CSS)

The individual components were measured on an analytical balance and sequentially added to the desired volume of DI water in the order that they are listed in Table 7. The complex salt solution was then filtered to remove any dusts.

Table 7. Concentration of components used to prepare complex salt solution [153].

Salt component	Molecular formula	mM
Sodium chloride	NaCl	110
Potassium chloride	KCl	16
Calcium chloride	CaCl ₂	0.5
Sodium carbonate	Na ₂ CO ₃	12
Potassium hydrogen carbonate	KHCO ₃	3
Sodium phosphate monobasic	NaH ₂ PO ₄	26

4.2.2.3 Preparation of lipid tear solution (LTS)

Six non-radioactive lipids were all ordered from Sigma-Aldrich. C-14 lipid 1 and C-14 lipid 2 were ordered from PerkinElmer.

Pure lipids were first warmed up to room temperature and weighed out using an analytical balance (solid lipids) or pipetted using a positive displacement pipette (liquid lipids). Then the six lipids above were dissolved in the solution of 1 hexane: 1 methyl tert-butyl ether to obtain the lipid stock solution. The concentrated lipid stock solution could be placed in an amber vial, sealed with Parafilm®, wrapped in foil, and stored at -20 °C.

When required, the lipid stock solution was removed from the freezer and warmed up again to room temperature in a dry, dark place. The desired volume of lipid stock solution was added to the complex salt solution and mixed thoroughly in the fume hood for an hour. The C-14 lipid was then added to the solution. Due to the extremely high cost of radioactive materials, the C-14 lipid was added at a concentration of 5.6% of the total individual lipid concentration, and the total radioactivity could also be decreased to a safer level.

Table 8. Molecular and experimental details of lipids used in all lipid deposition tests [153].

	Triolein	Cholesterol	Oleic acid	Oleic acid methyl ester	Cholesteryl oleate	Phosphatidyl choline
Lipid Type	Triglyceride	Sterol	Fatty acid	Fatty ester	Cholesteryl ester	Phospholipid
Formula	C ₅₇ H ₁₀₄ O ₆	C ₂₇ H ₄₆ O	C ₁₈ H ₃₄ O ₂	C ₁₉ H ₃₆ O ₂	C ₄₅ H ₇₈ O ₂	C ₄₂ H ₈₂ NO ₈ P
Molecular Weight (g/mol)	885.5	386.7	282.5	296.5	651	760.1
Lipid Stock Concentration (mg/ml)	32.0	3.6	3.6	24.0	48.0	1.0
Final ATS Concentration (mg/ml)	0.016	0.0018	0.0018	0.012	0.024	0.0005

4.2.2.4 Preparation of artificial tear solution (ATS)

The proteins and mucin were weighed out on an analytical balance and added to the lipid tear solution while stirring. When all components were fully incorporated, the complete ATS was sonicated at 37 °C for a maximum of 5 minutes to prevent destruction of the proteins.

Table 9. Molecular weight and concentration of proteins in ATS.

Proteins	Molecular weight (kDa)	Concentration (mg/ml)	Lot #
Bovin serum albumin	66.4	2.0	SLBZ6977
Lysozyme from chicken egg white	14.3	1.9	SLBZ8428
Mucin from bovine submaxillary glands	3×10^5 to 4×10^7	0.15	SLCC3392

4.2.2.5 Glass vial incubation

Fisherbrand™ 7mL borosilicate glass scintillation vials were used for all hydrogel samples incubation and were pre-treated with non-radioactive ATS for one to two days at 37 °C with a constant shaking of 150 rpm, to saturate the inside surface with lipid and protein prior to the radioactive ATS incubation. Following pretreatment, the vials were emptied, rinsed with PBS, and radioactive ATS (with either 14C-lipid 1 or 14C-lipid 2) was added.

4.2.2.6 Experimental setup for lipid deposition and lipid extraction

The hydrogel sample was mounted on the cap of the 7 mL glass scintillation vial with the patterned surface facing outside. The inner diameter of the foil-lined cap was 15 mm, and the 16 mm diameter SiHy sample could perfectly fit into the cap. After adding 0.75 ml ATS into the vial, the cap was slowly screwed on, and the hydrogel sample could be stabilized inside the cap without dropping out or being broken.

Vials were placed onto the rotating rocker of the brand tube rotator, and the custom mode was used for sample incubation with the following parameter: 180° clockwise rotation --- 180° clockwise rotation --- level 1 shaking 15 s --- pausing 99 s. As shown in Figure 35, the sample was exposed to the air and ATS intermittently to mimic the air exposure during eye blinking. All the vials were capped, sealed with Parafilm®, and incubated at 37 °C for 10 hours. Three replicates of each pattern were tested (n=3). At the end of the 10 hours, each sample was rinsed in two successive vials, each containing 2 mL of PBS, to remove loosely bound incubation solution.

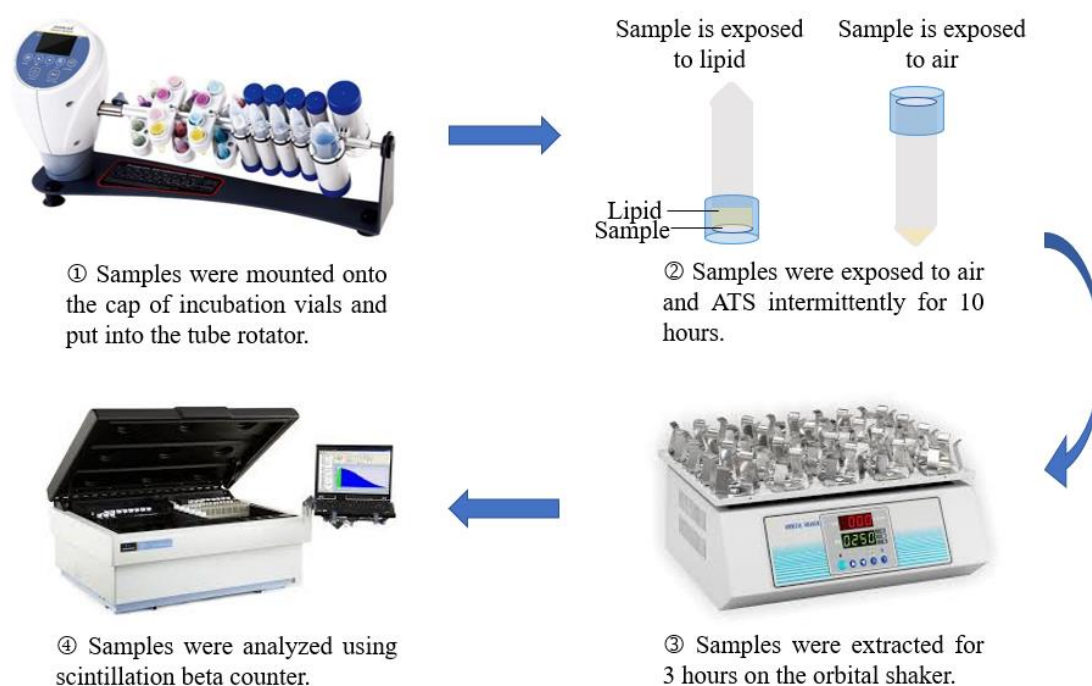


Figure 35. Experimental setup for lipid deposition and extraction.

The lenses were then put into 20 ml glass scintillation vials with 2 mL of (2:1) chloroform: methanol (v/v) extraction solution. All vials were covered with parafilm and sealed with the aluminum foil to prevent evaporation and were incubated for three hours at 37 °C while shaking on an orbital shaker at 150 rpm. After the extraction, each sample was placed in a new blank 20 ml scintillation vial, and all vials, including extracts and extracted lenses, were dried out in the fume hood overnight. Then all samples were resuspended in 0.4 mL of chloroform, sonicated for one minute, and 4 ml of Ultima Gold F scintillation cocktail (PerkinElmer) was added. Finally, the vials were characterized in the PerkinElmer scintillation beta counter, and the mass of deposited lipid of each sample could be calculated from the radioactivity results (see equations below).

$$activity (dpm) = \frac{activity (cpm)}{efficiency\ of\ detector}$$

$$1\ Ci = 2.22 \times 10^{12}\ dpm$$

$$lipid\ mass\ (g) = \frac{activity\ (Ci) \times lipid\ molar\ mass\ (\frac{g}{mol})}{specific\ activity\ (\frac{Ci}{mol})}$$

4.2.2.7 Fluorescence imaging

The adsorption and absorption of lipid 1 and lipid 2 were analyzed with Zeiss LSM700 confocal microscope using fluorescently labelled lipids. The TopFluor® lipid 1 and TopFluor® lipid 2 were ordered from Avanti. The comfilcon A commercial lenses were soaked in 1X PBS for 24 h at 60 rpm and cut into 5 mm diameter circles. Then these samples were incubated in the 96 black well plate for 24 h at 37 °C. Each well contained 100 µm fluorescently labelled lipid solution. All samples were washed three times with 1xPBS prior to subsequent characterizations.

The absorption profile was investigated by using z-stack function of 350 µm thick samples and 50 µm step. The surface of the sample was identified as the lowermost slice. Image processing and mean gray value measurement were then performed with ImageJ software.

4.2.3 Microbial adhesion test

4.2.3.1 Commercial hydrogel lenses for benchmarking bacterial adhesion protocol

Two commercial hydrogel lenses were used in the preliminary test, which were lotrafilcon A (AirOptix Night and Day Aqua) and etafilcon A (Acuvue2). In order to reduce the impact of inhibitory agents in the lens packaging solution, lenses were soaked in autoclaved PBS solution overnight prior to evaluation in the bacterial adhesion assay.

Table 10. Two commercial hydrogel lenses used for preliminary bacteria adhesion test.

USAN	Material type	Proprietary name	Manufacturer	Water content
Lotrafilcon A	Silicone hydrogel	AirOptix Night and Day Aqua	Alcon	24%
Etafilcon A	HEMA hydrogel	Acuvue2	Johnson & Johnson	58%

4.2.3.2 Bacterial strains tested

The adhesion of *bacteria 1* and *bacteria 2* onto surface patterned SiHy samples were evaluated in this project.

For each pattern type, n=5 replicates were examined under study. According to the product sheet, *bacteria 2* strains were cultured at 37 ± 1 °C using tryptic soy broth (TSB) and tryptic soy agar (TSA), while *bacteria 1* strains were cultured at 26 ± 1 °C using nutrient broth (NB) and nutrient agar (NA).

4.2.3.3 Culture preparation

An overnight TSB culture of *bacteria 2* was prepared from the stock culture plate and cultured at 37 °C on a 110 rpm orbital shaker for 18 hours. The culture was spun down at 5000 rpm for 2 min and washed with autoclaved PBS for two times. The optical density (OD) reading at 600 nm was checked and recorded by using the plate reader. TSA agar plates were prepared in advance, and the concentration of the bacteria inoculum was confirmed through the plate counting method. The inoculum level was around 10^8 CFU/ml.

The procedures of *bacteria 1* inoculum preparation were the same as that of *bacteria 2*, except the temperature and the culture media.

4.2.3.4 Primary adhesion method

Sterile polystyrene 24-well tissue culture plates were used for sample incubation. Each sample under study was aseptically transferred from its packaging to an individual sample case well. The patterned surface of sample was placed uppermost for bacteria adhesion. An autoclaved silastic ring was used to mount the sample at the bottom of the 24-well tissue culture plate. Two milliliters (2 mL) of the $\sim 10^8$ CFU/mL inoculum was dispensed into each well containing a sample.

The well plate was then incubated at bacteria's optimal temperature for 2 hours on an orbital shaker to allow bacteria to adhere to the sample surface. After incubation, the sample was aseptically removed from the culture plate with sterile forceps and rinsed via immersion for 5 times in each of three successive sterile PBS solution. Rinsing could remove associated cells that were not firmly attached to the sample.

Afterward, each sample was placed into a 20 ml sterile scintillation vial containing 2 mL of PBS for extraction and recovery.

4.2.3.5 Bacteria extraction and recovery

Each scintillation vial with sample inside was sonicated (30 kHz) for 60 seconds and immediately put onto the vortex for 30 seconds to remove bacteria adhered to the sample. Plate counting method was then applied to confirm the cell concentration of each sample. Agar plates were incubated for 24 to 72 hours at optimal temperature and the average CFU/ml of each pattern was calculated.

4.2.4 Statistical analysis

All statistical analyses found in this chapter were computed using Microsoft Excel and GraphPad Prism 9. One-way ANOVA analysis with Tukey and Dunnett post-hoc test, and parametric t tests were used in the analysis. Three replicas of each pattern were used for all tests (n=3).

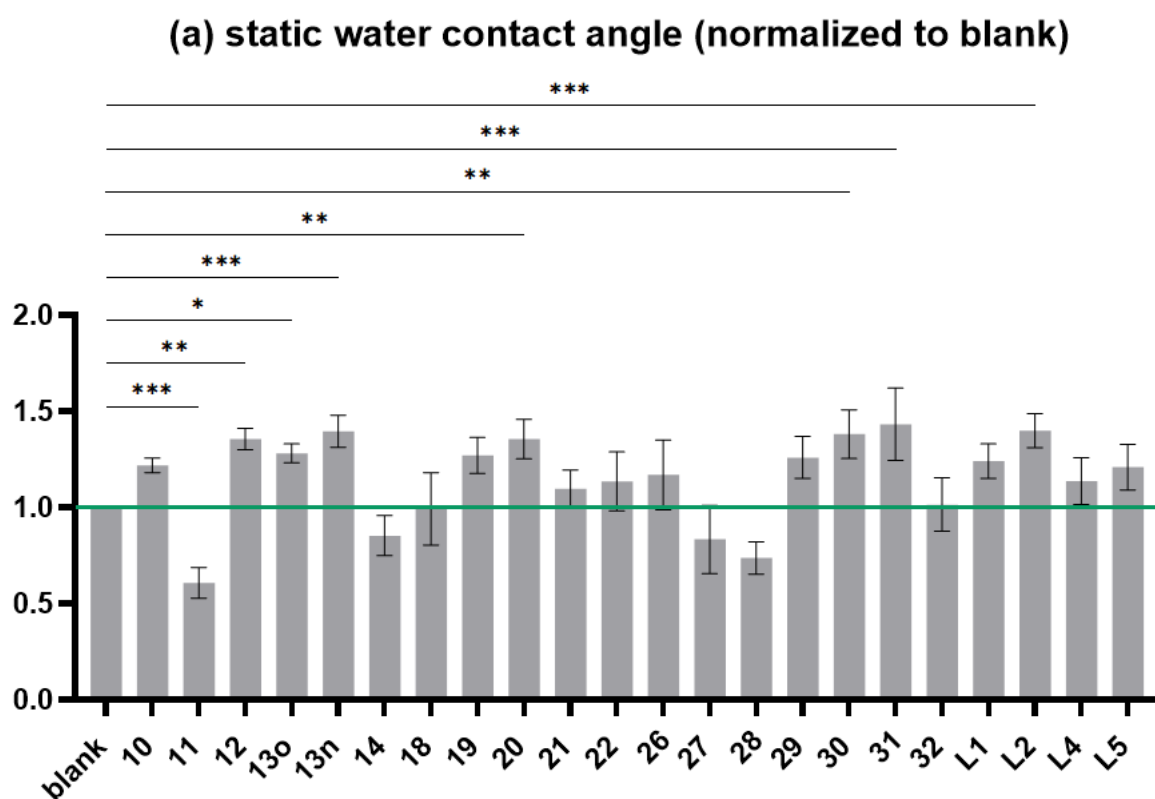
4.3 Results and discussion

4.3.1 Static water contact angle

The degree of wetting refers to the ability of a liquid to spread on and maintain contact with a solid surface, and the wettability shows how a solid surface can be wetted. As we mentioned in section 2.2.1, sessile drop method and captive bubble method are two popular ways to measure the material surface contact angle. Generally, the sessile drop is more widely used. However, in this project, the captive bubble method was selected instead. Due to the swelling and deswelling behavior of hydrogel materials, the flat SiHy samples could become curved quickly

when they were outside an aqueous environment. Not only the operation difficulty was increased by such sample deformation, but the dimensions of surface structures could also be changed. In addition, liquid residues could exist randomly between the surface structures, and it was difficult to remove them. All these uncertainties could introduce large experimental errors and lead to inaccuracy of results. Therefore, the captive bubble method was more suitable for hydrogel samples as all samples will be sufficiently hydrated, and their surface structures can be maintained well underwater.

Figure 36(a) shows the static water contact measured for all patterned SiHy samples. The average water contact angles of all patterns were in the range of 20° to 60°, showing that the surface wettability of these SiHy samples was relatively high. Among all samples, pattern 11, 14, 27 and 28 exhibited lower water CA than blank control, which reflected higher wettability of these surfaces. All these four patterns were in submicron scale; therefore, submicron structures could possibly work better to increase the hydrogel wettability than microstructures.



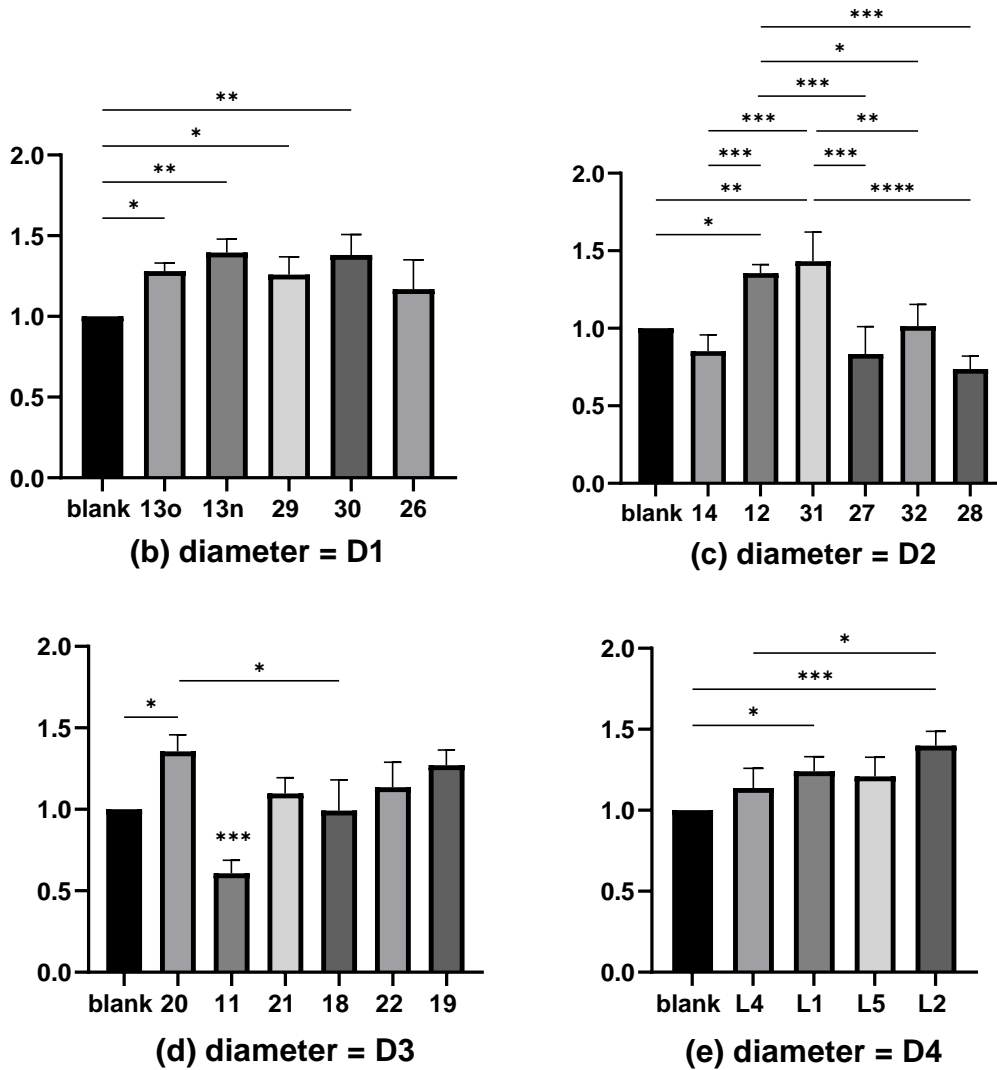


Figure 36. Static contact angle measurement of all surface patterned SiHy samples was shown in figure (a), and patterns were also analyzed in different groups according to their diameters (b) diameter = D1; (c) diameter = D2; (d) diameter = D3; (e) diameter = D4. $D1 < D2 < D3 < D4$. D1 and D2 are in submicron size, D3 and D4 are in micro size. Center-to-center distance increases from left to right in each figure. One-way ANOVA analysis was applied. P value style: < 0.05 (*), < 0.005 (**), < 0.0002 (***), < 0.0001 (****).

When these samples were divided into different groups according to their diameters, we noticed that large center-to-center distance reduced the water contact angle for submicron patterns but increased the water contact angle for micro patterns. However, this relationship was only effective for some of the patterns, and there was no significant difference between these samples.

Maldonado-Codina et al. measured the water contact angle of five different commercial SiHy lenses using both the sessile drop method and the captive bubble method [154]. All lenses were washed in saline for 48 hours to remove the surface-active agents from the packaging solution before the measurement. Contact angles measured using the captive bubble method varied from 30° to 50° for these commercial SiHy lenses, while contact angles of our surface patterned SiHy samples fell within a similar but slightly broader range.

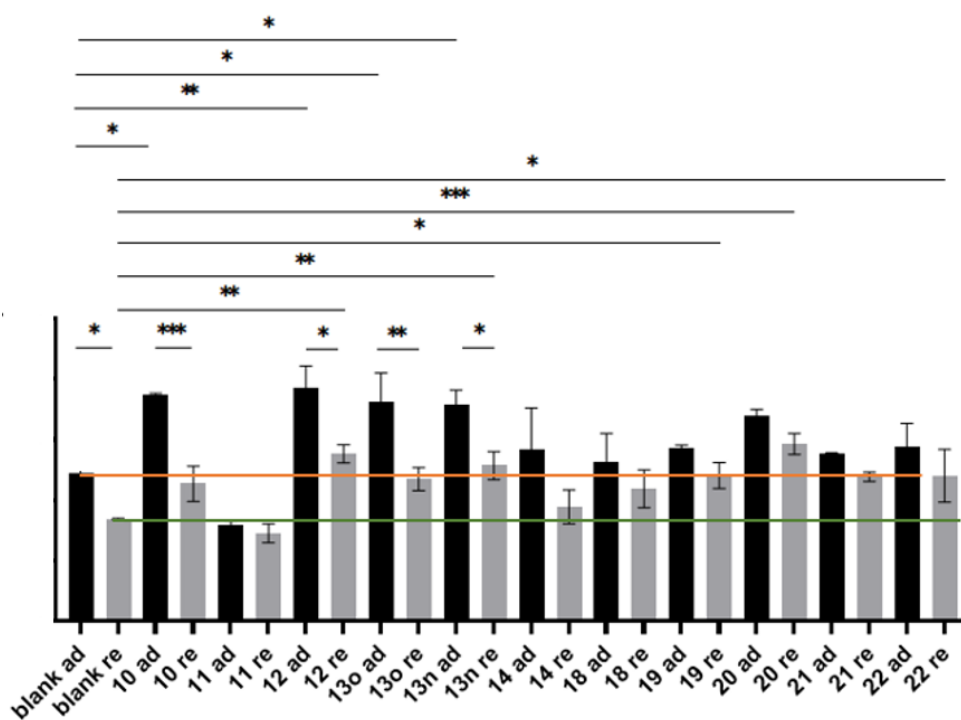
4.3.2 Advancing and receding water contact angle

Dynamic water contact angles were also measured for all samples. The advancing and receding contact

angles were observed to be correlated well. Pattern 11 again showed a lower value than other patterns. However, it would be more meaningful to learn the contact angle hysteresis. As mentioned in section 2.2.1, the contact angle hysteresis refers to the difference between the advancing and the receding contact angle. It shows the activation energy that a droplet needs to change from one metastable state to another. Generally, a surface with higher hydrophilicity would exhibit larger contact angle hysteresis. As is shown in Figure 37, a significant difference was found between advancing and receding contact angle of blank control, pattern 10, 11, 12, 13o, 13n, 27, 30 and #L5. The correlation between the hysteresis and other surface properties will be analyzed in section 4.4.

Dynamic contact angles of 11 commercially available SiHy contact lenses were also measured by Read et al. using the captive bubble method [38]. The advancing contact angles of these lenses varied from 20° to 70°, and the receding contact angles were found to range between 17° and 22°. Compared with these contact lenses, our SiHy samples showed a similar advancing contact angle range, but the receding contact angles were higher. This could be due to the different types of SiHy samples in our study or result from the liquid used in the test, as Read et al. had all lenses immersed in PBS solution, and we used DI water.

Dynamic water contact angle (normalized to blank control)



Dynamic water contact angle (normalized to blank control)

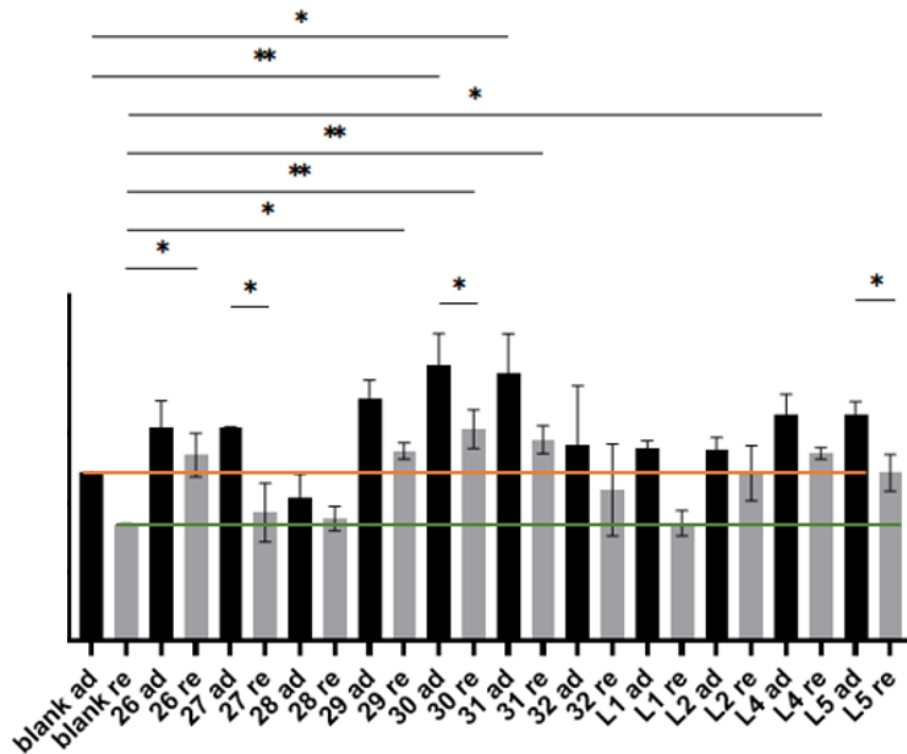


Figure 37. Dynamic water contact angle of surface patterned SiHy samples. One-way ANOVA analysis was applied. P value style: < 0.05(*), < 0.005(**), < 0.0002(***), < 0.0001(****).

4.3.3 Preliminary test to set up lipid deposition test

A preliminary test was performed to select the most suitable tubes for the lipid deposition test. Five parameters were evaluated including the volume and size of the tube, the type and lining of the cap, and the tube material.





Table 11 lists four different candidate tubes/vials that could be used for lipid deposition. The cap of these tubes can be divided into two groups: a snap cap or a screw cap. The cap is the most important factor that should be considered because the hydrogel sample needs to be mounted inside the cap. Since the diameter of the SiHy sample was 16 mm, the inner diameter of the cap should also have a similar diameter so that the sample can fit into the cap more easily. During the 10h incubation, the hydrogel sample should always remain in good shape. If the sample is broken, the lipid deposition can happen on both surfaces of the sample, leading to the inaccuracy or failure of the experiment. Unfortunately, all snap caps broke the sample easily at the beginning and only a screw cap can avoid this. Internal screw cap and external screw cap are two types of screw cap available. We tried both types and we noticed that for the internal screw cap, the lens was also broken easily at the periphery when it was sandwiched between the vial and the cap. Therefore, only an external screw cap met this fundamental requirement, and Teflon or aluminum lined caps are preferred.

The second important factor was the material of the vial. Generally, there were glass vials and plastic vials available. Considering the possibility of lipid deposition onto the vial inner wall, a glass vial was more suitable. Also, as described in section 4.2.2.5, vial incubation was performed to reduce the effect of lipid deposition onto the vial.

Additionally, as the ATS volume used in the experiment was only 0.75 ml per sample, almost all vials were large enough to accommodate this volume.

Considering all these factors, Fisherbrand™ 7ml borosilicate glass scintillation vials were finally chosen for the lipid deposition test in this project.

Table 11. Different types of vials/tubes evaluated for lipid deposition test.

	FisherBrand™ 7mL Borosilicate Glass Scintillation Vial	Thermo Scientific™ Low Protein Binding microcentrifuge tubes	VWR® Centrifuge Tubes	Cryovials
Capacity	7 ml	1.5 ml	15 ml	1.8 / 3.5 / 4.5 ml
Diameter	17 mm	/	17 mm	10 mm
Vial material	Borosilicate Glass	Polypropylene	Polypropylene	Polypropylene
Cap material	Plastic	Polypropylene	HDPE	polypropylene
Cap type	screw	snap	screw	screw
Liner material	cork-backed metal foil liner	/	/	/
photo				

4.3.4 Fluorescent-labeled lipid vs. radiolabeled lipid

To track the amount of lipid deposited onto the hydrogel sample, both fluorescently labeled lipids and radiolabeled lipids (C-14) can be used. The result of fluorescently labeled lipid can be analyzed using the plate reader (BioTek Synergy4) or the confocal microscope, while the result of C-14 lipids can be obtained from the scintillation beta counter.

Comparing these two options, C-14 labelled lipids were selected because the result from the radioactivity analysis is more quantitative and accurate. Also, there is no need to avoid light during the incubation process, which can also reduce the experimental errors.

4.3.5 Effect of scintillation cocktail volume

In this study, liquid scintillation counting technique was applied for radioactivity analysis. The radiolabeled analyte is incorporated into a uniformly distributed liquid chemical medium and the kinetic energy of nuclear emissions can be converted into light energy [155]. All liquid scintillation cocktails contain at least an organic solvent and one or more scintillators. The scintillator molecules are dissolved in the solvent and the role of the scintillator is to absorb the energy released by the solvent and re-emit this energy at a wavelength around 420 nm as visible light.

PerkinElmer Ultima Gold F scintillation cocktail was used in this project due to its high efficiency. To eliminate the uncertainties of the experimental setup, different volumes of the scintillation cocktail were added into radioactive samples with the same amount to evaluate if the cocktail volume could affect the counting result. Therefore, 20 ml scintillation vials were added with 10 ml, 5 ml and 3.5 ml cocktail, and 7 ml scintillation vials were added with 5 ml, 3.5 ml and 1.75 ml cocktail. N=3 replicates were examined for each group. As is shown in Figure 38, for scintillation vials of the same size, the cocktail volume added will not make a big difference. Based on this result, we determined to add 4 ml cocktail into each 20 ml scintillation vial in the experiment.

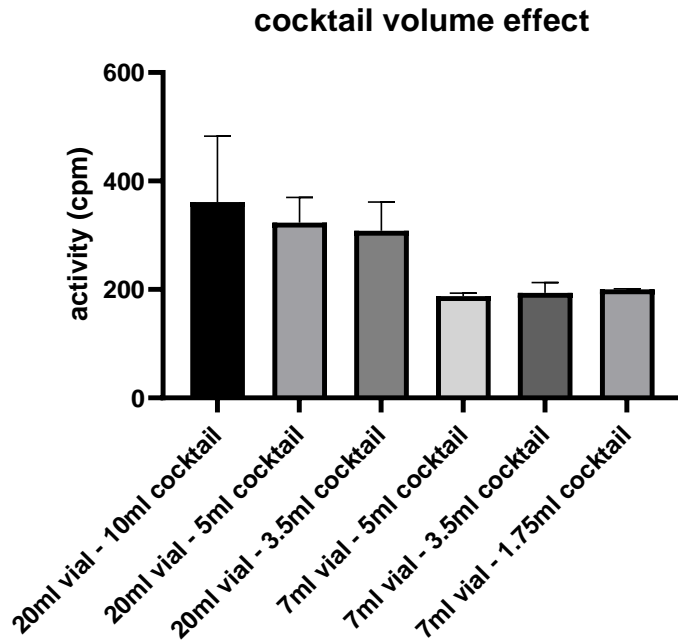


Figure 38. Effect of scintillation cocktail volume to counting results. The cocktail volume did not affect the final counting result and there was no significant effect when considering different cocktail volumes in the same size vial.

4.3.6 Effect of ATS volume and air exposure time

In order to evaluate the experimental setup, preliminary tests were performed on 4 different commercial lenses prior to testing patterned SiHy samples. The four lenses were comfilcon A, omafilcon A, senofilcon A and lotrafilcon B. Each lens was incubated for 10 h with 1.5 ml ATS. In this preliminary test, the pausing time of the rotation system was set to be 60 s only. The result in Figure 39 shows that senofilcon A had most lipid 2 deposition, followed by comfilcon A, lotrafilcon B and senofilcon A, which was consistent with the expected trend.

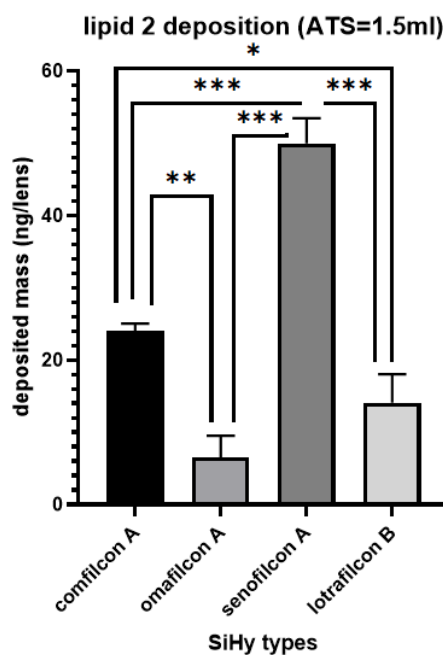


Figure 39. Lipid 2 deposition onto 4 commercial lenses. One-way ANOVA analysis was applied. P value style: < 0.05(*), < 0.005(**), < 0.0002(***), < 0.0001(****).

During the test, we noticed that the ATS volume can also be important. Because the rotation system is a closed system, if the ATS volume is too high, air exposure time will also be reduced, and samples will be difficult to dry down. However, if the ATS volume is too low, the liquid will stick to the corner of the vials and cannot touch the sample mounted on the cap (as is shown in the Figure 40). Therefore, the minimum ATS volume should be around 0.5 ml.

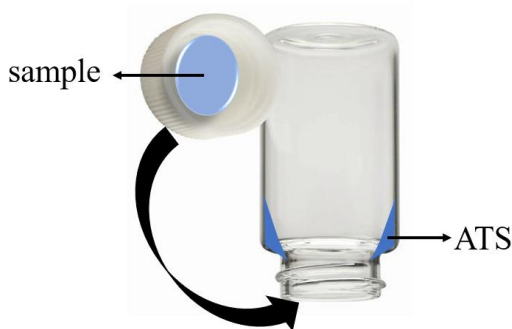


Figure 40. ATS volume cannot be too low.

We tried again with a decreased ATS volume and see if we could observe the same trend. As shown in Figure 41, the test on four commercial lenses was performed again with a decreased ATS volume of 0.75 ml. The result showed that the trend of the mass of deposited lipid 2 on 4 commercial lenses were the same with different ATS volumes. This could be due to the property of lipid 2 that it can soak into lenses more easily and may not be affected by the air exposure time that much.

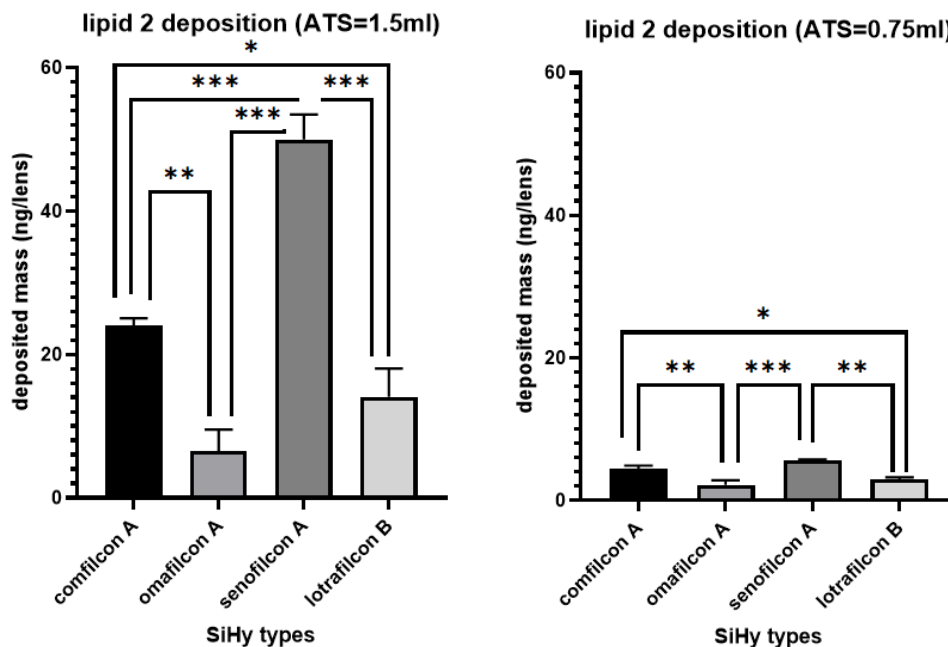


Figure 41. Lower ATS volume resulted in less lipid 2 deposited but the same trend. One-way ANOVA analysis was applied. P value style: < 0.05(*), < 0.005(**), < 0.0002(***), < 0.0001(****).

We then characterized the lipid 1 deposition on these four commercial lenses. The vials were still rotated at 1 rpm and paused for 60 s to allow the air exposure of lenses. At the same time, we also varied the ATS volume

with comfilcon A lenses to check its effect. Again, omafilcon A lenses exhibited lowest lipid 1 deposition (Figure 42), and the ATS volume did not affect the amount of lipid 1 deposited (Figure 43). We therefore introduced “shaking” mode and further extended the air exposure time to 99 s to explore this difference. The “shaking” mode mainly helped to reduce the potential liquid meniscus retained on samples; 99 s was the longest pausing time that the tube rotator could support. As shown in Figure 44, longer air exposure time exhibited lower lipid 1 deposition onto lenses, and no obvious effect was observed on lipid 2 deposition.

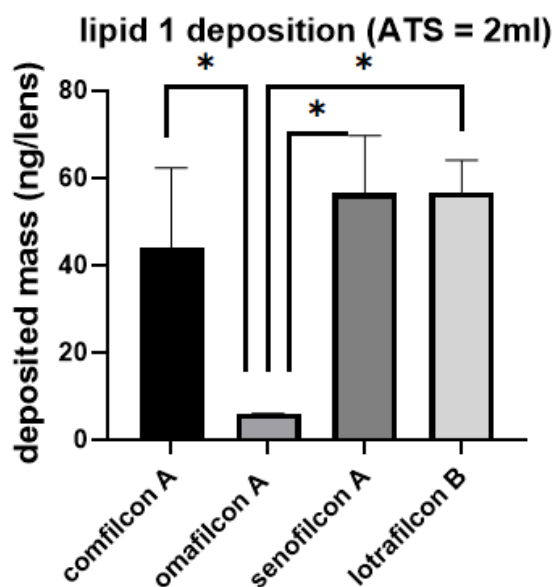


Figure 42. Lipid 1 deposition onto 4 commercial lenses. One-way ANOVA analysis was applied. P value style: < 0.05(*), < 0.005(**), < 0.0002(***), < 0.0001(****).

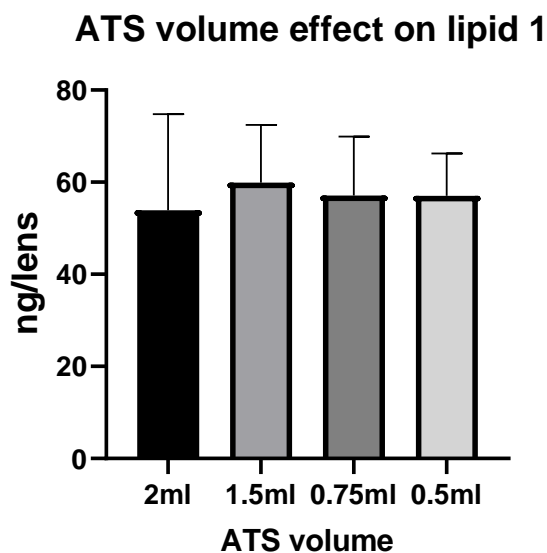


Figure 43. ATS volume did not affect the amount of lipid 1 deposited.

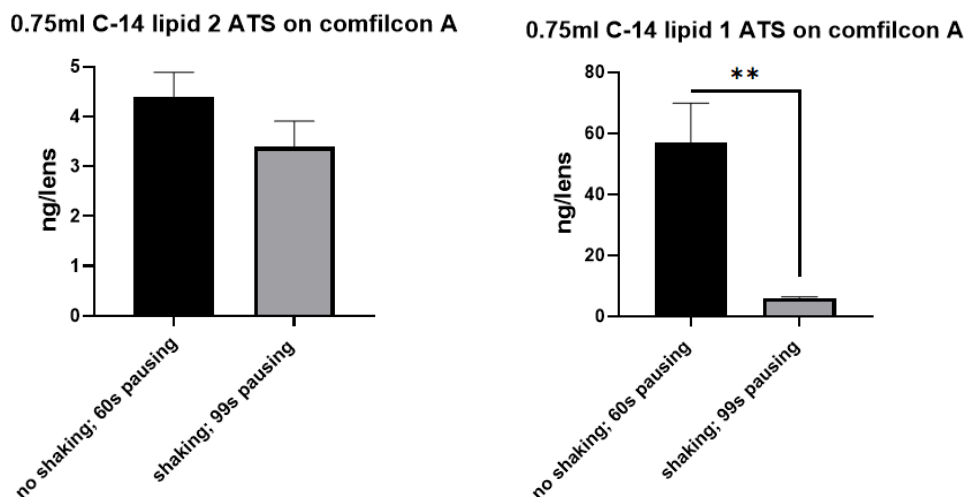


Figure 44. Effect of “shaking” mode and pausing time. One-way ANOVA analysis was applied. P value style: < 0.05(*), < 0.005(**), < 0.0002(***), < 0.0001(****).

Based on the effect of the “shaking” mode and longer air exposure time, we tested the lipid 1 deposition on 4 commercial lenses again and obtained the following trend, which was the same as expected and previously observed from literature (ref): senofilcon A > comfilcon A > lotrafilcon B > omafilcon A (Figure 45).

However, comparing to the lipid deposition result from Lorentz et al., we found that the trend was different for these samples [156]. Lorentz et al. also tested the deposition of an amphiphilic lipid on various commercial lenses in both fully submerged mode and intermittently air-exposed mode. Their result showed that the air exposure could significantly increase the deposition of the amphiphilic lipid onto omafilcon A, balafilcon A, comfilcon A and senofilcon A lenses, among which balafilcon A exhibited the highest lipid deposition, followed by comfilcon A, omafilcon A, senofilcon A and lotrafilcon B. This result again confirmed the effect of air exposure on lipid deposition. In their experiment, the lens was allowed to be submerged in ATS for 2 s and exposed to air for 5 s, while in our test, the air exposure time was set to be 99 s. However, as no significant difference was observed between lotrafilcon B, senofilcon A and omafilcon A lenses in Lorentz et al. paper, the slight difference in our trend and the trend in Lorentz et al. study might fall within the experiment error range. Also, the difference in air exposure time can be a possible reason for different trends we obtained. There were more kinds of salt components in Lorentz et al. ATS, which could contribute to the difference.

lipid 1 deposition (ATS = 0.75ml)

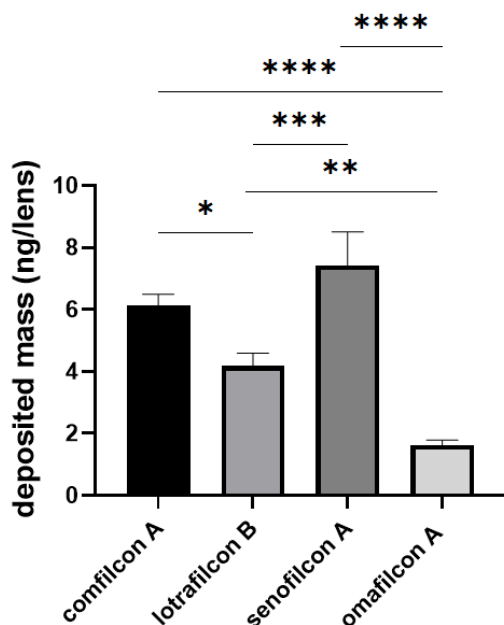


Figure 45. Lipid 1 deposition on 4 commercial lenses. Deposition on omafilcon A was significantly lower than all other three lenses. One-way ANOVA analysis was applied. P value style: < 0.05(*), < 0.005(**), < 0.0002(***), < 0.0001(****).

4.3.7 Adsorption vs absorption of lipids

The adsorption and absorption of lipid 1 and lipid 2 were analyzed on comfilcon A lenses using Zeiss LSM700 confocal microscope. In this section, fluorescently labelled lipids were used, and samples were incubated in lipid solution at 37 °C for 24 hours. The absorption profile was further investigated by using z-stack function of 350 µm thick samples and 50 µm step. The surface of the sample was identified as the lowermost slice. Image processing and mean gray value measurement were then performed with ImageJ software.

Compared with lipid 2, lipid 1 shows less adsorption into the hydrogel sample, which means that lipid 1 tends to adsorb on the hydrogel surface, while lipid 2 tends to soak into the lens itself. Therefore, lipid 1 deposition could be more affected by the surface area, and the surface area can be determined by the surface topography. In the following tests, lipid 1 deposition was performed on all patterned SiHy samples, and lipid 2 deposition was only performed on selected patterns.

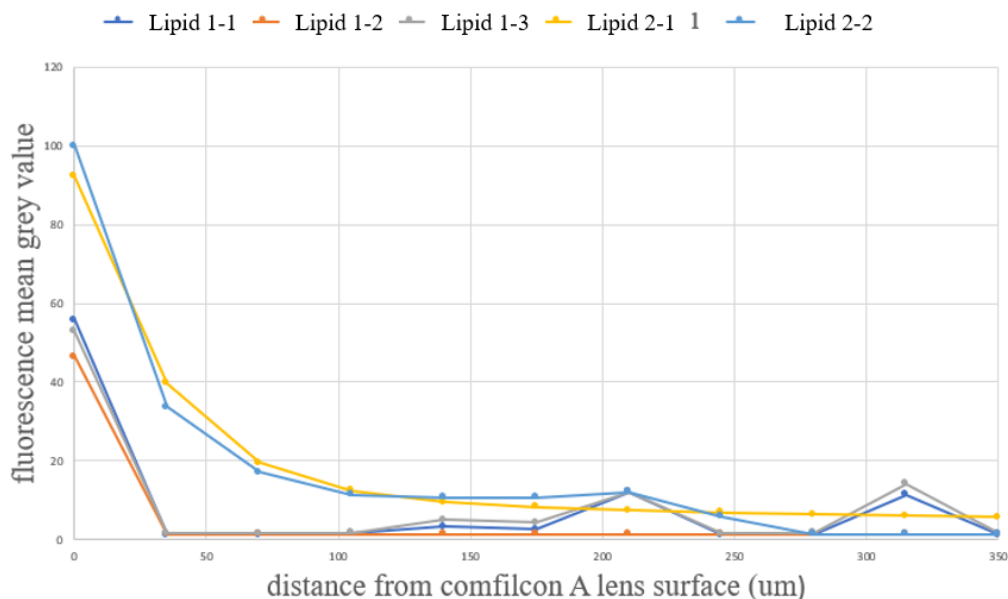


Figure 46. Lipid 2 soaked (absorbed) more into the lens while lipid 1 adsorbed onto the lens surface.

4.3.8 Lipid 1 & lipid 2 deposition on surface patterned SiHy samples

Based on the preliminary test results, all surface patterned SiHy samples were incubated with 0.75 ml ATS solution for 10 h at 37 °C. The “shaking” mode was also applied to remove potential liquid residues on sample surface and the air exposure time was set to be 99 s.

The deposition of each lipid type varied depending on the topography. C-14 lipid 2 was highly absorbed on pattern 10, while C-14 lipid 1 showed a high deposition on pattern 12 and pattern L4. Some patterns show lower lipid deposition than the blank control such as pattern 11, pattern 18 and pattern 21.

When the sample incubation process was complete, we picked up the SiHy samples from the vial caps, and we noticed that some samples fell out from the cap during the process and both surfaces of the sample were exposed to the ATS. In this case, lipid could deposit onto both surfaces during the incubation process. This could also introduce errors to the result, and we have removed those data points. Therefore, pattern 12, 18, 19, 27, 28 and 29 only had n=2 replicas, and all other patterns had n=3 replicas.

**lipid 2 deposition, ATS = 0.75ml
(normalized to blank)**

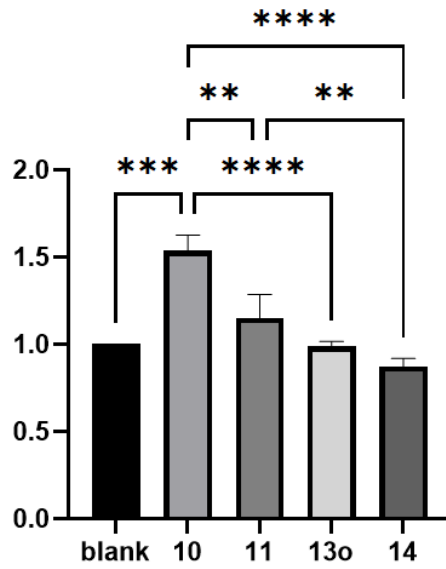


Figure 47. lipid 2 deposition on pattern SiHy samples. One-way ANOVA analysis was applied. P value style: < 0.05(*), < 0.005(**), < 0.0002(***), < 0.0001(****).

**Lipid 1 deposition, ATS = 0.75ml
(normalized to blank)**

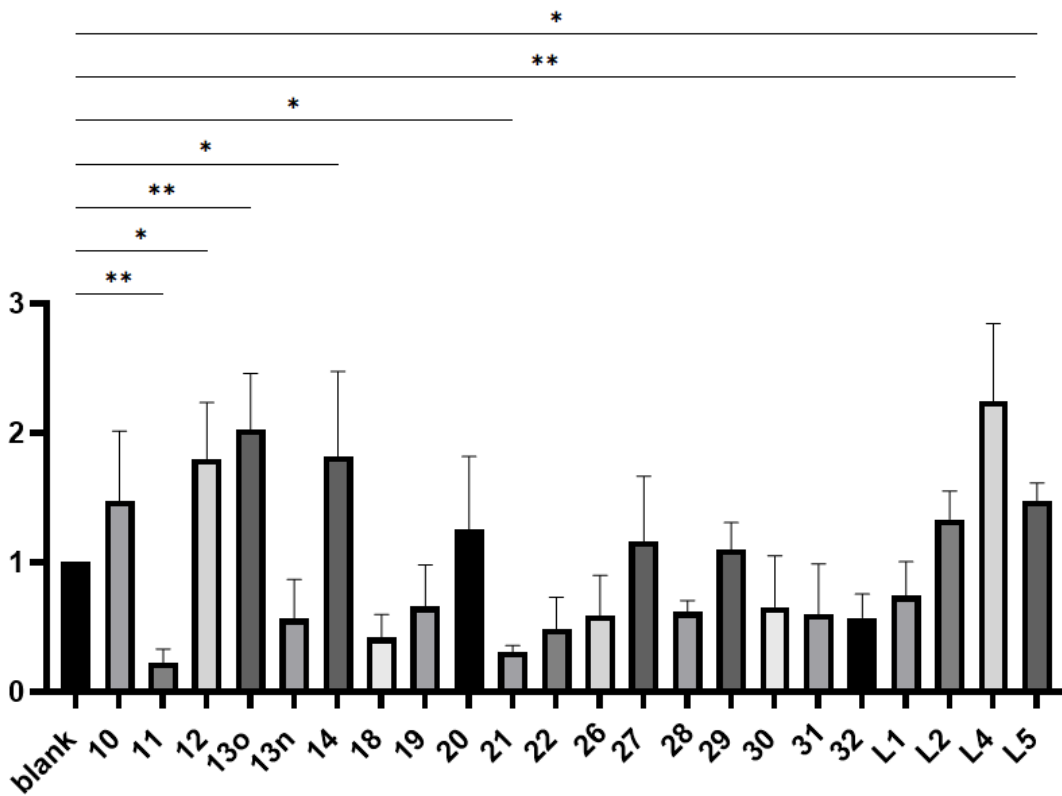


Figure 48. Lipid 1 deposition onto patterned SiHy samples. T test was performed to compare patterned SiHy samples with the blank control, and a $p < 0.05$ was considered significantly different. P value style: < 0.05 (*), < 0.005 (**), < 0.0002 (***), < 0.0001 (****).

4.3.9 Bacteria growth curve

Bacteria 1 are widespread gram-negative bacteria, and their optimal growing temperature is 26 °C. *Bacteria 2* are gram-positive bacteria, and they grow at 26 °C. Generally, *bacteria 1* species show higher adhesion onto contact lenses than *bacteria 2* species because they have higher organism surface hydrophobicity [157].

Using a standard bacterial adhesion test protocol, $\sim 10^8$ CFU/ml PBS culture was used for sample incubation. To guarantee that the cell concentration of PBS culture was the same for different experiments, it is necessary to obtain the growth curve of the bacteria. A single colony was picked from the *bacteria 1* stock plate and allowed to grow in the NB solution, while the *bacteria 2* colony was growing in TSB solution. The OD reading at 600nm wavelength was recorded through the plate reader every 30 min, and the plate counting was performed at the same time. The growth curve of two bacteria is shown below in Figure 49 and 50, respectively. When the OD 600 reading was between 0.18-0.28, the *bacteria 2* cell concentration was in the range of $\sim 10^8$ CFU/ml; When the OD 600 reading was between 0.14-0.24, the *bacteria 1* cell concentration was in the range of $\sim 10^8$ CFU/ml. Therefore, the following experiments started when OD reading reached 0.25 for *bacteria 2* culture and 0.2 for *bacteria 1*.

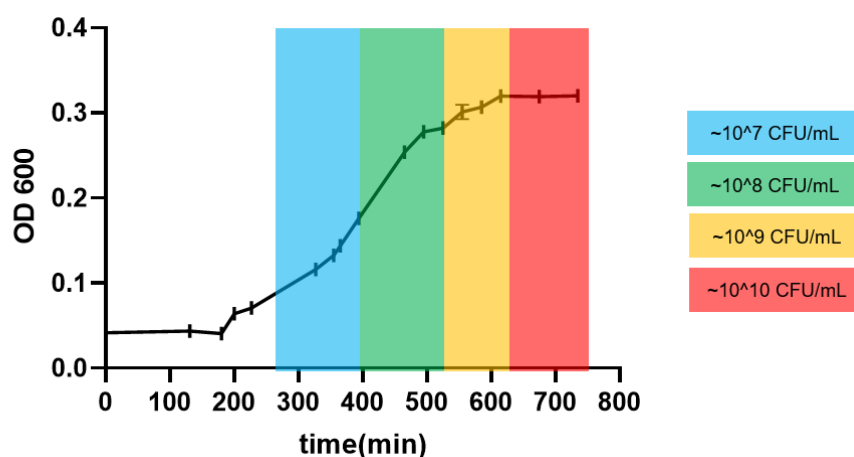


Figure 49. *Bacteria 2* growth curve at 37 °C.

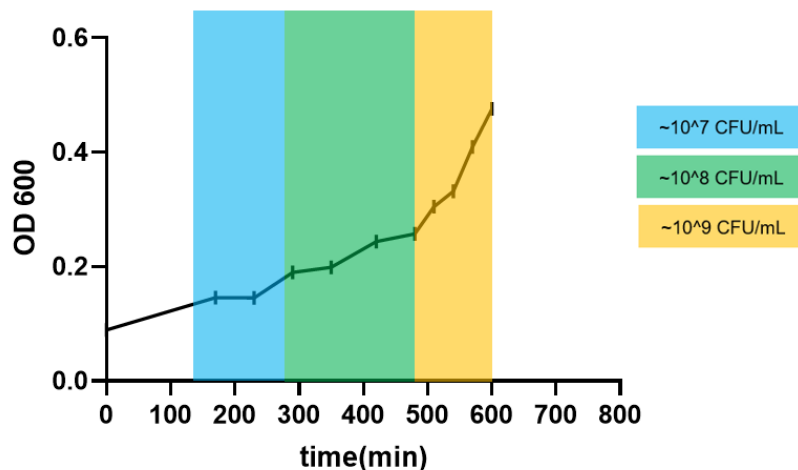


Figure 50. *Bacteria 1* growth curve at 26 °C.

4.3.10 Preliminary *bacteria 2* adhesion test on commercial lenses

A silicone hydrogel material lotrafilcon A (AirOptix Night and Day Aqua) and a conventional HEMA hydrogel material etafilcon A (Acuvue2) were selected to benchmark the primary bacteria adhesion protocol. Due to the higher hydrophobicity of silicone hydrogel lenses compared to HEMA-based lenses, higher numbers of bacteria were expected to adhere onto their surfaces.

These two commercial lenses were soaked in PBS prior to bacteria adhesion in order to reduce potential impact of inhibitory agents in the lens packaging solution. Soaked lenses were then incubated in the bacteria culture for 2 hours and plate counting method was used to evaluate the number of cells adhered onto lens surfaces. As is shown in Figure 51, lotrafilcon A lenses tended to have higher primary adhesion than etafilcon A lenses, which was consistent with the previous research [158].

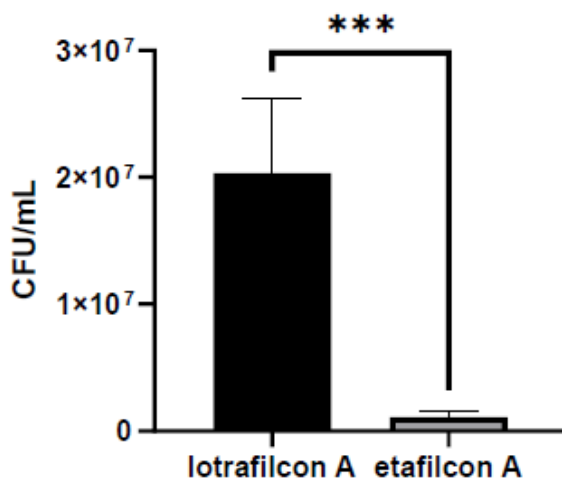


Figure 51. *Bacteria 2* adhered more onto lotrafilcon A lenses than etafilcon A lenses. T test was performed, and a $p < 0.05$ was considered significantly different. P value style: < 0.05 (*), < 0.005 (**), < 0.0002 (***), < 0.0001 (****).

4.3.11 Bacterial adhesion onto surface patterned SiHy samples

Figure 52 illustrates the *bacteria 2* adhesion onto pattern 10, 11, 13o and 14. Pattern 13o exhibited relatively lower adhesion than other patterns, while pattern 11 shows much higher adhesion. Although pattern 11 exhibited higher surface wettability, in the *bacteria 1* adhesion test, it happened again that pattern 11 was one of patterns having high adhesion.

Based on the literature review, surface topography could exhibit antibacterial properties and reduce the microbial adhesion [133, 137]. However, our result showed that the patterns did not decrease the bacteria adhesion and some patterns even increased the adhesion. Therefore, there should be some other factors that changed the properties of SiHy surface and bacteria. The bacterial adhesion onto solid surfaces is a complex process, it can be determined by the bacteria cell structure and bacteria surface hydrophobicity. The interaction between bacteria and material surface is also essential for bacteria adhesion and biofilm formation, and such interaction is highly affected by the material surface properties such as surface roughness, surface charge, surface chemistry or surface stiffness [7, 9]. Typically, adding surface topography onto material surfaces will not affect the surface chemistry. However, various patterning techniques could introduce surface chemistry changes [159, 160], making it a possible reason for higher bacteria adhesion increase.

Whether the bacteria incubation media is nutritionally rich can also affect the adhesion. Bacteria cell viability could be reduced in nutritionally poor media, especially when they were incubated for an extended period of time [161]. In the above studies, some bacteria were incubated in media with different supplementary such as glucose and yeast extract, while some were cultured in saline solution or artificial tears. Even in the same culture media, different bacteria strains could still exhibit different adhesion [162]. Therefore, it was reasonable to see a difference between the literature and our result, and more types of bacteria are worthy of being tested.

bacteria 2 adhesion (normalized to blank)

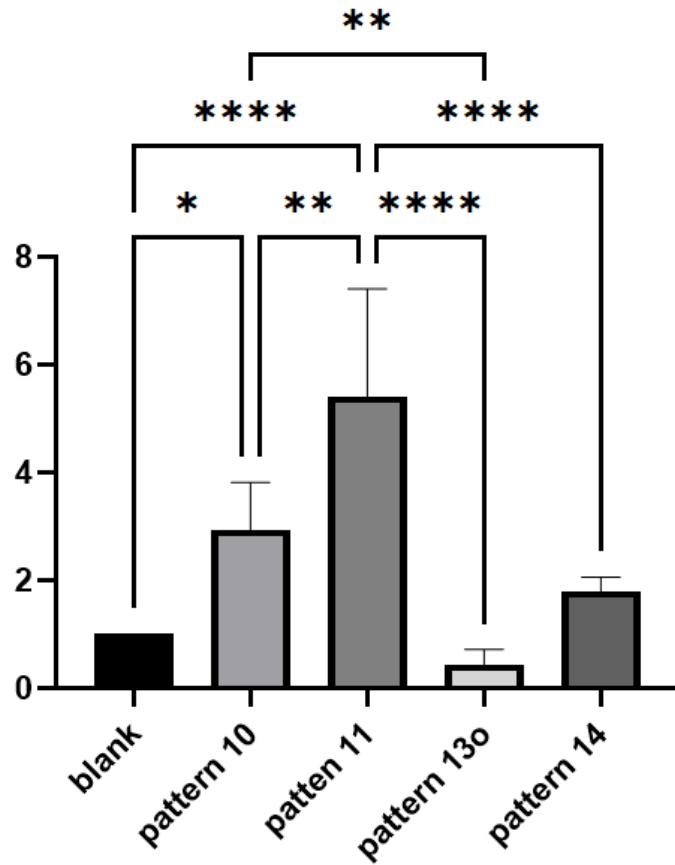


Figure 52. *Bacteria 2* adhesion onto patterned SiHy samples. One-way ANOVA analysis was applied. P value style: < 0.05(*), < 0.005(**), < 0.0002(***), < 0.0001(****).

bacteria 1 adhesion (normalized to blank)

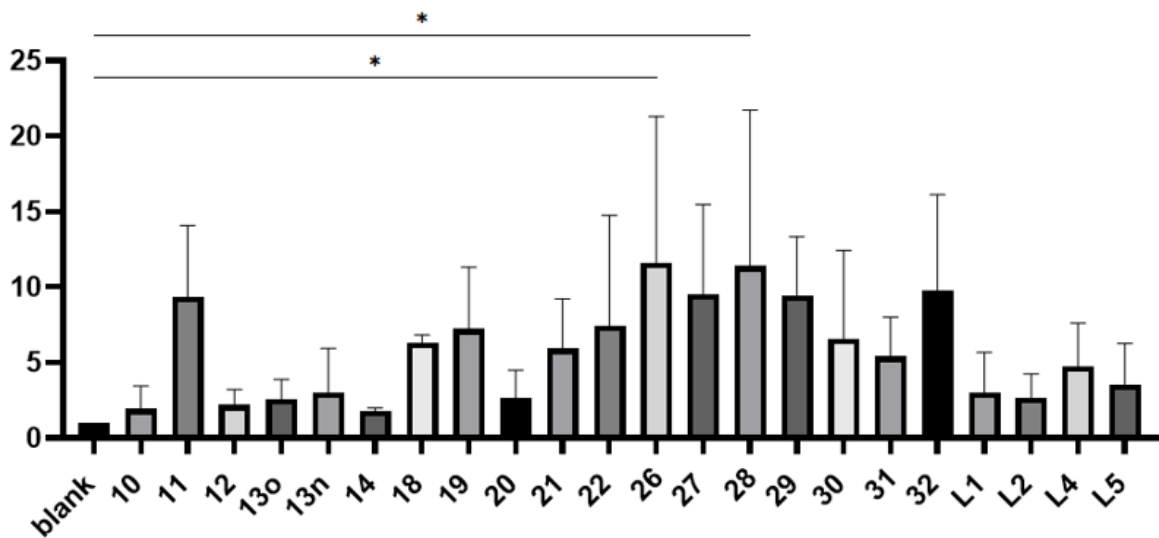


Figure 53. *Bacteria 1* adhesion onto patterned SiHy samples. One-way ANOVA analysis was applied. P value

style: < 0.05(*), < 0.005(**), < 0.0002(***), < 0.0001(****).

4.4 Correlation between surface pattern parameters and surface properties

Principal Component Analysis (PCA) is a multivariate technique that can reduce the dimension of a dataset but still retain as much information as possible. It can also be used to find the correlation between multiple variables. In this project, we have many different variables including the surface topography parameters, contact angle, lipid deposition and microbial adhesion. The lipid deposition may not be directly affected by structure dimensions, but the change in surface energy due to these topographies can possibly alter the lipid deposition. Also, deposits on the hydrogel sample surface can also manipulate the microbial adhesion. Therefore, it would be worthwhile to perform a PCA analysis on all of these variables to figure out how they could be related to or affected by each other.

Figure 54 shows the PCA analysis of all the variables in this project. The loading refers to the correlation between the values of the variable and the calculated values for the component. When the angle between two vectors is approaching 0 or 180°, it means that the two variables are positively or negatively correlated to each other. More perpendicular two vectors are, weaker correlation will exist in between.

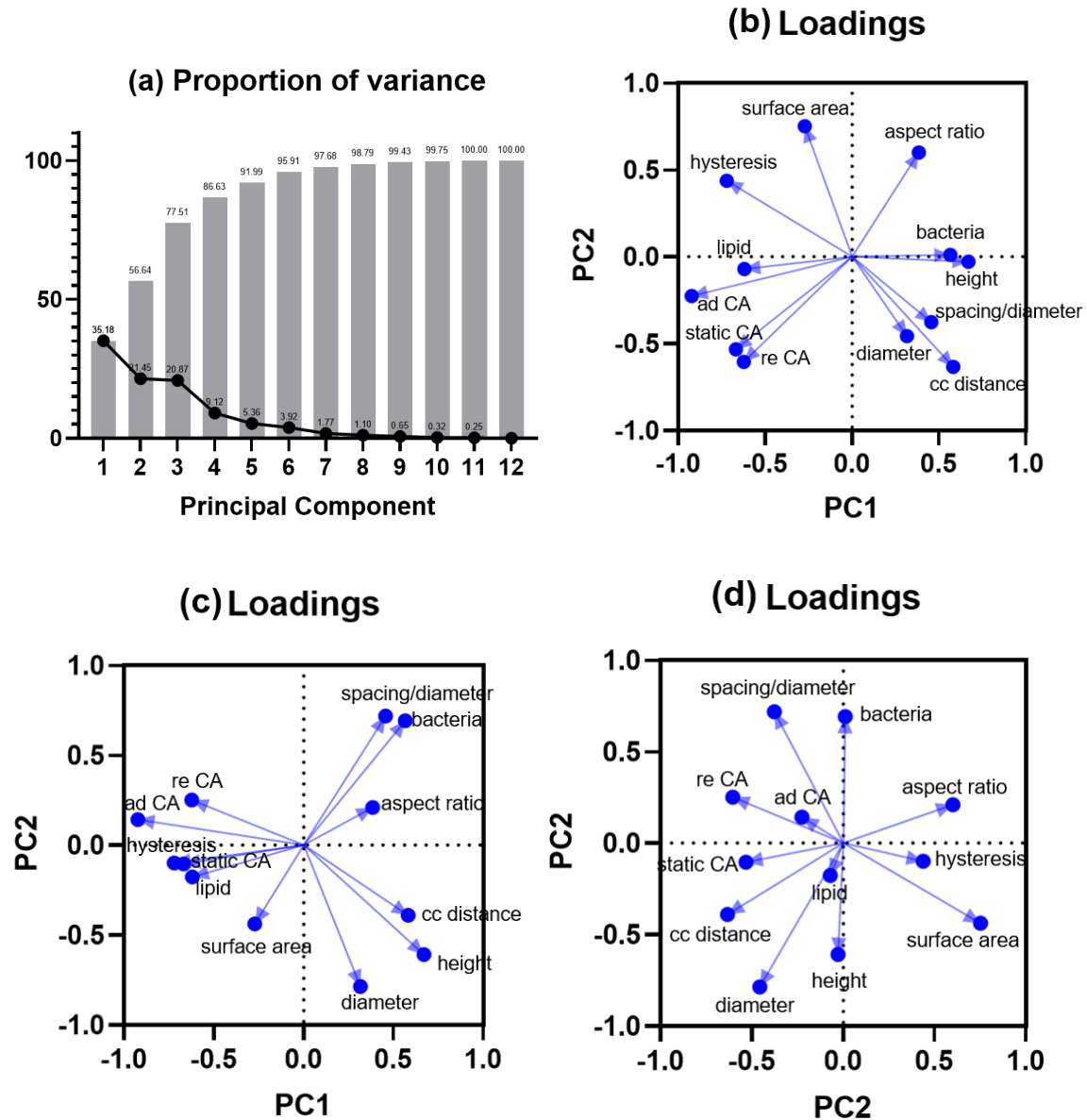


Figure 54. PCA analysis with respect to different variances. (a) proportion of component variances, (b) PC1 vs. PC2, (c) PC1 vs. PC3, (d) PC2 vs. PC3.

As illustrated in Figure 54, both static water contact angle and dynamic contact angle were not correlated with the structure height or diameter. According to the PCA analysis, the lipid 1 deposition had strong correlation with static water contact angle and contact angle hysteresis. When the surface energy was altered by the surface topography, lipid deposition was subsequently affected. Although we found that lipid 1 tended to adsorb onto the hydrogel surface, the theoretical sample surface area was not closely correlated with the lipid deposition. The PCA analysis also showed a weak correlation between bacterial adhesion and structure height in Figure 54(b), however, they were found to be negatively correlated in Figure 54(d). Compared with the height, the bacterial adhesion was more correlated to the ratio of spacing/diameter, showing that the adhesion process could be affected by the interaction between the cell and the structure.

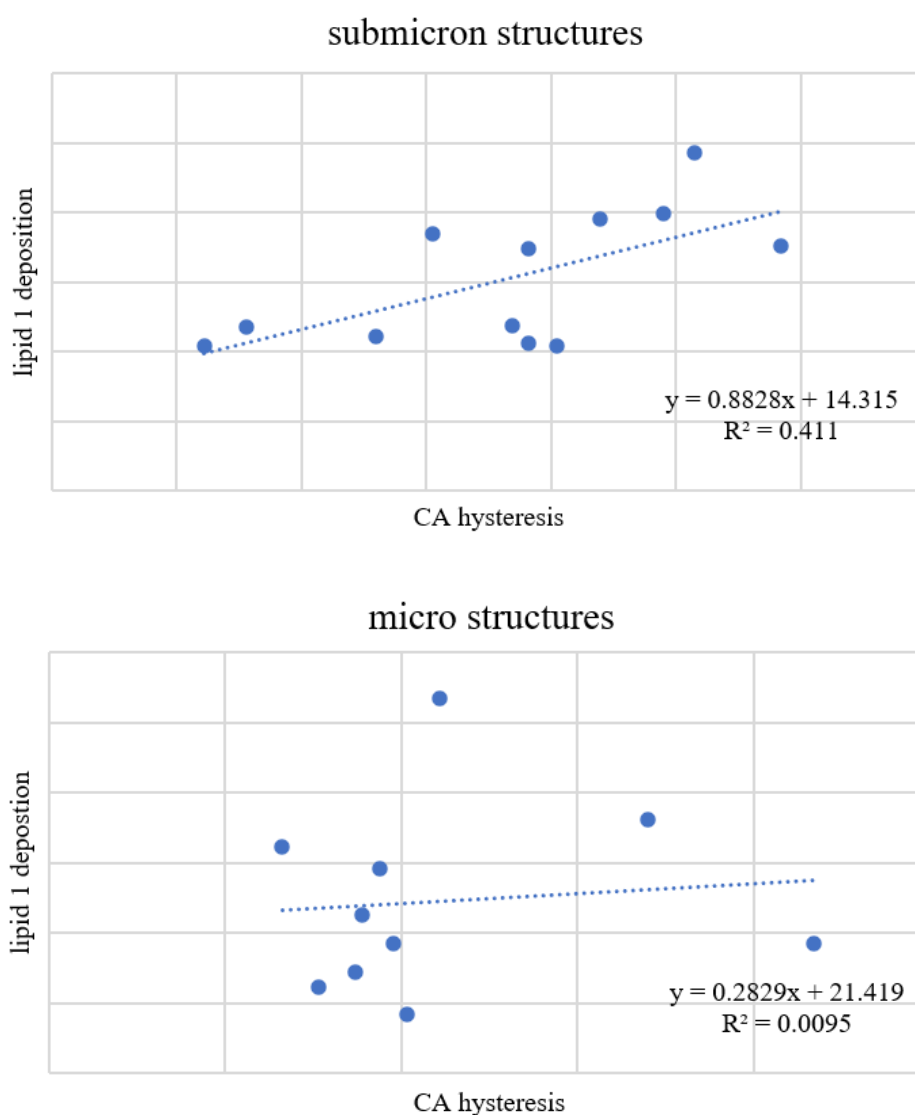


Figure 55. Linear regression of lipid 1 deposition vs. contact angle hysteresis for submicron and micro patterns.

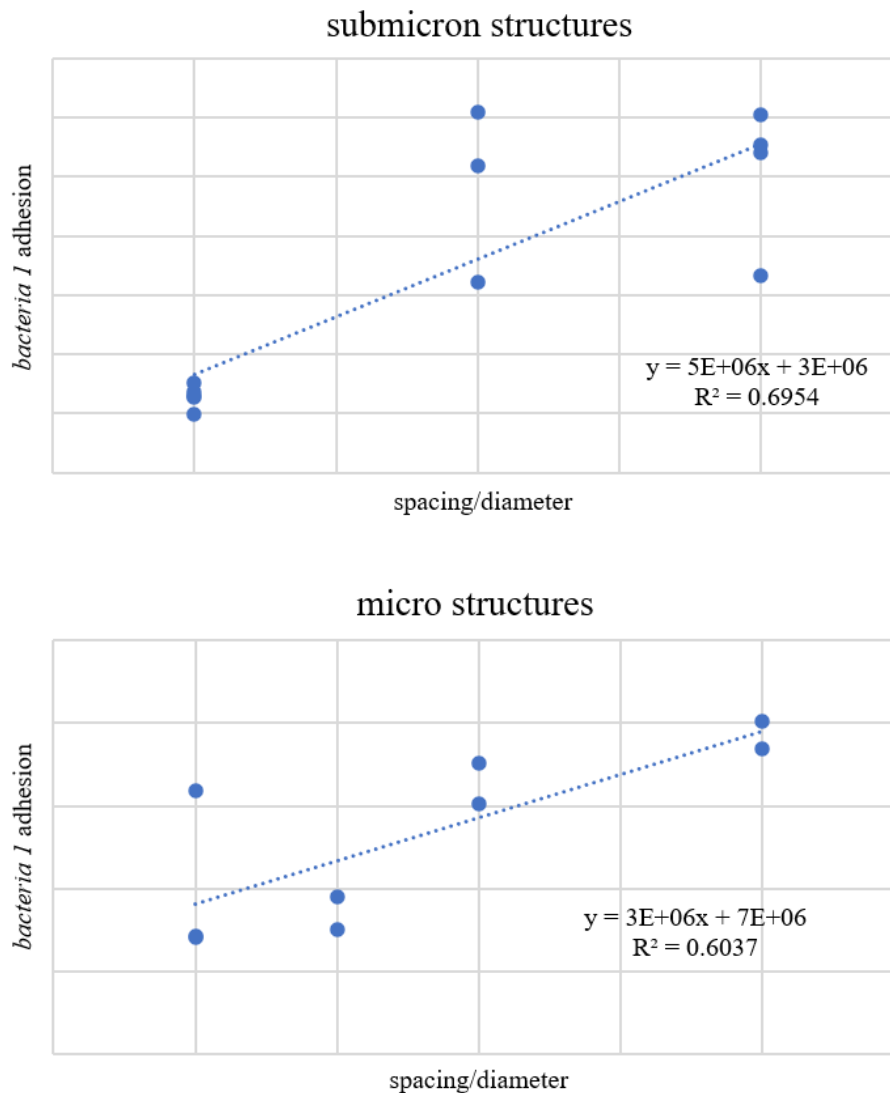


Figure 56. Linear regression of *bacteria I* adhesion vs. spacing/diameter ratio for submicron and micro patterns.

Furthermore, we analyzed the effects of contact angle hysteresis on lipid 1 deposition and the effects of spacing/diameter ratio on *bacteria I* adhesion by means of the linear regression in Excel. Patterns were divided into two groups based on their dimensions as we found that submicron and microstructures could have different effects on SiHy surface properties. The linear regression analysis indicated that lipid 1 deposition was more predictable for submicron structures than microstructures, as evidenced by its relatively higher R^2 value (Figure 55). Also, a positive relationship was found between the *bacteria I* adhesion and the ratio of spacing/diameter for both submicron and microstructures, showing that it could be one of the main determinants for bacteria adhesion (Figure 56).

4.5 Conclusion

This chapter mainly focused on characterizing patterned SiHy surface properties, including surface wettability, lipid deposition, and microbial adhesion, because an ideal contact lens should exhibit high wettability, low tear film lipid deposition, and low microbial contamination. The captive bubble method was used to measure the static and dynamic contact angle of SiHy samples because all samples could be kept fully hydrated during the

process, and the quality of surface structures could be maintained well. Then, we tested the lipid deposition onto SiHy samples with two different radioactive lipids, and the quantitative analysis was performed using a scintillation beta counter. From the result, pattern 11 showed outstanding performance in both the wettability test and lipid deposition test; however, it also had a higher bacterial adhesion. The adhesion of two different types of bacteria was evaluated in this study. Both could cause contact lens-related microbial keratitis. We observed no significant decrease in bacterial adhesion on these patterned SiHy samples, which conflicted with the literature that surface topographies could help reduce the microbial adhesion. This could be due to the surface chemistry changes from the surface patterning technique. The bacteria suspension media and bacteria strains could also influence the bacteria adhesion and can be further investigated. We also performed the principal component analysis to evaluate how these different variables could be correlated, and we found that the lipid deposition was correlated to the contact angle hysteresis. At the same time, the bacterial adhesion was correlated to the ratio of spacing/diameter. Therefore, the surface topography could alter the hydrogel surface properties and improve contact lens performance in some aspects, but further study is still necessary to figure out the mechanism.

Chapter 5 Summary and Future Work

5.1 Si wafer fabrication and PP molds development

In this study, the Si wafers were ordered from Eulitha or fabricated at QNC through UV and e-beam lithography. Some Si molds were over-etched so that larger heights were obtained. As some Si molds were not sufficiently etched, and the final heights were slightly lower than their expected values. This problem could subsequently lead to the SiHy pattern fidelity from the theoretical values and could be solved by better controlling the etching rate/time.

To increase the quality of PP molds, three different PP samples were evaluated. The USP PP was a homopolymer, and the GoodFellow PP was a copolymer. The information of PP pellets provided by our collaborator was not given, but by comparing their FTIR and DSC data, we found that it was more like the GoodFellow PP. All three different PP were tested for heat embossing, and the PP pellets were found to be the best as they created fewer defects on the surface. The defects on these PP samples could come from the plasticizers or antioxidants inside or be created by the reaction between two monomers. To obtain a better understanding, we could also compare the FTIR spectra of our PP samples with the spectra of pure PP or commonly used plasticizers.

The surface topography characterization of SiHy samples was also challenging, especially for those submicron structures. Cross-sectional SEM can also be used to confirm the pattern diameters and whether those structures had vertical walls.

5.2 Oxygen permeability of patterned SiHy samples

SiHy could support significantly higher oxygen transport than conventional soft contact lenses due to the silicone component. Some studies showed that the surface topography could affect the oxygen distribution and penetration throughout the surface [163, 164]. Therefore, it would be meaningful to check the oxygen permeability of patterned SiHy samples to ensure that the amount of oxygen transported will not be reduced by the surface structures.

5.3 SiHy surface properties characterization

Surface wettability, lipid deposition, and bacterial adhesion were three properties that were characterized for patterned SiHy samples in this study. When measuring contact angles, samples were all stabilized under the DI water. However, actual contact lenses are in direct contact with tear fluids when worn. Therefore, it is worthwhile to measure the contact angles by placing the samples in other fluids, for example, artificial tear solution or saline solution. It could give us more information about the sample surface energy change.

During the lipid deposition test, we noticed that the sample could fall out from the cap if they were not mounted well, which could introduce errors into the result and should be avoided. Also, the bacteria adhesion result we got was different from the literature that no significant reduction was observed on patterned SiHy samples. This could be because the bacteria type and the bacterial suspension media we used were different. Due to the limitation of time and resources, the deposition of lipid 2 and the adhesion of bacteria 2 were only tested on the part of the samples. To obtain a better understanding, we can try to incubate the samples in different cultures, such as nutritionally rich media or artificial tears. In addition, it is worthwhile to evaluate the microbial adhesion using different bacteria strains because the bacteria cell hydrophobicity and cell structure can also affect the interaction between bacteria and the material surface.

Also, all patterns investigated in this study were pillars, opposite well patterns with the same diameter, center-to-center distance and depth can be tested to help confirm how the surface area and surface roughness would affect the above surface properties.

5.4 Summary

This project mainly worked on evaluating the effect of surface topographies on SiHy surface properties. We tested three different PP samples for their quality and finally selected the one from the collaborator for PP molds fabrication because it exhibited fewer surface defects. Also, we found that several factors can influence the PP mold fabrication including temperature, pressure, and cooling time. Usually, we should set the temperature to be slightly higher than the theoretical melting temperature of PP so that the polymer could be melted and embossed. The pressure was also significant for successful embossing as it should be high enough to push the melted polymer into the structures of the negative mold.

After characterizing the surface wettability, lipid deposition and microbial adhesion properties of these patterned SiHy samples, we noticed that pattern 11 exhibited higher wettability and lower lipid deposition; however, this pattern also showed higher bacterial adhesion, which was undesirable. To further investigate the correlation between these variables, we performed PCA analysis, and the result showed that the lipid deposition was more correlated to the static water contact angle and contact angle hysteresis, while the bacteria adhesion was more correlated to the spacing/diameter ratio. Although the surface area was negatively correlated to the microbial adhesion, there was only weak correlation. The result showed that the surface topography could alter the surface properties of SiHy samples, but how these properties could affect each other was still not clear. For example, how lipid deposition could influence the microbial adhesion should be investigated by keeping all other parameters the same, which still needs further studies.

References

1. Yang, W.-H., V.F. Smolen, and N.A. Peppas, *Oxygen permeability coefficients of polymers for hard and soft contact lens applications*. Journal of Membrane Science, 1981. **9**(1-2): p. 53-67.
2. Mann, A. and B. Tighe, *Contact lens interactions with the tear film*. Experimental eye research, 2013. **117**: p. 88-98.
3. Tiffany, J.M., *Composition and biophysical properties of the tear film: knowledge and uncertainty*. Lacrimal Gland, Tear Film, and Dry Eye Syndromes, 1994: p. 231-238.
4. Dilly, P., *Structure and function of the tear film*. Lacrimal gland, tear film, and dry eye syndromes, 1994: p. 239-247.
5. Ormerod, L.D. and R.E. Smith, *Contact lens-associated microbial keratitis*. Archives of ophthalmology, 1986. **104**(1): p. 79-83.
6. Stapleton, F., et al., *The incidence of contact lens-related microbial keratitis in Australia*. Ophthalmology, 2008. **115**(10): p. 1655-1662.
7. Dutta, D., N. Cole, and M. Willcox, *Factors influencing bacterial adhesion to contact lenses*. Molecular vision, 2012. **18**: p. 14.
8. Dunne Jr, W.M., *Bacterial adhesion: seen any good biofilms lately?* Clinical microbiology reviews, 2002. **15**(2): p. 155-166.
9. Willcox, M.D., *Microbial adhesion to silicone hydrogel lenses: a review*. Eye & contact lens, 2013. **39**(1): p. 61-66.
10. THOMPSON, R., *Lysozyme and the antibacterial properties of tears*. Archives of Ophthalmology, 1941. **25**(3): p. 491-509.
11. McDermott, A.M., *Antimicrobial compounds in tears*. Experimental eye research, 2013. **117**: p. 53-61.
12. Efron, N., et al., *Oxygen permeability and water content of silicone hydrogel contact lens materials*. Optometry and Vision Science, 2007. **84**(4): p. E328-E337.
13. Sunny, M. and C.P. Sharma, *Surface modification of corneal contact lens with phosphoryl choline by glow discharge*. Biomaterials, Artificial Cells and Immobilization Biotechnology, 1991. **19**(3): p. 599-612.
14. Szczołka-Flynn, L.B., et al., *Increased resistance of contact lens related bacterial biofilms to antimicrobial activity of soft contact lens care solutions*. Cornea, 2009. **28**(8): p. 918.
15. Muntz, A., et al., *Tear exchange and contact lenses: A review*. Journal of optometry, 2015. **8**(1): p. 2-11.
16. Cavanagh, H.D., et al., *Forty Years in Search of the Perfect Contact Lens*. Cornea, 2010. **29**(10): p. 1075.
17. Korb, D.R., *Tear film—contact lens interactions*. Lacrimal Gland, Tear Film, and Dry Eye Syndromes, 1994: p. 403-410.
18. Alam, F., et al., *Prospects for Additive Manufacturing in Contact Lens Devices*. Advanced Engineering Materials, 2021. **23**(1): p. 2000941.
19. Stocker, E. and J.P. Schoessler, *Corneal endothelial polymegathism induced by PMMA contact lens wear*. Investigative ophthalmology & visual science, 1985. **26**(6): p. 857-863.
20. Athreya, P.K. and G.K. Bhardwaj, *Contact Lens Materials and Modalities*. Trend in Opftthalmology, 2018. **1**(1): p. 1-5.
21. Refojo, M.F., F.J. Holly, and F.-L. Leong, *Permeability of dissolved oxygen through contact lenses I. Cellulose acetate butyrate*. Eye & Contact Lens, 1977. **3**(4): p. 27-33.
22. Carlson, K., et al., *Effect of silicone elastomer contact lens wear on endothelial cell morphology in aphakic eyes*. Cornea, 1990. **9**(1): p. 45-47.
23. Chen, Y., et al., *Microengineered poly (HEMA) hydrogels for wearable contact lens biosensing*. Lab on

- a Chip, 2020. **20**(22): p. 4205-4214.
24. Ahmed, E.M., *Hydrogel: Preparation, characterization, and applications: A review*. J Adv Res, 2015. **6**(2): p. 105-21.
 25. Kopeček, J., *Swell gels*. Nature, 2002. **417**(6887): p. 389-391.
 26. LeVier, R.R., et al., *What is silicone?* Plastic and reconstructive surgery, 1993. **92**(1): p. 12-167.
 27. Filipecki, J., A. Kocela, and W. Korzekwa, *Study of free volumes of polymer hydrogel and silicone-hydrogel contact lenses by means of the positron annihilation lifetime spectroscopy method*. Polymers in Medicine, 2014. **44**(4): p. 255-260.
 28. Lee, M.-J. and A. Sung, *Preparation and physical properties of silicone hydrogel ophthalmic lens containing hydrophilic monomer*. Journal of the Korean Chemical Society, 2016. **60**(4): p. 261-266.
 29. Zhang, H. and A. Cloud, *The permeability characteristics of silicone rubber*. Global Advances in Materials and Process Engineering, 2006: p. 72-75.
 30. Wang, J.-j. and X.-s. Li, *Improved oxygen permeability and mechanical strength of silicone hydrogels with interpenetrating network structure*. Chinese Journal of Polymer Science, 2010. **28**(6): p. 849-857.
 31. Bennett, E.S. and V.A. Henry, *Clinical manual of contact lenses*. 2019: Lippincott Williams & Wilkins.
 32. Giraldez, M.J., et al., *Contact lens hydrophobicity and roughness effects on bacterial adhesion*. Optometry and Vision Science, 2010. **87**(6): p. E426-E431.
 33. Boone, A., et al., *Ex vivo protein deposition on bi-weekly silicone hydrogel contact lenses*. Optometry and Vision Science, 2009. **86**(11): p. 1241-1249.
 34. Cheng, L., S.J. Muller, and C.J. Radke, *Wettability of silicone-hydrogel contact lenses in the presence of tear-film components*. Current eye research, 2004. **28**(2): p. 93-108.
 35. Suwala, M., et al., *Quantity and conformation of lysozyme deposited on conventional and silicone hydrogel contact lens materials using an in vitro model*. Eye & contact lens, 2007. **33**(3): p. 138-143.
 36. Lam, C.N., et al., *Study of the advancing and receding contact angles: liquid sorption as a cause of contact angle hysteresis*. Advances in colloid and interface science, 2002. **96**(1-3): p. 169-191.
 37. Kyzas, G.Z. and A.C. Mitropoulos, *Advanced Low-cost Separation Techniques in Interface Science*. 2019: Academic Press.
 38. Read, M.L., et al., *Dynamic contact angle analysis of silicone hydrogel contact lenses*. Journal of biomaterials applications, 2011. **26**(1): p. 85-99.
 39. Walther, H., et al., *Differential deposition of fluorescently tagged cholesterol on commercial contact lenses using a novel in vitro eye model*. Translational vision science & technology, 2018. **7**(2): p. 18-18.
 40. Lorentz, H., et al., *Contact lens physical properties and lipid deposition in a novel characterized artificial tear solution*. Molecular vision, 2011. **17**: p. 3392.
 41. Turano, A. and F. Pirali, *Quantification methods in microbiology*, in *Laboratory diagnosis of infectious diseases*. 1988, Springer. p. 8-13.
 42. Zhao, Q., et al., *Factors affecting improvement of engineering properties of MICP-treated soil catalyzed by bacteria and urease*. Journal of Materials in Civil Engineering, 2014. **26**(12): p. 04014094.
 43. Daley, R.J. and J.E. Hobbie, *Direct counts of aquatic bacteria by a modified epifluorescence technique I*. Limnology and oceanography, 1975. **20**(5): p. 875-882.
 44. Norland, S., *Section Biomass The Relationship Between Biomass and Volume of Bacteria*, in *Handbook of methods in aquatic microbial ecology*. 2018, CRC press. p. 303-307.
 45. LeChevallier, M.W., R.J. Seidler, and T. Evans, *Enumeration and characterization of standard plate count bacteria in chlorinated and raw water supplies*. Applied and Environmental Microbiology, 1980. **40**(5): p. 922-930.

46. Kulkarni, S.A., S.B. Ogale, and K.P. Vijayamohan, *Tuning the hydrophobic properties of silica particles by surface silanization using mixed self-assembled monolayers*. Journal of Colloid and Interface Science, 2008. **318**(2): p. 372-379.
47. Zhang, J.Z., J.C. Chen, and E.D. Kirby, *Surface roughness optimization in an end-milling operation using the Taguchi design method*. Journal of materials processing technology, 2007. **184**(1-3): p. 233-239.
48. Bagherifard, S., et al., *Effect of severe shot peening on microstructure and fatigue strength of cast iron*. International Journal of Fatigue, 2014. **65**: p. 64-70.
49. Chang-Yen, D.A., R.K. Eich, and B.K. Gale, *A monolithic PDMS waveguide system fabricated using soft-lithography techniques*. Journal of lightwave technology, 2005. **23**(6): p. 2088.
50. Lei, Y., et al., *Surface patterning using templates: concept, properties and device applications*. Chemical Society Reviews, 2011. **40**(3): p. 1247-1258.
51. Bao, L.-R., et al., *Nanoimprinting over topography and multilayer three-dimensional printing*. Journal of Vacuum Science & Technology B: Microelectronics and Nanometer Structures Processing, Measurement, and Phenomena, 2002. **20**(6): p. 2881-2886.
52. Müller-Meskamp, L., et al., *Efficiency enhancement of organic solar cells by fabricating periodic surface textures using direct laser interference patterning*. Advanced Materials, 2012. **24**(7): p. 906-910.
53. Cutiungco, M.F., et al., *Planar and tubular patterning of micro and nano-topographies on poly (vinyl alcohol) hydrogel for improved endothelial cell responses*. Biomaterials, 2016. **84**: p. 184-195.
54. Turunen, S., et al., *Chemical and topographical patterning of hydrogels for neural cell guidance in vitro*. Journal of Tissue Engineering and Regenerative Medicine, 2013. **7**(4): p. 253-270.
55. Pfister, P.M., et al., *Surface-textured PEG-based hydrogels with adjustable elasticity: Synthesis and characterization*. Biomaterials, 2007. **28**(4): p. 567-575.
56. Yeh, J., et al., *Micromolding of shape-controlled, harvestable cell-laden hydrogels*. Biomaterials, 2006. **27**(31): p. 5391-5398.
57. Tang, M.D., A.P. Golden, and J. Tien, *Molding of three-dimensional microstructures of gels*. Journal of the American Chemical Society, 2003. **125**(43): p. 12988-12989.
58. Kobel, S., et al., *Micropatterning of hydrogels by soft embossing*. Langmuir, 2009. **25**(15): p. 8774-8779.
59. Di Benedetto, F., et al., *Patterning polyacrylamide hydrogels by soft lithography*. Nanotechnology, 2005. **16**(5): p. S165.
60. Jonelle, Z.Y., et al., *Biomimetic scaffolds with three-dimensional undulated microtopographies*. Biomaterials, 2017. **128**: p. 109-120.
61. Hahn, M.S., et al., *Photolithographic patterning of polyethylene glycol hydrogels*. Biomaterials, 2006. **27**(12): p. 2519-2524.
62. Revzin, A., et al., *Fabrication of poly (ethylene glycol) hydrogel microstructures using photolithography*. Langmuir, 2001. **17**(18): p. 5440-5447.
63. Guo, L.J., *Nanoimprint lithography: methods and material requirements*. Advanced materials, 2007. **19**(4): p. 495-513.
64. Francone, A., et al., *Integrated 3D hydrogel waveguide out-coupler by step-and-repeat thermal nanoimprint lithography: A promising sensor device for water and pH*. Sensors, 2018. **18**(10): p. 3240.
65. Tan, L., et al., *Imprinting of polymer at low temperature and pressure*. Journal of Vacuum Science & Technology B: Microelectronics and Nanometer Structures Processing, Measurement, and Phenomena, 2004. **22**(5): p. 2486-2492.
66. Li, J., et al., *3D printing of hydrogels: Rational design strategies and emerging biomedical applications*. Materials Science and Engineering: R: Reports, 2020. **140**: p. 100543.

67. Han, D., et al., *Micro 3D printing of a temperature-responsive hydrogel using projection micro-stereolithography*. Scientific reports, 2018. **8**(1): p. 1-10.
68. Wang, J., et al., *Hydrogel 3D printing with the capacitor edge effect*. Science advances, 2019. **5**(3): p. eaau8769.
69. Chen, T., et al., *Combining 3D printing with electrospinning for rapid response and enhanced designability of hydrogel actuators*. Advanced Functional Materials, 2018. **28**(19): p. 1800514.
70. Wade, R.J., et al., *Nanofibrous hydrogels with spatially patterned biochemical signals to control cell behavior*. Advanced Materials, 2015. **27**(8): p. 1356-1362.
71. Xu, F., H. Sheardown, and T. Hoare, *Reactive electrospinning of degradable poly (oligoethylene glycol methacrylate)-based nanofibrous hydrogel networks*. Chemical Communications, 2016. **52**(7): p. 1451-1454.
72. Huang, N., C.W. Li, and B.P. Chan, *Multiphoton 3D microprinting of protein micropatterns with spatially controlled heterogeneity—a platform for single cell matrix niche studies*. Advanced Biosystems, 2018. **2**(8): p. 1800053.
73. Tong, M.H., et al., *Multiphoton photochemical crosslinking-based fabrication of protein micropatterns with controllable mechanical properties for single cell traction force measurements*. Scientific reports, 2016. **6**(1): p. 1-12.
74. Wosnick, J.H. and M.S. Shoichet, *Three-dimensional chemical patterning of transparent hydrogels*. Chemistry of Materials, 2008. **20**(1): p. 55-60.
75. Ali, M. and J.B. Shear, *Real time remodeling of cellular morphology using optical imprinting of cell-culture substrates*. Biomedical Physics & Engineering Express, 2019. **5**(3): p. 035029.
76. Bat, E., et al., *Morphing Hydrogel Patterns by Thermo-Reversible Fluorescence Switching*. Macromolecular rapid communications, 2014. **35**(14): p. 1260-1265.
77. Schmidt, T., J.I. Mönch, and K.F. Arndt, *Temperature-Sensitive Hydrogel Pattern by Electron-Beam Lithography*. Macromolecular Materials and Engineering, 2006. **291**(7): p. 755-761.
78. González-Henríquez, C.M., et al., *Design and fabrication of biocompatible wrinkled hydrogel films with selective antibiofouling properties*. Materials Science and Engineering: C, 2019. **97**: p. 803-812.
79. González-Henríquez, C.M., et al., *Microwrinkled pH-sensitive hydrogel films and their role on the cell adhesion/proliferation*. Materials Science and Engineering: C, 2019. **103**: p. 109872.
80. Arias, S.L., et al., *Ion-Induced Nanopatterning of Bacterial Cellulose Hydrogels for Biosensing and Anti-Biofouling Interfaces*. ACS Applied Nano Materials, 2020. **3**(7): p. 6719-6728.
81. Guvendiren, M., S. Yang, and J.A. Burdick, *Swelling-induced surface patterns in hydrogels with gradient crosslinking density*. Advanced Functional Materials, 2009. **19**(19): p. 3038-3045.
82. Guvendiren, M., J.A. Burdick, and S. Yang, *Kinetic study of swelling-induced surface pattern formation and ordering in hydrogel films with depth-wise crosslinking gradient*. Soft Matter, 2010. **6**(9): p. 2044-2049.
83. Sun, J., et al., *Technique of surface modification of a cell-adhesion-resistant hydrogel by a cell-adhesion-available inorganic microarray*. Biomacromolecules, 2008. **9**(10): p. 2569-2572.
84. Peng, X., et al., *Surface patterning of hydrogels for programmable and complex shape deformations by ion inkjet printing*. Advanced Functional Materials, 2017. **27**(33): p. 1701962.
85. Lv, S., et al., *Micro/nanofabrication of brittle hydrogels using 3D printed soft ultrafine fiber molds for damage-free demolding*. Biofabrication, 2020. **12**(2): p. 025015.
86. Hansson, P.M., et al., *Influence of surface topography on the interactions between nanostructured hydrophobic surfaces*. Langmuir, 2012. **28**(21): p. 8026-8034.

87. Wallqvist, V., et al., *Influence of surface topography on adhesive and long-range capillary forces between hydrophobic surfaces in water*. Langmuir, 2009. **25**(16): p. 9197-9207.
88. Heydari, G., et al., *Hydrophobic surfaces: topography effects on wetting by supercooled water and freezing delay*. The Journal of Physical Chemistry C, 2013. **117**(42): p. 21752-21762.
89. Xin, B. and J. Hao, *Reversibly switchable wettability*. Chemical Society Reviews, 2010. **39**(2): p. 769-782.
90. Piao, C., J.E. Winandy, and T.F. Shupe, *From hydrophilicity to hydrophobicity: A critical review: Part I. Wettability and surface behavior*. Wood and Fiber Science, 2010. **42**(4): p. 490-510.
91. Santander-Borrego, M., et al., *Hydrogels with lotus leaf topography: investigating surface properties and cell adhesion*. Langmuir, 2017. **33**(2): p. 485-493.
92. Choi, W., et al., *A modified Cassie–Baxter relationship to explain contact angle hysteresis and anisotropy on non-wetting textured surfaces*. Journal of colloid and interface science, 2009. **339**(1): p. 208-216.
93. Zhang, P., et al., *Superwetting surfaces under different media: Effects of surface topography on wettability*. Small, 2015. **11**(16): p. 1939-1946.
94. Dai, Z., et al., *Wetting control through topography and surface hydrophilic/hydrophobic property changes by coarse grained simulation*. Molecular Simulation, 2017. **43**(13-16): p. 1202-1208.
95. Larrañeta, E., et al., *Hydrogels for hydrophobic drug delivery. Classification, synthesis and applications*. Journal of functional biomaterials, 2018. **9**(1): p. 13.
96. McKenzie, M., et al., *Hydrogel-based drug delivery systems for poorly water-soluble drugs*. Molecules, 2015. **20**(11): p. 20397-20408.
97. Ayala, R., et al., *Engineering the cell–material interface for controlling stem cell adhesion, migration, and differentiation*. Biomaterials, 2011. **32**(15): p. 3700-3711.
98. Wang, L., et al., *Smart thin hydrogel coatings harnessing hydrophobicity and topography to capture and release cancer cells*. Small, 2016. **12**(34): p. 4697-4701.
99. Matsumura, T., et al., *Micro machining for control of wettability with surface topography*. Journal of Materials Processing Technology, 2012. **212**(12): p. 2669-2677.
100. Mock, U., et al., *Towards ultrahydrophobic surfaces: a biomimetic approach*. Journal of Physics: Condensed Matter, 2005. **17**(9): p. S639.
101. Luensmann, D. and L. Jones, *Protein deposition on contact lenses: the past, the present, and the future*. Contact Lens and Anterior Eye, 2012. **35**(2): p. 53-64.
102. Scopelliti, P.E., et al., *The effect of surface nanometre-scale morphology on protein adsorption*. PloS one, 2010. **5**(7): p. e11862.
103. Mitra, S.K., D.A. Hanson, and D.D. Schlaepfer, *Focal adhesion kinase: in command and control of cell motility*. Nature reviews Molecular cell biology, 2005. **6**(1): p. 56-68.
104. Young, B., W. Pitt, and S. Cooper, *Protein adsorption on polymeric biomaterials I. Adsorption isotherms*. Journal of colloid and interface science, 1988. **124**(1): p. 28-43.
105. Jones, L., et al., *Lysozyme and lipid deposition on silicone hydrogel contact lens materials*. Eye & contact lens, 2003. **29**(1): p. S75-S79.
106. Schulte, V.A., et al., *Surface topography induces fibroblast adhesion on intrinsically nonadhesive poly (ethylene glycol) substrates*. Biomacromolecules, 2009. **10**(10): p. 2795-2801.
107. Schulte, V.A., et al., *Topography-Induced Cell Adhesion to Acr-sP (EO-stat-PO) Hydrogels: The Role of Protein Adsorption*. Macromolecular bioscience, 2011. **11**(10): p. 1378-1386.
108. Cutiongco, M.F., et al., *In vitro and ex vivo hemocompatibility of off-the-shelf modified poly (vinyl alcohol) vascular grafts*. Acta biomaterialia, 2015. **25**: p. 97-108.

109. Fan, Z., et al., *A novel wound dressing based on Ag/graphene polymer hydrogel: effectively kill bacteria and accelerate wound healing*. *Advanced Functional Materials*, 2014. **24**(25): p. 3933-3943.
110. Swaroop, K., S. Francis, and H. Somashekarappa, *Gamma irradiation synthesis of Ag/PVA hydrogels and its antibacterial activity*. *Materials Today: Proceedings*, 2016. **3**(6): p. 1792-1798.
111. Wu, S., et al., *Influence of surface topography on bacterial adhesion: A review (Review)*. *Biointerphases*, 2018. **13**(6): p. 060801.
112. Liu, Y., et al., *Developing polyimide-copper antifouling coatings with capsule structures for sustainable release of copper*. *Materials & Design*, 2017. **130**: p. 285-293.
113. Ji, Y.W., et al., *Comparison of Surface Roughness and Bacterial Adhesion Between Cosmetic Contact Lenses and Conventional Contact Lenses*. *Eye & Contact Lens-Science and Clinical Practice*, 2015. **41**(1): p. 25-33.
114. Giraldez, M.J., et al., *Contact Lens Hydrophobicity and Roughness Effects on Bacterial Adhesion*. *Optometry and Vision Science*, 2010. **87**(6): p. E426-E431.
115. Giraldez, M.J. and E. Yebra-Pimentel, *Hydrogel contact lenses surface roughness and bacterial adhesion, in Ocular Diseases*. 2012, IntechOpen.
116. Preedy, E., et al., *Surface roughness mediated adhesion forces between borosilicate glass and gram-positive bacteria*. *Langmuir*, 2014. **30**(31): p. 9466-9476.
117. Bagherifard, S., et al., *The influence of nanostructured features on bacterial adhesion and bone cell functions on severely shot peened 316L stainless steel*. *Biomaterials*, 2015. **73**: p. 185-197.
118. Lüdecke, C., et al., *Nanorough titanium surfaces reduce adhesion of Escherichia coli and Staphylococcus aureus via nano adhesion points*. *Colloids and Surfaces B: Biointerfaces*, 2016. **145**: p. 617-625.
119. Lee, S.W., et al., *How microbes read the map: effects of implant topography on bacterial adhesion and biofilm formation*. *Biomaterials*, 2020: p. 120595.
120. Perera-Costa, D., et al., *Studying the influence of surface topography on bacterial adhesion using spatially organized microtopographic surface patterns*. *Langmuir*, 2014. **30**(16): p. 4633-4641.
121. Truong, V.K., et al., *The influence of nano-scale surface roughness on bacterial adhesion to ultrafine-grained titanium*. *Biomaterials*, 2010. **31**(13): p. 3674-3683.
122. Graham, M.V. and N.C. Cady, *Nano and microscale topographies for the prevention of bacterial surface fouling*. *Coatings*, 2014. **4**(1): p. 37-59.
123. Singh, A.V., et al., *Quantitative characterization of the influence of the nanoscale morphology of nanostructured surfaces on bacterial adhesion and biofilm formation*. *PloS one*, 2011. **6**(9): p. e25029.
124. Hasan, J., R.J. Crawford, and E.P. Ivanova, *Antibacterial surfaces: the quest for a new generation of biomaterials*. *Trends in biotechnology*, 2013. **31**(5): p. 295-304.
125. Ivanova, E.P., et al., *Natural bactericidal surfaces: mechanical rupture of Pseudomonas aeruginosa cells by cicada wings*. *Small*, 2012. **8**(16): p. 2489-2494.
126. Tripathy, A., et al., *Natural and bioinspired nanostructured bactericidal surfaces*. *Advances in colloid and interface science*, 2017. **248**: p. 85-104.
127. Bandara, C.D., et al., *Bactericidal effects of natural nanopography of dragonfly wing on Escherichia coli*. *ACS applied materials & interfaces*, 2017. **9**(8): p. 6746-6760.
128. Ivanova, E.P., et al., *Bactericidal activity of black silicon*. *Nature communications*, 2013. **4**(1): p. 1-7.
129. Lu, N., et al., *Fabrication of PDMS surfaces with micro patterns and the effect of pattern sizes on bacteria adhesion*. *Food Control*, 2016. **68**: p. 344-351.
130. Hsu, L.C., et al., *Effect of micro-and nanoscale topography on the adhesion of bacterial cells to solid surfaces*. *Applied and environmental microbiology*, 2013. **79**(8): p. 2703-2712.

131. Pacha-Olivenza, M.Á., et al., *Relevance of topographic parameters on the adhesion and proliferation of human gingival fibroblasts and oral bacterial strains*. BioMed research international, 2019. **2019**.
132. Das, J., et al., *An Insight into Surface Topographical Parameters and Bacterial Adhesion: A Case Study of Listeria monocytogenes Scott a Attachment on 304 Stainless Steel*. Journal of food protection, 2020. **83**(3): p. 426-433.
133. Heedy, S., et al., *Synergistic Antimicrobial Activity of a Nanopillar Surface on a Chitosan Hydrogel*. ACS Applied Bio Materials, 2020. **3**(11): p. 8040-8048.
134. Koh, W.-G., et al., *Control of mammalian cell and bacteria adhesion on substrates micropatterned with poly (ethylene glycol) hydrogels*. Biomedical Microdevices, 2003. **5**(1): p. 11-19.
135. da Silva Domingues, J.F., et al., *Macrophage phagocytic activity toward adhering staphylococci on cationic and patterned hydrogel coatings versus common biomaterials*. Acta biomaterialia, 2015. **18**: p. 1-8.
136. Papi, M., et al., *Biomimetic antimicrobial cloak by graphene-oxide agar hydrogel*. Scientific reports, 2016. **6**(1): p. 1-7.
137. Krsko, P., J.B. Kaplan, and M. Libera, *Spatially controlled bacterial adhesion using surface-patterned poly (ethylene glycol) hydrogels*. Acta Biomaterialia, 2009. **5**(2): p. 589-596.
138. Zhang, R., et al., *Crystallization characteristics of polypropylene and low ethylene content polypropylene copolymer with and without nucleating agents*. Journal of applied polymer science, 1994. **51**(1): p. 51-56.
139. Sahin, S. and P. Yayla, *Effects of testing parameters on the mechanical properties of polypropylene random copolymer*. Polymer testing, 2005. **24**(5): p. 613-619.
140. Farrow, G., *Crystallinity, 'crystallite size' and melting point of polypropylene*. Polymer, 1963. **4**: p. 191-197.
141. Xiang, Q., et al., *Effects of melt reprocessing on volatile emissions and structural/rheological changes of unstabilized polypropylene*. Polymer Degradation and Stability, 2002. **77**(1): p. 93-102.
142. Purohit, V. and R. Orzel, *Polypropylene: A literature review of the thermal decomposition products and toxicity*. Journal of the American College of Toxicology, 1988. **7**(2): p. 221-242.
143. Giessibl, F.J., *Principle of nc-AFM*, in *Noncontact atomic force microscopy*. 2002, Springer. p. 11-46.
144. Bramowicz, M., S. Kulesza, and K. Rychlik, *A Comparison between Contact and Tapping AFM Mode in Surface Morphology Studies*. Technical Sciences/University of Warmia and Mazury in Olsztyn, 2012: p. 307-318.
145. Pohan, G., et al., *Effect of Ethylene Oxide Sterilization on Polyvinyl Alcohol Hydrogel Compared with Gamma Radiation*. Tissue Engineering Part A, 2020. **26**(19-20): p. 1077-1090.
146. Fang, J., et al., *Needleless melt-electrospinning of polypropylene nanofibres*. Journal of nanomaterials, 2012. **2012**.
147. Wu, J., et al., *TG/FTIR analysis on co-pyrolysis behavior of PE, PVC and PS*. Waste management, 2014. **34**(3): p. 676-682.
148. Cho, S., et al. *Comparison of thermal performance between glass and silicon interposers*. in *2013 IEEE 63rd Electronic Components and Technology Conference*. 2013. IEEE.
149. Mosse, L., et al., *The effect of process temperature on the formability of polypropylene based fibre-metal laminates*. Composites Part A: Applied science and manufacturing, 2005. **36**(8): p. 1158-1166.
150. Zeng, F., et al., *Effects of heat setting on the morphology and performance of polypropylene separator for lithium ion batteries*. Industrial & Engineering Chemistry Research, 2019. **58**(6): p. 2217-2224.
151. Toosi, S.F., et al., *Microfabrication of polymeric surfaces with extreme wettability using hot embossing*.

- Applied Surface Science, 2016. **378**: p. 426-434.
152. Karsten, E., S.L. Watson, and L.J.R. Foster, *Diversity of microbial species implicated in keratitis: a review*. The open ophthalmology journal, 2012. **6**: p. 110.
 153. Lorentz, H.I., *Modeling in vitro lipid deposition on silicone hydrogel and conventional hydrogel contact lens materials*. 2012.
 154. Maldonado-Codina, C. and P.B. Morgan, *In vitro water wettability of silicone hydrogel contact lenses determined using the sessile drop and captive bubble techniques*. Journal of Biomedical Materials Research Part A: An Official Journal of The Society for Biomaterials, The Japanese Society for Biomaterials, and The Australian Society for Biomaterials and the Korean Society for Biomaterials, 2007. **83**(2): p. 496-502.
 155. HAYES, F.N., *Liquid scintillation counting*. 1958: Citeseer.
 156. Lorentz, H., et al., *The impact of intermittent air exposure on lipid deposition*. Optometry and Vision Science, 2012. **89**(11): p. 1574-1581.
 157. Klotz, S.A., et al., *The contribution of bacterial surface hydrophobicity to the process of adherence of Pseudomonas aeruginosa to hydrophilic contact lenses*. Current eye research, 1989. **8**(2): p. 195-202.
 158. Henriques, M., et al., *Adhesion of Pseudomonas aeruginosa and Staphylococcus epidermidis to silicone-hydrogel contact lenses*. Optometry and vision science, 2005. **82**(6): p. 446-450.
 159. Deitzel, J., et al., *Electrospinning of polymer nanofibers with specific surface chemistry*. Polymer, 2002. **43**(3): p. 1025-1029.
 160. Liu, T., et al., *Photochemical crosslinked electrospun collagen nanofibers: synthesis, characterization and neural stem cell interactions*. Journal of biomedical materials research Part A, 2010. **95**(1): p. 276-282.
 161. Kodjikian, L., et al., *Bacterial adhesion to conventional hydrogel and new silicone-hydrogel contact lens materials*. Graefe's Archive for Clinical and Experimental Ophthalmology, 2008. **246**(2): p. 267-273.
 162. Borazjani, R.N., B. Levy, and D.G. Ahearn, *Relative primary adhesion of Pseudomonas aeruginosa, Serratia marcescens and Staphylococcus aureus to HEMA-type contact lenses and an extended wear silicone hydrogel contact lens of high oxygen permeability*. Contact lens and anterior eye, 2004. **27**(1): p. 3-8.
 163. Wang, M., S. Liu, and F. Li, *Imaging oxygen microenvironment in hydrogel microwell array*. Acta Mechanica Sinica, 2019. **35**(2): p. 321-328.
 164. Lee, G., et al., *Enhanced oxygen permeability in membrane-bottomed concave microwells for the formation of pancreatic islet spheroids*. Acta biomaterialia, 2018. **65**: p. 185-196.